# Dynamics, global and local rheology of vesicles and red blood cells in microcirculation

Abdessamad Nait Ouhra

Communauté
UNIVERSITÉ Grenoble Alpes

# THÈSE

Pour obtenir le grade de

**DOCTEUR DE LA COMMUNAUTE UNIVERSITE GRENOBLE ALPES**

Spécialité : **Physique pour les sciences du vivant**

Arrêté ministériel : 25 mai 2016

Présentée par

**Abdessamad NAIT OUHRA**

Thèse dirigée par **Chaouqi MISBAH**
préparée au sein du **Laboratoire Interdisciplinaire de Physique**

dans **l'École Doctorale de Physique de Grenoble**

# Dynamique, rhéologie globale et local des vésicules et globules rouges en microcirculation

Thèse soutenue publiquement le **9 décembre 2019**,
devant le jury composé de :

**M. Badr ABOU EL MAJD**
Professeur, Université Mohammed V de Rabat, Président
**M. Marc JAEGER**
Professeur, Ecole Centrale de Marseille, Rapporteur
**M. Mhamed MOUQALLID**
Professeur, ENSAM Meknes, Rapporteur
**Mme. Salima RAFAI**
Chargée de recherche CNRS, Grenoble, Examinatrice
**M. Chaouqi MISBAH**
Directeur de recherche CNRS, Grenoble, Directeur de thèse
**M. Alexander FARUTIN**
Chargé de recherche CNRS, Grenoble, Co-encadrant

# Dynamics, global and local rheology of vesicles and red blood cells in microcirculation


Abdessamad Nait Ouhra

Laboratoire Interdisciplinaire de Physique Grenoble

Université Grenoble Alpes

A thesis submitted for the degree of

*Doctor of Physics*

December 9, 2019

# Acknowledgements

I would like to express my sincere gratitude to Chaouqi Misbah for the indispensable guidance, encouragement and support he has provided throughout my research and writing of this thesis. It has been a great pleasure to work with Chaouqi, who always offers me all the freedom for my own interests as an independent researcher and also gives me the necessary advice in the forward direction.

I am particularly grateful to Abdelillah Benyoussef and Hamid Ez-Zahraouy, of the faculty of sciences of Rabat for their supports and guidance on the topic of blood flow, I also thank them for the inspirations and encouragement in many fruitful communications. I would like to thank Alexander Farutin for his patience in answering my questions in boundary integral method and for the careful correction of the thesis manuscript.

I would like to thank the referees of my thesis, Marc Jaeger and Mhamed Mouqallid for having accepted this task. I also thank the other members of the defense committee, Salima Rafai, Badr Abou El Majd and Alexander Farutin. I would also like to express my gratitude to all collaborators.

I would like to thank Hengdi, Suhail and Othmane for the inspiring discussions on vesicle dynamics. Thanks to many members of Liphy, and especially Alexander, Suhail, Hengdi, Mehdi, Zaiyi, Levke, Othmane, Hao, Mattieu, Sylvain ,Philippe Peyla, Philippe Beys, Salima, Mourad, Chantal, Nadine, Sabine, Swapnil, Andrey, Brenna, Dongliang, Vishwas, etc ..., during the duration of my PhD, they provided me with a lot of important suggestions and help. With these lovely people, my life in Grenoble was happy and colorful.

Finally, I would like to thank all my family members who gave me an atmosphere full of love and encouragement.

I acknowledge French-German University Programme "Living Fluids" (Grant No. CFDA-Q1-14), CNRST-Morocco (Grant Ref. k 1/045), Erasmus+ and Campus France, for the financial support.

# Abstract

The rheology and dynamics of red blood cells (RBCs) under confined flows (simple shear and Poiseuille flows), are studied in the Stokes limit. We numerically investigated the rheology of a suspension of RBCs under shear flow in a confined geometry using bounday integral method. We show that the suspension can exhibit both shear-thinning and shear-thickening behavior depending on viscosity contrast between the encapsulated fluid and the suspending one. We provide an appealing interpretation of these behaviors providing a link between microdynamics and global rheology. In the second study, we found that, by increasing the internal viscosity of the suspended entity, the final position can be off-centered, a solution that may either coexist (saddle node bifurcation) or not (pitchfork bifurcation) with the centered solution. These results are somewhat surprising given the general belief that flexible particles tend to migrate away from solid boundaries in shear flow. This novel scenario strongly affects rheological properties of dilute as well as concentrated RBC suspensions. In the last part of this thesis, we focused on the local rheology of RBC suspension. A universal law is discovered. This law links stress to strain rate and local concentration, and its universality means that it is independent of channel width and global concentration.

**Keywords:** Red blood cells, rheology, Stokes, boundary integral method, saddle node bifurcation, pitchfork bifurcation

# Résumé

La rhéologie et la dynamique des globules rouges (GR) sous écoulements confinés (écoulements de cisaillement et de Poiseuille), sont étudiées dans la limite de Stokes. Nous avons étudié numériquement la rhéologie d'une suspension de GR sous un écoulement de cisaillement en utilisant la méthode intégrale de frontière. Nous montrons que la suspension peut avoir un comportement d'un fluide rhéofluidifiant et d'un fluide rhéoépaississant, en fonction du contraste de viscosité entre le fluide encapsulé et le fluide porteur. Nous proposons une interprétation de ces comportements en établissant un lien entre la microdynamique et la rhéologie globale. Dans la deuxième étude, nous avons trouvé qu'en augmentant la viscosité interne de l'entité suspendue, la position finale peut être excentrée, une solution qui peut coexister (bifurcation col-noeud) ou non (bifurcation fourche) avec la solution centrée. Ces résultats sont quelque peu surprenants étant donné la croyance générale que les particules flexibles ont tendance à s'éloigner des parois solides dans un écoulement de cisaillement. Ce nouveau scénario affecte fortement les propriétés rhéologiques des suspensions de GR diluées et concentrées. Dans la dernière partie de cette thèse, nous nous sommes concentrés sur la rhéologie locale de la suspension des globules rouges. Une loi universelle est découverte. Cette loi relie la contrainte au taux de déformation et à la concentration locale, et son universalité signifie qu'elle est indépendante de la largeur du canal et de la concentration globale.

**Mots clés :** Globules rouges, rhéologie, Stokes, méthode intégrale de frontière, bifurcation col-nœud, bifurcation fourche.

# Contents

# Chapter 1

# Introduction

In this chapter, a brief review of human blood and its components is given in Section 1.1. A brief discussion on dynamics of a single red blood cells under flow is given in Section 1.2. An overview of blood's rheology is discussed in Section 1.3 and some pathologies are presented in Section 1.4. Section 1.5 is devoted to the presentation of the main contributions of this thesis.

## 1.1 Brief review on red blood cells

The human blood is a dense suspension of red blood cells (RBCs), which account for around 45% of its total volume. The main function of RBCs among others (transport of nutrients and hormones to the cells all over the body and the regulation of the body temperature) is to carry oxygen from the lungs to the tissues and to carry carbon dioxide from the tissues to the lungs. Besides RBCs, white blood cells (WBCs) and platelet constitute less than 1% of the total blood volume, therefore blood flow is greatly influenced by the dynamics, deformation, orientation and the micro-structure of RBCs within the suspension. A healthy human RBC has a typical shape like biconcave disk with an average diameter $8\mu m$ and a thickness of $2.5\mu m$ (Figure 1.1). The volume of a single RBC is about $90\mu m^3$ and its surface is about $130\mu m^2$ [Tomaiuolo, 2014]. The interior fluid of a RBC is mainly cmposed of haemoglobin solution, which gives to blood its red color. Under physiological conditions, the haemoglobin is Newtonian fluid and has a viscosity 5 to 10 times larger than that of the plasma [Forsyth et al., 2011, Vitkova et al., 2008]. The haemoglobin is enclosed by a membrane which consists of a lipid bilayer scaffolded by a cytoskeleton (see Figure 1.2 for the complex structure of the RBC membrane). The lipid bilayer is about 4nm in thickness.
Owing to the ability of RBCs to flow even in very narrow vessels, the oxygen trans-

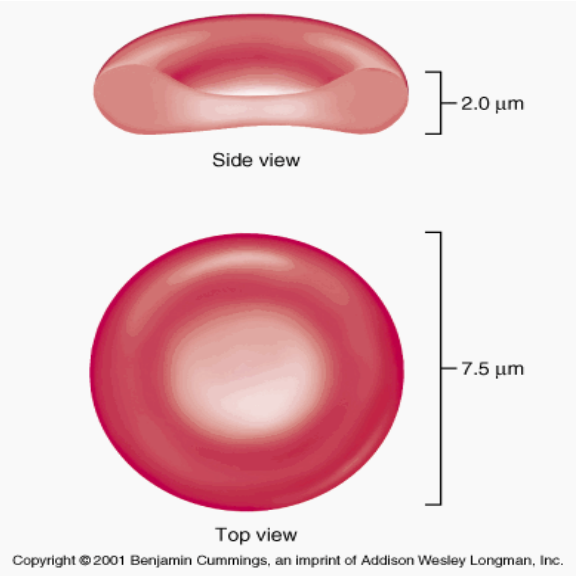


Figure 1.1: Red blood cell.

port to the tissues is enhanced, and due to their deformation, the mixing of the haemoglobin si allowed [Chien, 1975, Schmid-Schonbein, 1975].

## 1.2 Brief review on dynamics of a single RBC under shear flow

Normal human RBCs in quiescent plasma assume a biconcave disk shape. In a shear flow the cell with a large viscosity contrast (the ratio between the inner and the outer viscosities) exhibits an unsteady motion in which the shape of the cell remains essentially unchanged from its resting shape while the cell undergo a flipping motion called tumbling (Figure 1.3), as observed for example in [Goldsmith et al., 1972]. As viscosity contrast decreases the RBC reaches an equilibrium shape and orientation which remains constant as the membrane rotates around the interior fluid (haemoglobin) (Figure 1.3). The last behavior called tank-treading and early observed by Schmid-Schönbein and co-workers [Schmid-Schönbein and Wells, 1969, Fischer et al., 1978]. Long time ago Keller and Skalak have modeled the behavior of nondeforming ellipsoidal particles in shear flow and predicted the two regimes of motion observed for RBCs in shear flow (tumbling and tank-treading) [Keller and Skalak, 1982]. In 2006 C. Misbah found analytically a new type of motion called vacillating breathing: the cell orientation exhibits an oscillation around the flow direction, while the shape executes breathing dynamics [Misbah, 2006]. One year after M. Abkarian et al.

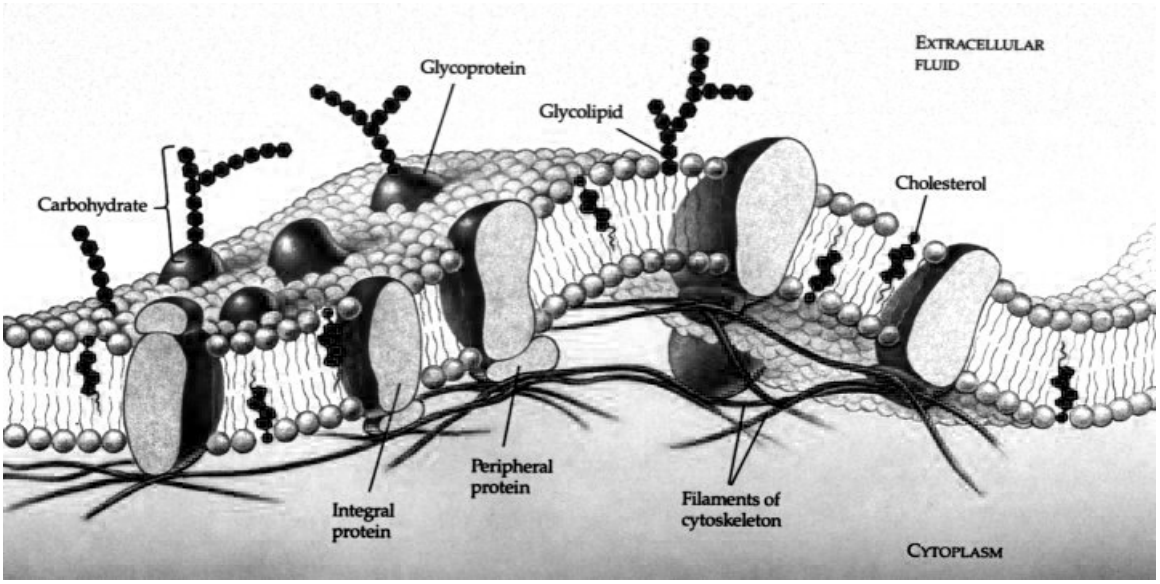


Figure 1.2: A schematic view of the the RBC membrane showing the phospholipid bilayer, the spectrin network (called cytoskeleton) beneath and several membrane and transmembrane proteins.

have reported a similar motion experimentally [Abkarian et al., 2007]. In the last two decades there has been tremendous literature dedicated to dynamics of RBCs, vesicles and capsules (another model of RBCs) either theoretically or experimentally [Viallat and Abkarian, 2014, Kaoui and Harting, 2016, Beaucourt et al., 2004b, Dupire et al., 2012, Vitkova et al., 2012, Farutin and Misbah, 2012, Krüger et al., 2013, Lebedev et al., 2007, Secomb, 2017, Trozzo et al., 2015, Kraus et al., 1996, Zhao and Shaqfeh, 2011, Boedec et al., 2011]. Recent studies of RBCs demonstrate that RBCs show polylobed shapes (Figure 1.4) with increasing the shear rate when the viscosity contrast is large enough [Lanotte et al., 2016, Mauer et al., 2018]. It is claimed that these polylobes are directly linked to the cytoskeleton.

Along this thesis we shall present the impact of some of the aforementioned dynamics of RBCs on the micro-structure of cells on the suspension which in turn affects the rheology of the suspension.

## 1.3 Rheology of blood

The macroscopic rheology of blood has received considerable attention in the past. In the middle of the 19th century, the French physicist and physiologist Jean Léonard Marie Poiseuille reported that in the microvascular network, there exists near the

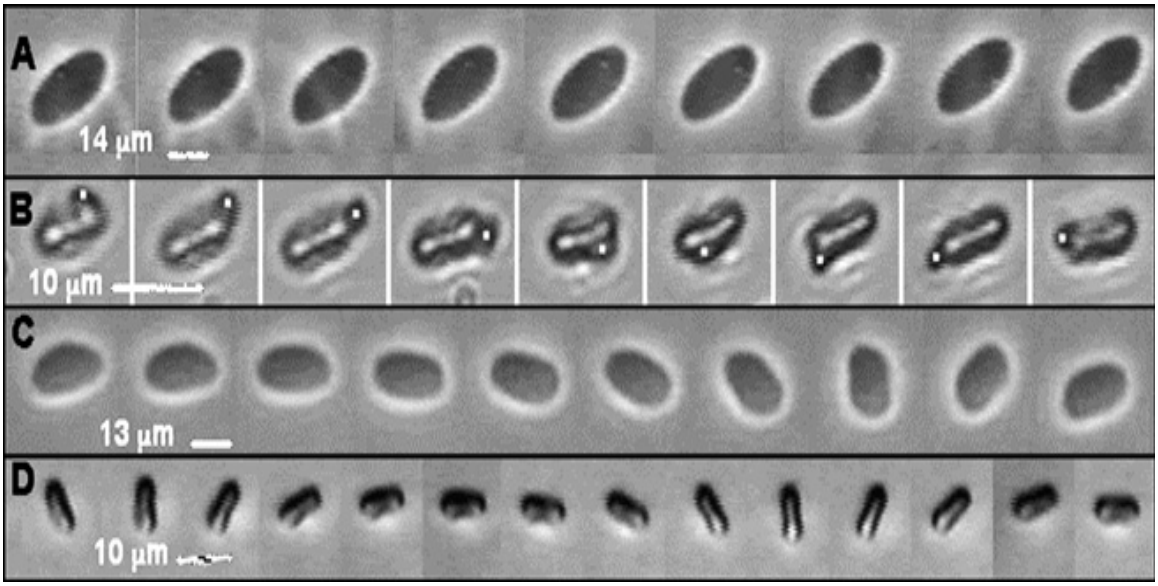


Figure 1.3: Vesicles and red blood cells in shear flow. A: tank-treading vesicle; B: rotation of a bead stuck on the membrane of a tank-treading RBC; C: tumbling vesicle; D: tumbling RBC (from [Abkarian and Viallat, 2008]).

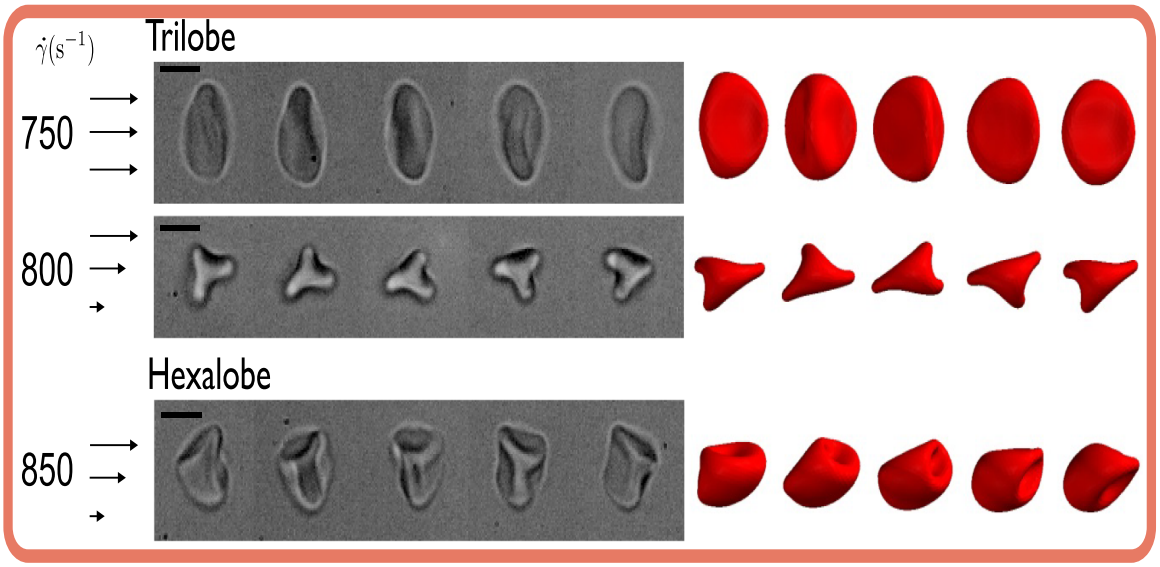


Figure 1.4: Microfluidic observation (left) and numerical simulations (right) of RBC dynamics in shear flow. RBCs show polylobed shapes for large enough viscosity contrast and high values of shear rate (from [Lanotte et al., 2016]).

walls of a vessel in microcirculation, a depletion layer devoid of RBCs and consisting mainly of blood plasma. This cell free layer is due to two antagonist effects: (i) the wall-induced lift that pushes the RBCs towards the channel center, and (ii) particle-particle interactions that induce random lateral motions of RBCs, with a net flux down the concentration gradient, toward the wall. This effect is known as shear-induced diffusion. Poiseuille has derived his famous equation which links the flux of a simple fluid to the diameter of the tube in which the flow takes place, constituting a first attempt to elucidate the flow of blood in capillaries. In 1931, Fåhræus and Lindqvist [Fåhræus and Lindqvist, 1931] found deviation from Poiseuille's law. They found that the blood viscosity in small tube (in vessel diameters ranging from approximately $10\mu m$ to $300\mu m$) decreases as the diameter of the tube decreases (Figure 1.5). This effect is due to the fact that RBCs have a tendency to accumulate towards the blood vessel center, leaving behind a cell-free layer close to the vessel wall. This phenomenon has a major effect in microcirculation leads to higher efficiency of oxygen delivery to tissues.
In short, the rheological properties of blood are mainly determined by the properties of RBCs; including their deformability and dynamics, and their interactions with each other as well as with the surrounding structures.

Besides the heterogeneous distribution of RBCs and its impact on blood rheology, it is commonly believed that blood displays a yield stress attributed to the presence of rouleaux [Merrill et al., 1963, Cokelet et al., 1963, Copley et al., 1973, Picart et al., 1998, Fisher and Rossmann, 2009, Merrill et al., 1969, Thurston, 1972, Morris et al., 1987]. These rouleaux formations are caused by the presence of certain macromolecules, such as fibrinogen, dextran etc (as described for example in [Merrill et al., 1963, Schmid-Schönbein and Wells, 1971, Samsel and Perelson, 1982, Brust et al., 2014]) (see Figure 1.6). Disaggregating is mainly caused by the shear forces present in the bulk flow. Thus, it is necessary to apply a certain stress before blood starts to flow. Experimentally, blood shows a shear-thinning behavior (decreasing of its viscosity with shear rate Figure 1.7) associated with the dissociation of RBC rouleaux upon increasing shear rate [Schmid-schönbein et al., 1969, Dintenfass, 1968, Lipowsky, 2005, Chien, 1970, Chien et al., 1967b, Chien et al., 1967a, Gijsen et al., 1999]. It has been also found that the blood possesses viscoelastic properties that are governed by cell concentration, deformation, aggregation, and plasma viscosity [Chien, 1975]. The viscous properties of blood dominate under most conditions, particularly high shear

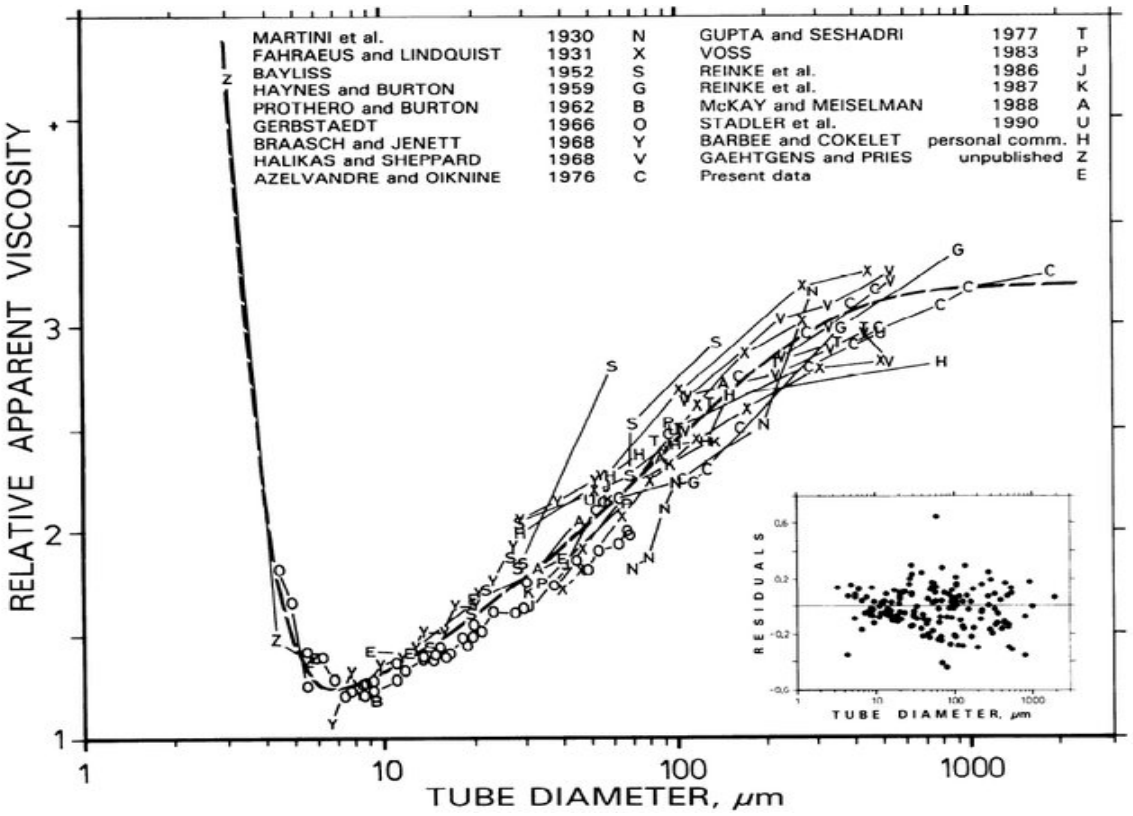


Figure 1.5: Fåhræus-Lindqvist effect (from [Pries et al., 1992]).

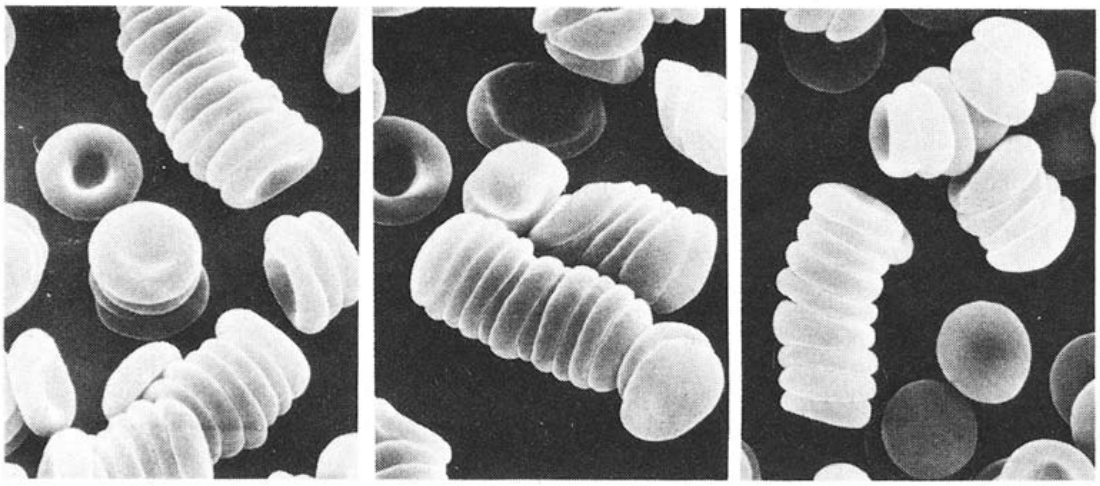

Figure 1.6: Formation and morphology of clusters (rouleaux) of RBCs (from [Maeda and Shiga, 1985]).

deformations. However, under low shear conditions, elasticity becomes increasingly important.

As seen above, blood is: (i) a non-Newtonian fluid (shear-thinning behavior), (ii) affected by confinement (Fåhræus and Lindqvist effect), (iii) a yield stress fluid, and (iv) a viscoelastic fluid. Theoretically, several phenomenological continuum viscoelastic models have been proposed; these models include Casson model, to describe yield stress property [Marcinkowska-Gapińska et al., 2007, Morris et al., 1987, Errill, 1969, Robertson et al., 2009], power-law model, to describe shear thinning behavior [Bodnár et al., 2011, Molla and Paul, 2012], Herschel-Bulkley model, to describe both yield stress and shear thinning properties [Lee et al., 2011, Misra and Maiti, 2012], Quemada model, as another description of shear thinning behavior [Das et al., 1997, Kim et al., 2008], Oldroyd-B model, to describe viscoelastic property [Pontrelli, 2000, Pontrelli, 1998]. Despite these several studies, there is no general approach in tackling the problem of non-Newtonian effects in blood circulation in a systematic way based on a unified vision.

Another feature of interest is the dependence of rheology on hematocrit. Many empirical laws linking the viscosity and the volume fraction of a suspension of rigid particles have been developed which are to be extended to RBCs. The first who has described such system is Einstein in 1906 [Einstein, 1906] for a very dilute suspension

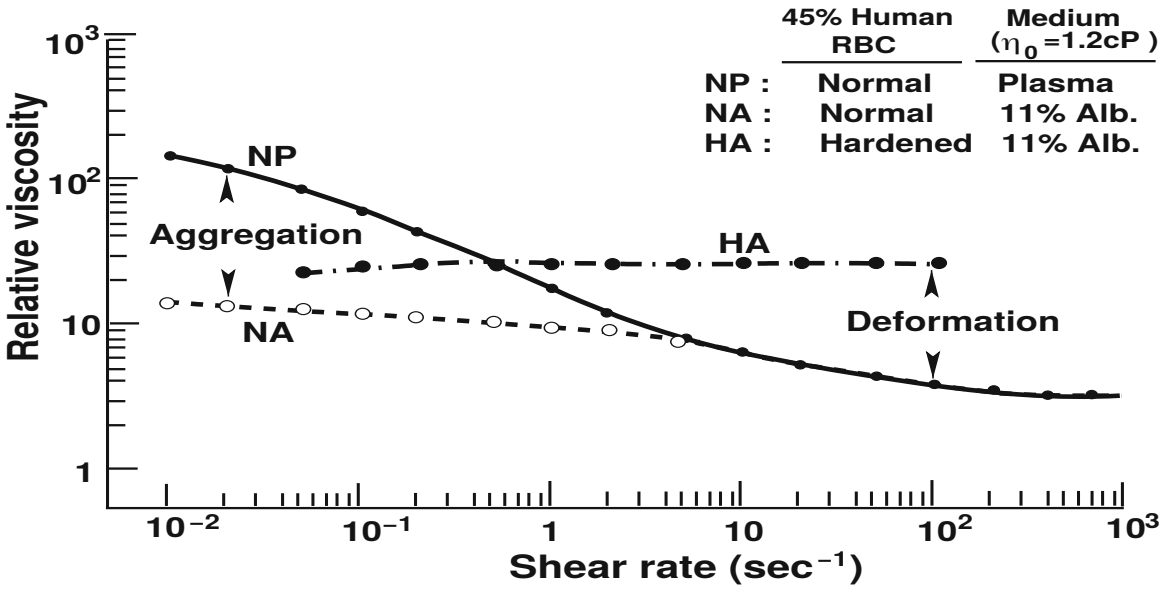


Figure 1.7: Shear thinning of blood: influence of deformation and aggregation of RBCs (from [Chien, 1970]).

of rigid particles. He found that the viscosity of suspension $\eta$ is simply linked to the volume fraction $\phi$ and the viscosity of the suspending fluid $\eta_0$ by the following equation:

$$\eta = \eta_0(1 + [\eta]\phi)$$

where $[\eta] = \lim_{\phi \to 0} \frac{\eta - \eta_0}{\eta_0 \phi} = \frac{5}{2}$ for rigid spheres. The last formula has been extended to small drops [Taylor, 1932] and to vesicles [Danker and Misbah, 2007a].
The Einstein's formula is valid for a dilute suspension. For high concentrations the interactions between the particles play a role and Batchelor has proposed the following [Batchelor, 1970]:

$$\eta = \eta_0(1 + [\eta]\phi + B\phi^2 + \mathcal{O}(\phi^2))$$

where $B = 5$ for rigid spheres. For high concentrations, it was necessary to introduce the parameter $\phi_m$, which is the maximum volume fraction of particles that represents the state of jammed suspension for which the viscosity diverges. Krieger and Dougherty [Krieger and Dougherty, 1959] have proposed a phenomenological law valid for dilute and dense suspension which takes into account $\phi_m$:

$$\eta = \eta_0(1 - \frac{\phi}{\phi_m})^{-[\eta]\phi_m}$$

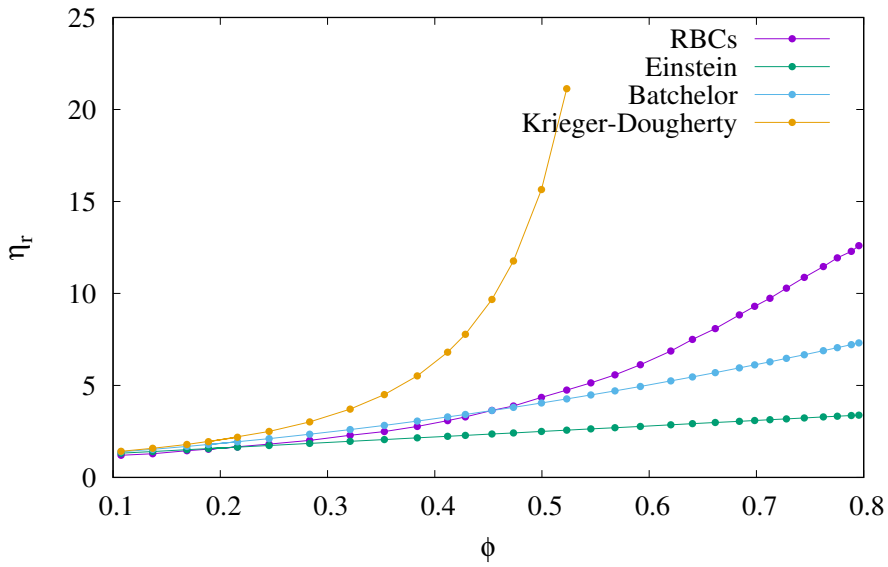


Figure 1.8: The relative viscosity $\eta_r = \eta/\eta_0$ of a suspension of RBCs as a function of concentration $\phi$ according to Einstein, Batchelor and Krieger-Doughtry models and according experimental data (from [Baskurt and Meiselman, 2003], $[\eta] = 3, \phi_m = 0.67$). Here B=6.2.

Figure 1.8 shows the effect of concentration on a suspension of RBCs, using the above macrospic models, comparing with experimental results for RBCs from [Baskurt and Meiselman, 2003]. It is clear that in dilute suspension, the above models are in a good agreement with the experiment. However a general agreement is far from being achieved.

A basic understanding of the behavior of confined suspensions requires, on the one hand, the identification of the key parameters that play a relevant role, and on the other hand linking the microscale (e.g. the spatiotemporal organization) to the macroscale. The present thesis is directed along this objective. We will see that the viscosity contrast $\lambda$ plays an essential role in the spatial organization, which in turn affects rheology.

The rheology of confined suspensions has been addressed quite sparsely to date. Regarding suspensions of rigid spheres, Peyla et al. [Peyla and Verdier, 2011, Davit and Peyla, 2008, Sangani et al., 2011] have shown that for a certain range of ratio between the gap size and the particle size, the interactions between particles leads to a decrease of the total dissipation. 2D and 3D numerical simulations and experiments of confined RBCs [Thiébaud et al., 2014, Shen et al., 2018] have been performed using vesicles and capsules as a model. It has been shown that confinement leads to a subtle ordering with a strong impact on rheology. It is found that the effective viscosity of a

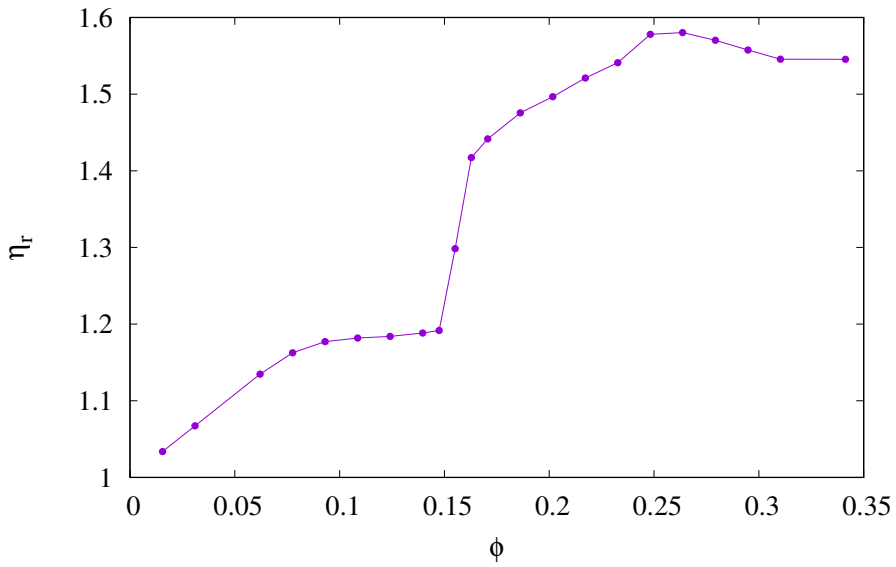


Figure 1.9: The relative viscosity as a function of vesicle concentration (from [Thiébaud et al., 2014]).

suspension of vesicles increases with the concentration in a non-monotonic way (see Figure 1.9). Similar ordering [Fornari et al., 2016] has been reported on confined suspensions of rigid paricles in the presence of inertia.

In summary, blood flow displays a complex character results from RBCs deformation and their heterogeneous distribution, and its theoretical description remains a challenging task. All the existing macroscopic phenomenological models are incapable of fully describing blood flow and can not be considered as reliable. Based on that, a new generation of models is requested. To come up with a first model of this new generation of models we must resort to a local microscopic analysis. To do so, we will study the local rheology (i.e. $\sigma(\dot{\gamma}(\phi_l))$, $\sigma$: stress, $\dot{\gamma}$: shear rate and $\phi_l$: local concentration), taking into account the local concentration of cells, which is highly affected by the interactions of RBCs with each other. We shall show that for a given local concentration, the local relationship between stress and strain rate is deterministic and linear whatever the value of the gap and global concentration is.

## 1.4 Pathologies and rheology

The viscosity of blood is considered as one of the indicators in the understanding and diagnosis of diseases. For example, the hardening of RBCs is known [Chien et al., 1967a, Brooks et al., 1970, Schmid-Schönbein and Wells, 1971, Bookchin and Lew,

1996, Embury et al., 1994, Pauling et al., 1949] to increase the viscosity of suspension, which is the case for many hematologic disorders and diseases, such as malaria, sickle-cell anemia, spherocytosis etc. Moreover, the rigidity of RBCs is related to increase of the cytoplasm viscosity (i.e. increase of the viscosity contrast between the fluid viscosities of the inner and outer fluids) [Chien et al., 1970, Imai et al., 2010, Bow et al., 2011, Suresh, 2006, Barabino et al., 2010, Li et al., 2013]. The lack of flexibility causes difficulty for RBCs passing through blood vessels and this affects their physiological function regarding oxygen transport [Wang and Popel, 1993]. It is also shown that the hardened RBCs may exhibit a shear thickening behavior [Lanotte et al., 2016] constituting thus an opposite rheological behavior of healthy blood which exhibits a shear thinning behavior.

Beside the deformabiliy of the RBCs, the RBC hyper-aggregation, an abnormal increase in RBC aggregation, constitutes another pathological state associated with several circulatory diseases such as deep venous thrombosis, atherosclerosis, AIDS, myeloma, and diabetes mellitus, which may afflict many different sites of the human arterial tree [Franceschini et al., 2010, Robertson et al., 2008, Dintenfass, 1980]. This hyper-aggregation is due to an increased level of fibrinogen in the blood which enhances the aggregation of RBC with more robust clusters, as encountered also in other pathological cases such as cardiac diseases [Robertson et al., 2008] or sepsis [Baskurt et al., 1997].

## 1.5 Contribution of the present thesis

This work contributes to the understanding of dynamics and rheology of blood. The 2D vesicle model (a closed membrane of phospholipid that mimics the cytoplasmic membrane of RBCs) will be adopted to model a RBC. However, some 3D simulations have been performed in this thesis where we have confirmed some novel scenarios adopted by 2D vesicle model. In this thesis we are interested in dilute as well as dense suspensions, in their dynamics, their global and local rheology. The main contributions are discussed in the following subsections.

### 1.5.1 Shear-rate dependent viscosity of a confined suspension of vesicles under shear flow

In this study we analyse the rheology of a suspension of vesicles in a confined geometry: the suspension, bound by two planar rigid walls on each side, is subject to a

shear flow. Flow properties are then analyzed as a function of shear rate $\dot{\gamma}$, the concentration of the suspension $\phi$ and the viscosity contrast $\lambda = \eta_{in}/\eta_{out}$, where $\eta_{in}$ and $\eta_{out}$ are the fluid viscosities of the inner and outer fluids, respectively. We find that the apparent (or effective viscosity) of the suspension exhibits both shear-thinning (decreasing viscosity with shear rate) or shear-thickening (increasing viscosity with shear rate) in the same concentration range. The shear- thinning or thickening behaviors appear as subtle phenomena, depending on viscosity contrast $\lambda$. We provide physical arguments on the origins of these behaviors. This work has given rise to an article which has been published in Physical Review E [A. Nait Ouhra et al., Phys. Rev. E 97, 012404 (2018).]. This study is presented in Chapter 3.

### 1.5.2 Lateral vesicle migration in a confined shear flow: Viscosity contrast leads to off-center solutions

In this study, the lateral migration of a suspended vesicle in a bounded shear flow is investigated numerically using a boundary integral method. We explore, among other parameters, the effect of the viscosity contrast $\lambda$. We found that a vesicle can either migrate to the centerline or towards the wall depending on $\lambda$. More precisely, below a critical viscosity contrast $\lambda_c$, the terminal position is at the centerline, whereas above $\lambda_c$, the vesicle can be either centered or off-centered depending on initial conditions. It is found that the equilibrium lateral position of the vesicle exhibits a saddle-node bifurcation as a function of the bifurcation parameter $\lambda$. When the shear stress increases the saddle-node bifurcation evolves towards a pitchfork bifurcation. A systematic analysis is first performed in 2D (due to numerical efficiency). The overall picture is confirmed in 3D. This study can be exploited in the problem of cell sorting and can help understand the intricate nature of the dynamics and rheology of confined suspensions. This work is presented in Chapter 4. This work has given rise to an article which has been published in Physical Review Fluids [A.Nait-Ouhra et al., Phys. Rev. Fluids 3, 123601 (2018).].

### 1.5.3 The effect of initial conditions on the rheology of a vesicle suspension under a bounded shear flow

This study is a follow up of the previous one, where we have found that the single vesicle may migrate to the centerline or towards the wall depending on the viscosity contrast $\lambda$. The current study shows that this bifurcation of the equilibrium lateral position of the vesicle has a strong rheological signature, which leads often to a

surprising acute decrease in the effective viscosity of the suspension above a critical $\lambda$. In the dilute regime, it is found that the effective viscosity corresponding to the off-centered solution may have a lower value than that of the centered solution. Moreover the effective viscosity shows a discontinuity as a function of $\lambda$. This discontinuity is traced back to the existence of a saddle node bifurcation of the lateral position. When the flow strength is increased the viscosity behavior becomes continuous, owing to the evolution of the transition of the off-centered solution from a saddle-node to a pitchfork bifurcation. We analyze then rheology as a function of the suspension concentration for different values of $\lambda$. For large enough $\lambda$ the viscosity may be lower or larger than that corresponding to small $\lambda$, depending on initial configuration. There is a critical concentration beyond which the initial configuration is irrelevant, but still the behavior of the suspension viscosity with concentration for low and large $\lambda$ are quite different both qualitatively and quantitatively. This is traced back to special spatial organization of the confined suspensions, which depends on $\lambda$. This work is presented in chapter 5. This study has given rise to an article which has been published in Physical Review Fluids [A. Nait-Ouhra et al., Phys. Rev. Fluids 4, 103602 (2019)].

### 1.5.4 Local rheology of a dense suspension of vesicles under a confined pressure-driven flow

The rheological properties of blood strongly depend on the flow geometry and on the mechanical properties of the RBCs. Moreover, the spatial variations of the concentration of RBCs within the vessel (Fåhræus-Lindqvist effect [Fåhræus and Lindqvist, 1931]) are expected to lead to a spatial variation of the local effective viscosity. Thus the notion of a global effective viscosity does not define a full rheological picture of the suspension. In this study we provide a new picture which goes beyond the state of the art of rheology of suspensions. The objective is to address the question whether or not there exits a universal law linking the local stress to the local shear rate and the local concentration. We address this question by simulations of a suspension of vesicles in confined flow, extracting the averaged shear rate and concentration profiles. This work is split up into two parts: i) in the first part we investigate how the flow strength alter the rheological law of a suspension of vesicles. A study done by L. Bocquet and co-workers [Goyon et al., 2008] reveals non-locality and cooperativity effects of emulsions. They found that the same sample of a confined emulsion may exhibit different rheological laws depending only on the flow strength. Our study for vesicles, so far, does not show any non-local effect. ii) The second part consists

in linking the local viscosity of a suspension of vesicles to the local concentration, as well as linking the local relationship between local stress and local shear rate to the local concentration. A universal law is discovered: the local fluidity can be well described as a function of the local concentration only, independently of the channel's width within which the flow suspension takes place or the global concentration of the suspension. This work is presented in Chapter 6. A paper is under preparation.

# Chapter 2

# Model and simulation method

In the present chapter, the system of vesicle as a simple model of red blood cell and the method used to solve the hydrodynamic equations are presented. We first present in Section 2.1 the vesicle and its mathematical model. We describe in Section 2.2 the hydrodynamic equations. In Section 2.3 we present the method used in this thesis, namely the Boundary Integral Method (BIM). The numerical procedure is summarized in Section 2.4. Finally, the derivation of the rheological quantities is shown in Section 2.5.

## 2.1 Red blood cell membrane model

Here we describe the model of vesicle used to mimic the dynamics and rheology of RBCs. Vesicles are closed membranes of phospholipids which are closed fluid membranes, suspended in an aqueous medium. They are made of bilayers of phospholipids, each having a hydrophilic head and two hydrophobic tails [Lipowsky and Sackmann, 1995].

Numerical studies explored in this thesis have focused on a two dimensional case, which offers low enough numerical cost for a more systematic investigation. However some three-dimensional simulations have been also performed.

### 2.1.1 Two-dimensional model

In a two dimensional space, a vesicle has its membrane shape illustrated by a closed curve (interface). The Helfrich energy [Zhong-Can and Helfrich, 1989] is defined on the interface as a the sum of bending and inextensibility contributions

$$E = \frac{\kappa}{2}\int_{\text{mem}} c^2 ds + \int_{\text{mem}} \xi ds \tag{2.1}$$

where the integrals are performed over the membrane interface "mem". This energy includes a tension-like term $\xi$ in order to fulfill the local arclength conservation constraint. Strictly speaking $\xi$ is a Lagrange multiplier. $c$ is the membrane curvature, $s$ is the curvilinear coordinate along the membrane, and $\kappa$ is the membrane bending rigidity (typical value for vesicles is of about a fraction of $eV$). The enclosed area $A$ is conserved automatically thanks to the fluid incompressibility (it is enforced by the pressure term in the flow equations 2.11 written below in section 2.2.2). The force (per unit area) associated with this energy (E) is obtained from the functional derivative of the Helfrich energy (Eq 2.1):

$$\mathbf{f}_{\text{mem}\to\text{flu}} = \kappa \left( \frac{d^2 c}{ds^2} + \frac{1}{2} c^3 \right) \mathbf{n} - \xi c \mathbf{n} + \frac{d\xi}{ds} \mathbf{t} \tag{2.2}$$

Here $\mathbf{n}$ and $\mathbf{t}$ are the unit normal and tangent vectors. The force (2.2) is derived in 2D in [Kaoui et al., 2008]. Physically this force means that the membrane vesicle acts on the fluid (in and outside of the interface) via bending force (first term) and tension force (two last terms). The still unknown Lagrange multiplier $\xi$ is obtained by imposing a divergence-free velocity along the membrane, expressing the membrane incompressibility. The numerical method of imposing membrane incompressibility follows closely that presented in [Ghigliotti et al., 2010].

We define the reduced area as the ratio between the actual fluid area enclosed by the vesicle contour $A = \pi R_0^2$ and the area of a circle which has the same perimeter (denoted as $L$) as the vesicle.

$$\tau = \frac{4\pi A}{L^2} \tag{2.3}$$

For a circle $\tau = 1$, otherwise $\tau < 1$. The effective vesicle radius ($R_0 = \sqrt{A/\pi}$) is chosen to be the characteristic length. For a RBC, the effective radius is $R_0 \simeq 3\mu m$.

### 2.1.2 Three-dimensional model

As stated above, some 3D numerical simulation have been carried out along this thesis. We consider for this case a pure 3D vesicle, which does not exhibit any shear elasticity. We model the vesicle's bending rigidity according to the Helfrich model with a bending modulus $\kappa$ [Zhong-Can and Helfrich, 1989,Trozzo et al., 2015,Guckenberger and Gekle, 2017]. The force (per unit area) $\mathbf{f}_{\text{mem}\to\text{flu}}$ can be expressed as:

$$\mathbf{f}_{\text{mem}\to\text{flu}} = 2\kappa \left[ 2H \left( H^2 - K \right) + \Delta^s H \right] \mathbf{n} \tag{2.4}$$

Here, $H = (c_1 + c_2)/2$ is the mean curvature, where $c_1$ and $c_2$ are the principle curvatures, $K = c_1 c_2$ is the Gaussian curvature and $\Delta^s$ the Laplace-Beltrami operator.

Numerically, we compute the surface force via the parabolic fitting method from [Farutin et al., 2014] (a detailed analysis can be found in [Guckenberger et al., 2016], see Method E therein).

An artificial volume drift of the vesicle is countered by employing the no-flux condition and the rescaling method as in [Guckenberger and Gekle, 2018], i.e. the volume $V$ is perfectly conserved. The global surface area is kept approximately constant via an effective surface force with a surface modulus of $\kappa_A = 2000\kappa/R_0^2$. This results in typical surface deviations of $\lesssim 0.3\%$ which is consistent with [Biben et al., 2011]. The mesh is stabilized by employing the procedure from [Guckenberger and Gekle, 2018, eq. (2.74)] (which is very similar to [Farutin et al., 2014, eq. (59)]) with a strength of $\zeta = 0.03$ ($\zeta$ is a parameter that controls the stiffness of the scheme used the prevent the large distortions of the mesh).

The reduced volume is slightly different from its counterpart for 2D case. It is defined as the ratio of the volume of the vesicle $V$ to the volume of a sphere having the same surface $A'$ as the vesicle:

$$\tau^{3D} = 6\sqrt{\pi}V/A'^{3/2} \tag{2.5}$$

For a spherical vesicle $\tau^{3D} = 1$, otherwise $\tau < 1$ (deflated vesicle). The effective radius is defined as $R_0 = (3V/(4\pi))^{1/3}$.

## 2.2 Hydrodynamic equations

### 2.2.1 *Navier-Stokes* equations

The internal and external fluids (see Figure 2.1), are considered to be incompressible Newtonian fluids with viscosity $\eta$ and density $\rho$. They are governed by the known *Navier-Stokes* equations:

$$\begin{aligned} \rho\frac{D\mathbf{v}}{Dt} &= -\nabla p + \eta\nabla^2\mathbf{v} + \int_{mem} ds(\mathbf{r}_0)\mathbf{f}_{\text{mem}\to\text{flu}}(\mathbf{r}_0)\delta(\mathbf{r}-\mathbf{r}_0) \\ \nabla.\mathbf{v} &= 0, \end{aligned} \tag{2.6}$$

where $\mathbf{v}$ is the velocity field and $p$ is the pressure. $\mathbf{f}_{\text{mem}\to\text{flu}}$ is the force (per unit area) applied by the membrane on the fluids, which is given by equation 2.2 for 2D case. $\delta(\mathbf{r}-\mathbf{r}_0)$ is a Dirac Delta function that identifies the position $\mathbf{r}_0$ of the membrane. Here $D/Dt := \partial/\partial t + \mathbf{v}.\nabla$ is the material derivative.

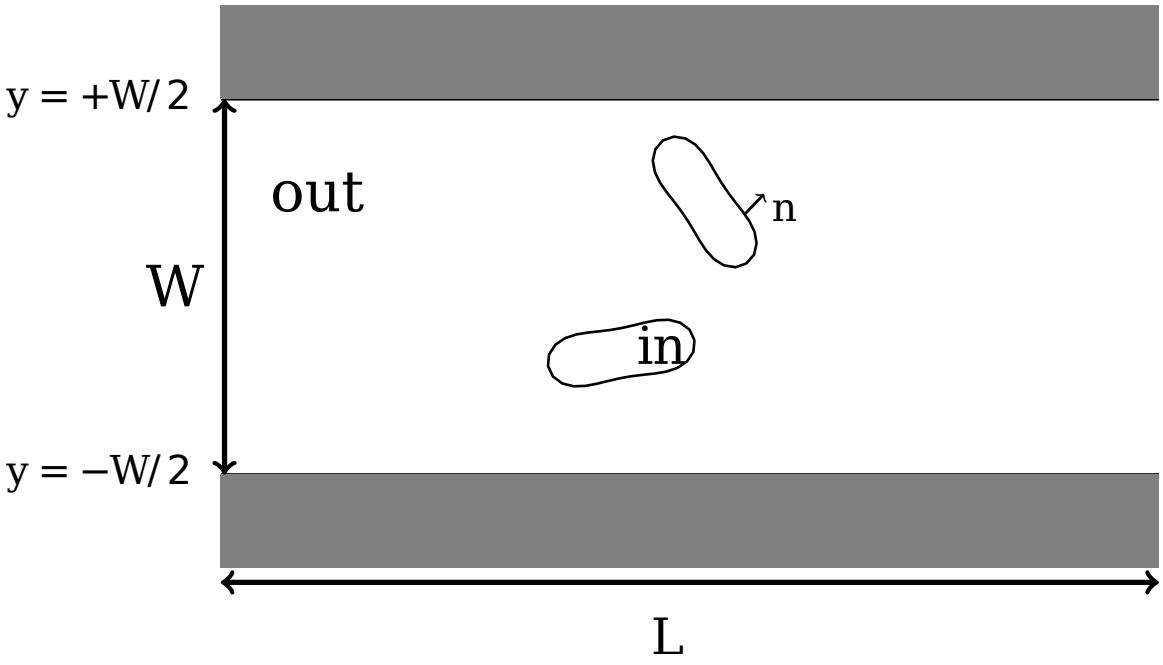


Figure 2.1: Schematic view of the simulated system.

It is useful to write equations 2.6 in a nondimensional form. To do so, the physical quantities are divided by some reference values of relevance in the problem. We introduce nondimensional quantities as follows:

- $\mathbf{v}^* = \mathbf{v}/U$;
- $\mathbf{r}^* = \mathbf{r}/R_0$;
- $t^* = tU/R_0$;
- $p^* = pR_0/\eta U$;
- $\mathbf{f}^*_{\text{mem}\to\text{flu}} = R_0^3/\kappa \mathbf{f}_{\text{mem}\to\text{flu}}$;
- $\delta(\mathbf{r} - \mathbf{r}_0) = \delta(\mathbf{r}^* - \mathbf{r}^*_0)/R_0^2$;

Where $U$ is a typical velocity of the flow, $R_0$ is a typical length (the radius of vesicle).
If we substitute these quantities into the *Navier-Stokes* equation 2.6, we obtain the dimensionless form:

$$\begin{aligned} Re\frac{D\mathbf{v}^*}{Dt^*} &= -\nabla^* p^* + \frac{\eta}{\eta_{out}}\nabla^{*2}\mathbf{v}^* + \frac{1}{C_\kappa}\int_{mem} ds^*(\mathbf{r}^*_\mathbf{0})\mathbf{f}^*_{\text{mem}\to\text{liq}}(\mathbf{r}^*_0)\delta^*(\mathbf{r}^* - \mathbf{r}^*_0) \\ \nabla^*.\mathbf{v}^* &= 0 \end{aligned} \tag{2.7}$$

We come out with the following adimensional numbers:

- *The Reynolds number*:
$$Re = \frac{\rho U R_0}{\eta_{out}} \tag{2.8}$$
it represents the relative importance of inertial and viscous effects.

- *The capillary number*:
$$C_\kappa = \frac{\eta_{out}\dot{\gamma} R_0^3}{\kappa} \equiv \dot{\gamma} t_c \tag{2.9}$$
it measures the flow strength over the bending energy of the membrane. In other words, $C_\kappa$ controls how the shapes of vesicles deform in response to an applied external flow. Here $t_c$ is the typical time needed for the vesicle to recover its equilibrium shape after cessation of flow.

- *The viscosity ratio:*
$$\lambda = \frac{\eta_{in}}{\eta_{out}} \tag{2.10}$$
where $\eta_{in}$ and $\eta_{out}$ are the fluid viscosities of the inner (hemoglobin solution for RBC) and outer fluids, respectively.

### 2.2.2 *Stokes* equations

Vesicles and RBCs are small enough and their speeds (say in vivo for RBCs) are small, so that the corresponding Reynolds number is small (typically in the range $10^{-4} - 10^{-2}$). We can safely consider the limit of a vanishing Reynolds number (the Stokes limit), where the flow is governed by viscous forces (inertia is neglected).
With the assumption of vanishing Reynolds number, the hydrodynamic equations (2.6) for a suspension of vesicles become:

$$\begin{aligned} -\nabla p + \eta \nabla^2 \mathbf{v} + \int_{mem} ds(\mathbf{r_0}) \mathbf{f}_{\text{mem}\to\text{flu}}(\mathbf{r_0}) \delta(\mathbf{r} - \mathbf{r}_0) &= \mathbf{0} \\ \nabla . \mathbf{v} &= 0 \end{aligned} \tag{2.11}$$

### 2.2.3 Boundary conditions

The equations above are accompanied with the following boundary conditions:

$$\mathbf{v} = \mathbf{V}^0 \quad at \quad infinity \quad (unperturbed \quad flow) \tag{2.12}$$

$$\mathbf{v}_{int} = \mathbf{v}_{out} = \mathbf{v} \quad on \quad \partial\Omega \equiv \text{"}mem\text{"} \quad (membrane) \tag{2.13}$$

for last equation (2.13) the continuity of the normal component is a consequence of the mass conservation, while the tangential velocity continuity follows from the assumption of no-slip condition.

## 2.3 Boundary integral equation

### 2.3.1 Boundary integral equation in an unbounded geometry

The numerical method adopted along this thesis is for the computation of two-dimensional Stokes flows in the presence of an interface's force (equations 2.11). Here we give the main steps to derive the boundary integral equation for Stokes equations which describe the motion of a membrane. For more details the reader may refer to [Pozrikidis, 1992]. The first starting point for deriving this integral equation is the *Lorentz* reciprocal identity:

$$\nabla.(\mathbf{v}'.\boldsymbol{\sigma} - \mathbf{v}.\boldsymbol{\sigma}') = 0 \tag{2.14}$$

where $\mathbf{v}$ and $\mathbf{v}'$ are two solutions of Stokes equations occuring in a domain $\Omega$ and $\boldsymbol{\sigma}$ and $\boldsymbol{\sigma}'$ are their associated stress tensors respectively.
We identify $\mathbf{v}'$ the flow due to a point force with strength $\mathbf{f}$ located at point $\mathbf{r_0}$ and $\boldsymbol{\sigma}'$ its associated stress tensor. The solution of this flow $(\mathbf{v}', \boldsymbol{\sigma}')$ is given by:

$$\mathbf{v}'(\mathbf{r}) = \frac{1}{4\eta\pi}\mathbf{G}(\mathbf{r}, \mathbf{r_0})\mathbf{f} \tag{2.15}$$

$$\boldsymbol{\sigma}' = \frac{1}{4\pi}\mathbf{T}(\mathbf{r}, \mathbf{r_0})\mathbf{f} \tag{2.16}$$

where $\mathbf{G}$ and $\mathbf{T}$ are the Green's function (also called *fundamental solution* or *propagator*) and its associated stress tensor for unbounded 2D flow, their corresponding scalar formula are given by:

$$\mathbf{G}_{ij} = -\delta_{ij}\ln|\mathbf{r} - \mathbf{r_0}| + \frac{(\mathbf{r} - \mathbf{r_0})_i(\mathbf{r} - \mathbf{r_0})_j}{(\mathbf{r} - \mathbf{r_0})^2} \tag{2.17}$$

$$\mathbf{T}_{ijk} = -4\frac{(\mathbf{r} - \mathbf{r_0})_i(\mathbf{r} - \mathbf{r_0})_j(\mathbf{r} - \mathbf{r_0})_k}{(\mathbf{r} - \mathbf{r_0})^2} \tag{2.18}$$

Later we shall show specific Green's functions for a bounded geometry with no-slip conditions.
Substituting 2.15 and 2.16 in 2.14, integrating over the domain $\Omega$ and applying the divergence theorem we obtain:

$$\begin{aligned}\frac{-1}{4\pi\eta}\int_{mem}\mathbf{f}(\mathbf{r})\mathbf{G}(\mathbf{r}, \mathbf{r_0})ds + \\ \frac{1}{4\pi}\int_{mem}\mathbf{v}(\mathbf{r})\mathbf{T}(\mathbf{r}, \mathbf{r_0})\mathbf{n}ds = \begin{cases}\mathbf{v}(\mathbf{r_0}) & \text{if} \quad \mathbf{r_0} \in \Omega \\ \mathbf{0} & \text{if} \quad \mathbf{r_0} \notin \Omega\end{cases}\end{aligned} \tag{2.19}$$

where *'mem'* designating the membrane interface. The first term on the LHS of 2.19 is called the *single-layer potential*, whereas the second term is called the *double-layer*

*potential*. It is demonstrated that the *doubl-layer potential* is not continuous as $\mathbf{r_0}$ approaches the membrane interface [Barthès-Biesel, 2012]. For the latter case ($r_0$ approaching membrane interface) the second integral of 2.19 becomes:

$$\lim_{\mathbf{r_0}\to mem}\int_{mem}\mathbf{v}(\mathbf{r})\mathbf{T}(\mathbf{r},\mathbf{r_0})\mathbf{n}ds = \pm 2\pi\mathbf{v}(\mathbf{r_0}) + \int_{mem}^{\mathcal{PV}}\mathbf{v}(\mathbf{r})\mathbf{T}(\mathbf{r},\mathbf{r_0})\mathbf{n}ds \tag{2.20}$$

where the plus (minus) sign corresponds to the case where $\mathbf{r_0}$ approaches from inside (outside) to the membrane interface. $\mathcal{PV}$ indicates the principle value of the *double-layer potential*. The limit in 2.20 does exist only if the normal vector $\mathbf{n}$ to the membrane interface is continuous (Lyapunov curve). Combining 2.20 and 2.19 we find that

$$\alpha\mathbf{v}(\mathbf{r_0}) = \frac{-1}{4\pi\eta}\int_{mem}\mathbf{f}(\mathbf{r})\mathbf{G}(\mathbf{r},\mathbf{r_0})ds + \frac{1}{4\pi}\int_{mem}^{\mathcal{PV}}\mathbf{v}(\mathbf{r})\mathbf{T}(\mathbf{r},\mathbf{r_0})\mathbf{n}ds \tag{2.21}$$

with

$$\alpha = \begin{cases} \mathbf{0} & \text{if} \quad \mathbf{r_0}\notin\Omega \\ 1 & \text{if} \quad \mathbf{r_0}\in\Omega \\ \frac{1}{2} & \text{if} \quad \mathbf{r_0}\in\partial\Omega \quad (\mathbf{r_0} \quad \text{approaching from outside}) \end{cases} \tag{2.22}$$

Lets consider the subscript $'out'$ for outside the vesicle and $'in'$ for inside. We define the viscosity contrast as $\lambda = \frac{\eta_{in}}{\eta_{out}}$. From the equation 2.21 we get for the external flow:

$$\mathbf{v_{out}}(\mathbf{r_0}) = \frac{-1}{4\pi\eta_{out}}\int_{mem}\mathbf{f_{out}}(\mathbf{r})\mathbf{G}(\mathbf{r},\mathbf{r_0})ds + \frac{1}{4\pi}\int_{mem}\mathbf{v}(\mathbf{r})\mathbf{T}(\mathbf{r},\mathbf{r_0})\mathbf{n}ds \tag{2.23}$$

We apply the the reciprocal identity 2.14 (integrating over the membrane *'mem'*, applying the divergence theorem) for the internal flow $\mathbf{v_{in}}(\mathbf{r_0})$:

$$\int_{mem}\mathbf{f_{in}}(\mathbf{r})\mathbf{G}(\mathbf{r},\mathbf{r_0})ds - \eta_{in}\int_{mem}\mathbf{v}(\mathbf{r})\mathbf{T}(\mathbf{r},\mathbf{r_0})\mathbf{n}ds = 0 \tag{2.24}$$

Combining the two equations 2.24 and 2.23 we find

$$\mathbf{v_{out}}(\mathbf{r_0}) = \frac{-1}{4\pi\eta_{out}}\int_{mem}\Delta\mathbf{f}(\mathbf{r})\mathbf{G}(\mathbf{r},\mathbf{r_0})ds + \frac{1-\lambda}{4\pi}\int_{mem}\mathbf{v}(\mathbf{r})\mathbf{T}(\mathbf{r},\mathbf{r_0})\mathbf{n}ds \tag{2.25}$$

where $\Delta\mathbf{f} = \mathbf{f}_{out} - \mathbf{f}_{in}$ is the discontinuity in the interfacial stress. Next, we seek to derive a boundary integral representation for the internal flow. Following the same procedure (2.24 and 2.23) we get for the internal flow:

$$\mathbf{v_{in}}(\mathbf{r_0}) = \frac{-1}{4\pi\eta_{in}\lambda}\int_{mem}\Delta\mathbf{f}(\mathbf{r})\mathbf{G}(\mathbf{r},\mathbf{r_0})ds + \frac{1-\lambda}{4\pi\lambda}\int_{mem}\mathbf{v}(\mathbf{r})\mathbf{T}(\mathbf{r},\mathbf{r_0})\mathbf{n}ds \tag{2.26}$$

It is instructive to observe that 2.26 may be obtain directly from 2.25 by dividing the RHS by the viscosity contrast $\lambda$.
Now, let the point $\mathbf{r_0}$ approach the membrane interface either from the external or from the internal side, taking into account an imposed flow $\mathbf{v}^\infty$, we find that both equations 2.25 and 2.26 reduce to the equation:

$$\mathbf{v}(\mathbf{r_0}) = \frac{2}{1+\lambda}\mathbf{v}^\infty + \frac{1}{2\pi\eta_1(1+\lambda)}\int_{mem}\mathbf{f}_{\text{mem}\to\text{flu}}(\mathbf{r})\mathbf{G}(\mathbf{r},\mathbf{r_0})ds + \frac{1-\lambda}{2\pi(1+\lambda)}\int_{mem}^{\mathcal{PV}}\mathbf{v}(\mathbf{r})\mathbf{T}(\mathbf{r},\mathbf{r_0})\mathbf{n}ds \tag{2.27}$$

where $\mathbf{f}_{\text{mem}\to\text{flu}} = -\Delta\mathbf{f} = \mathbf{f}_{in} - \mathbf{f}_{out}$ is the force (per unit area) applied by the membrane interface on the fluid. We recall that $\mathbf{G}$ and $\mathbf{T}$ are the Green's function $\mathbf{G}$ and its associated stress tensor $\mathbf{T}$ for unbounded 2D flow. Their corresponding expressions are given by 2.17 and 2.18. In the following section we will show the main steps to derive the specific Green's functions for the bounded geometry (channel), satisfying the no-slip boundary condition at the bounding walls.

### 2.3.2 Green's functions between two parallel plane walls

We first consider the flow in an unbounded domain due to a Stokeslet with a given force $\mathbf{f}$ located at $\mathbf{r_0} = (x_0, y_0)$ and recalling the two-dimensional Oseen tensor (equation 2.17):

$$\mathbf{G}_{ij}(\mathbf{r},\mathbf{r_0}) = -\delta_{ij}\ln|\mathbf{r}-\mathbf{r_0}| + \frac{(\mathbf{r}-\mathbf{r_0})_i(\mathbf{r}-\mathbf{r_0})_j}{(\mathbf{r}-\mathbf{r_0})^2} \tag{2.28}$$

We seek for the corresponding Green's function $\mathbf{G^{2W}}$ in the presence of the walls (Figure 2.2) which we decompose into a fundamental component $\mathbf{G^F}$ and a complementary component $\mathbf{G^C}$ (the reason will become clear later in this section):

$$\mathbf{G}^{2W} = \mathbf{G}^F + \mathbf{G}^C \tag{2.29}$$

Considering the sum over all images of the Stokeslet with respect to the two walls, we obtain:

$$\mathbf{G}^F_{ij}(\mathbf{r},\mathbf{r_0}) = \sum_{n=-\infty}^{n=+\infty}\left(-\delta_{ij}\ln|\mathbf{r}-\mathbf{r_n}|\frac{(\mathbf{r}-\mathbf{r_n})_i(\mathbf{r}-\mathbf{r_n})_j}{(\mathbf{r}-\mathbf{r_n})^2}\right) - \sum_{n=-\infty}^{n=+\infty}\left(-\delta_{ij}\ln|\mathbf{r}-\mathbf{R_n}| + \frac{(\mathbf{r}-\mathbf{R_n})_i(\mathbf{r}-\mathbf{R_n})_j}{(\mathbf{r}-\mathbf{R_n})^2}\right) \tag{2.30}$$

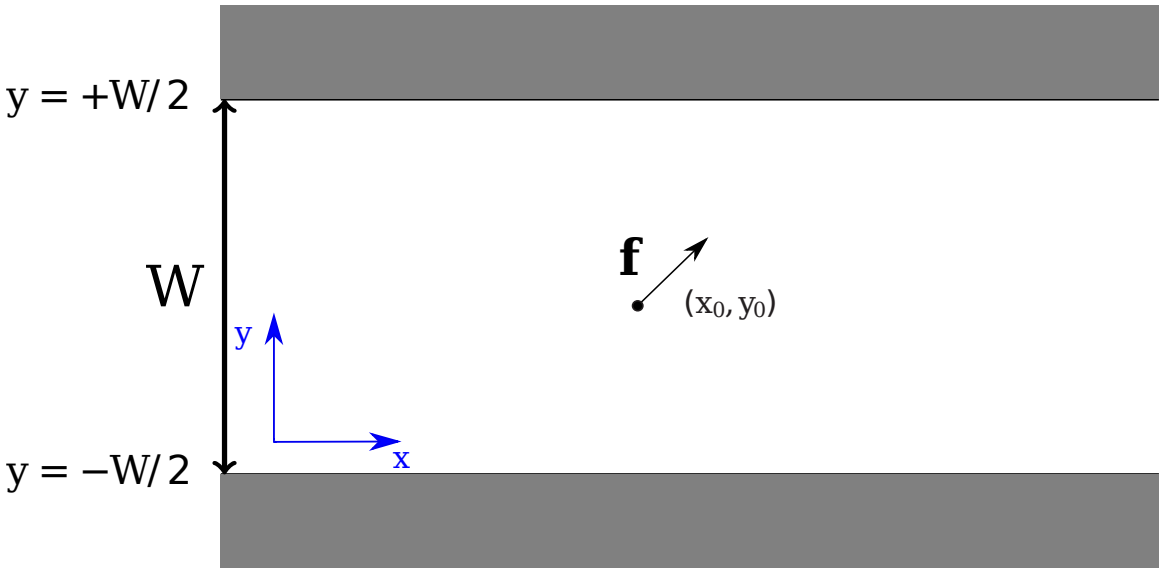


Figure 2.2: A point force $\mathbf{f}$ in a channel confined by two parallel walls.

where

$$\mathbf{r_n} = (x_0, y_0 + 2nW) \qquad \text{and} \qquad \mathbf{R_n} = (x_0, -y_0 - W + 2nW) \tag{2.31}$$

The location of the first set of images are sketched in Figure (2.3). The first sum on the RHS of 2.30 contains the point force and its images which have the same sign as the source force (green points in Figure 2.3), whereas the second sum contains the images of the point force which have the opposite sign as the source force (red points in Figure 2.3). As $n$ tends to infinity, both sums on the RHS of 2.30 diverge. In order to overcome this problem (divergence), we use the following summation formula [Lamb, 1993]:

$$\sum_{n=-\infty}^{n=+\infty} \ln \mathbf{r_n} = \frac{1}{2} \ln \Big( \cosh(x - x_0) - \cos(y - y_0) \Big) + \frac{1}{2} \ln 2 \tag{2.32}$$

The term $\frac{1}{2} \ln 2$ on the RHS of 2.32 was added so that close to a pole the Green's function reduces to the Stokslet. Without loss of generality, we can take the abscissa of $\mathbf{r_0}$ as the origin. The fundamental Green's function is then expressed as:

$$\mathbf{G}^F(x, y; 0; y_0) = \frac{1}{2} \left( \mathbf{G}\Big(\frac{x}{W}, \frac{y - y_0}{W}\Big) - \mathbf{G}\Big(\frac{x}{W}, \frac{y + y_0 - W}{W}\Big) \right) \tag{2.33}$$

With

$$\mathbf{G}(x, y) = \begin{pmatrix} -\ln[f(x,y)] + g(x,y) & h(x,y) \\ h(x,y) & -\ln[f(x,y)] - g(x,y) \end{pmatrix} \tag{2.34}$$

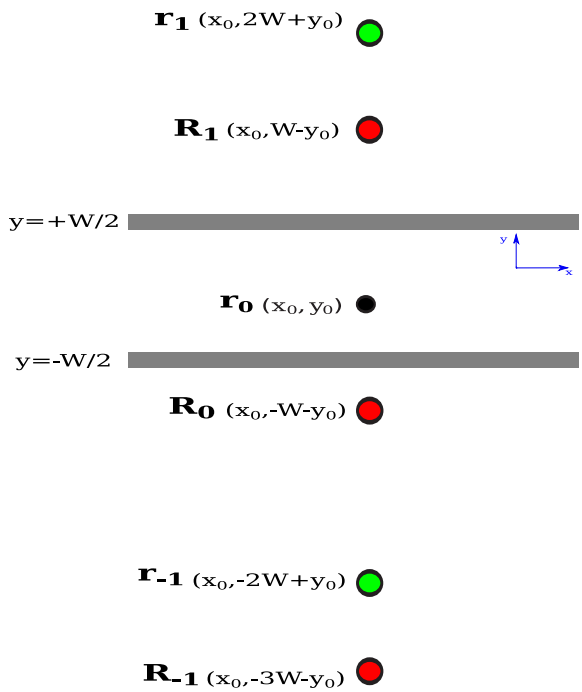


Figure 2.3: Determination of the positions of the few first images.

where $f(x,y) = \cosh(\pi x) - \cos(\pi y)$, $g(x,y) = (\pi x)\sinh(\pi x)/f(x,y)$ and $h(x,y) = (\pi x)\sin(\pi y)/f(x,y)$.
Evaluating the equation 2.33 at the boundaries ($y = \pm W/2$) we find:

$$\begin{aligned} \mathbf{G}^F_{xy}(x, \frac{W}{2}; 0, y_0) &= \mathbf{G}^F_{yx}(x, \frac{W}{2}; 0, y_0) \\ &= \frac{\pi x}{W} \frac{\cos(\pi y_0/W)}{\cosh(\pi x/W) - \sin(\pi y_0/W)} \end{aligned} \tag{2.35}$$

$$\begin{aligned} \mathbf{G}^F_{xy}(x, -\frac{W}{2}; 0, y_0) &= \mathbf{G}^F_{yx}(x, -\frac{W}{2}; 0, y_0) \\ &= -\frac{\pi x}{W} \frac{\cos(\pi y_0/W)}{\cosh(\pi x/W) + \sin(\pi y_0/W)} \end{aligned} \tag{2.36}$$

while diagonal terms ($\mathbf{G}^F_{xx}$ and $\mathbf{G}^F_{yy}$) vanish exactly on the walls.

Because the non-diagonal terms do not vanish at the walls (2.35 and 2.36), $\mathbf{G}^F$ is not sufficient to take into account the no-slip condition on the walls. An additional tensor has to be added in order to fulfill the required boundary conditions. The latter is the reason why we have decomposed $\mathbf{G}^{2W}$ into a fundamental component $\mathbf{G}^F$ and a complementary component $\mathbf{G}^C$ (equation 2.29). $\mathbf{G}^C$ must satisfy the following

boundary conditions on the walls:

$$\mathbf{G}^C_{xx}(y = \pm W/2) = \mathbf{G}^C_{yy}(y = \pm W/2) = 0 \tag{2.37}$$

$$\mathbf{G}^C_{xy}(y = \pm W/2) = \mathbf{G}^C_{yx}(y = \pm W/2) = -\mathbf{G}^F_{xy}(y = \pm W/2) \tag{2.38}$$

For convenience, the complementary component $\mathbf{G}^C$ is obtained in the reciprocal space [Pozrikidis, 1992, p. 98]. As usual, direct and inverse Fourier transforms are defined as:

$$\begin{aligned} f_k &= \int_{-\infty}^{+\infty} \mathrm{d}x f \exp(-ikx) \\ f &= \int_{-\infty}^{+\infty} \frac{\mathrm{d}k}{2\pi} f_k \exp(ikx). \end{aligned} \tag{2.39}$$

where $f$ stands for any components of the Green tensors. By inverse Fourier transform, $\mathbf{G}^C$ in real space is determined numerically using the inverse fast Fourier transform subroutines. We then store large data arrays and after homothetic transformations on coordinates (channel width), we obtain the desired Green's function. The complementary component $\mathbf{G}^C$ is added to fundamental component $\mathbf{G}^F$ in order to obtain the full desired Green's function.

By injecting the new Green's functions, which take into account the no-slip conditions on the walls, in the equation 2.27, we end up with the main equation to be solved numerically. Now that we have built the model, we will analyze it for RBCs in different situations.

### 2.3.3 Other alternative of Green's function

Simulations with high concentrations are a burden to the previous presented code where the efficiency and the accuracy are diminished. To overcome this limitation, we use an ad-hoc Green's function using another code developed by Alexander Farutin, a researcher in our group. Here we briefly describe this alternative.

We represent the membrane position $\mathbf{X}$ by a Fourier series defined on the complex plane:

$$X_x(s) + iX_y(s) = \sum_{k=-k_{max}}^{k_{max}} X_k \exp\left(2\pi iks\right) \tag{2.40}$$

whre $s$ is a curvilinear coordinate, the complex amplitudes $X_k$ are the shape parameters of the membrane. The velocity at any point $\mathbf{r}'$ in the domain can be calculated by the boundary integral equation:

$$\begin{aligned} \Lambda(\mathbf{r})\mathbf{v}(\mathbf{r}') =& \mathbf{v}^\infty(\mathbf{r}') + \frac{1}{\eta_{out}} \int_{mem} \mathbf{f}_{\text{mem}\to\text{flu}}(r) \cdot \mathcal{G}(\mathbf{X}(s), \mathbf{r}')ds \\ &+ (1-\lambda) \int_{mem} \mathbf{v}(\mathbf{X}(s)) \cdot \mathcal{T}(\mathbf{X}(s), \mathbf{r}) \cdot \mathbf{n}(\mathbf{X}(s))ds \end{aligned} \tag{2.41}$$

where $\mathcal{G}$ and $\mathcal{T}$ are the single and double layer Green's functions (they are different from those presented in last section, see below), respectively, and the integrals are carried out along all vesicles in the calculation domain. The coefficient $\Lambda$ is defined as

$$\Lambda(\mathbf{r}) = \begin{cases} \lambda, & \text{if } \mathbf{r}' \text{ is inside the vesicle} \\ (1+\lambda)/2, & \text{if } \mathbf{r}' \text{ is on a membrane} \\ 1, & \text{if } \mathbf{r}' \text{ is outside of any vesicles} \end{cases} \tag{2.42}$$

The numerical procedure employs another Green's function which satisfies only periodic condition denotes as $\mathbf{G}_p$ and $\mathbf{T}_p$ [Pozrikidis, 1992]. The no-slip boundary condition on the walls is imposed through a numerical procedure. The procedure consists in representing the force and the residual velocity on the walls as a Fourier series. The residual wall velocity, here is the velocity on the walls calculated using Eqn. (2.41) with its Green's function being replaced by $\mathbf{G}_p$ and $\mathbf{T}_p$. The Fourier components of the residual wall velocities as well as the wall forces are calculated through explicit expressions and linear equations with explicit coefficients, respectively [Pozrikidis, 1992]. After this, the velocity contribution from wall forces to vesicles is added to the vesicle velocities using $\mathbf{G}_p$ and $\mathbf{T}_p$. This procedure is also done in Fourier space with explicit expressions [Pozrikidis, 1992].

An additional procedure was performed in order to ensure long-term stability of the simulations. A small correction of membrane positions was performed when two particles approach each other too closely (considered as a collision). The correction starts to act only when the distance between the particles' membranes is below a certain limit $\delta h$. The correction pushes the particles apart, thus preventing numerical instabilities from particle interpenetration.

In order to eliminate numerical artifacts, several confirmatory simulations were performed with more refined meshes in time steps, sampling points, Fourier harmonics and critical inter-particle distance $\delta h$. Based on this verification and a compromise between efficiency and accuracy, each particle was characterized by 63 Fourier harmonics. 2048 sampling points were used to resolve the short-range hydrodynamics interactions. The velocity of the particle membrane was calculated at 128 sampling points. The minimal distance $\delta h$ for which the particles were unaffected by the collision-preventing procedure was 0.005 of the particle radius.

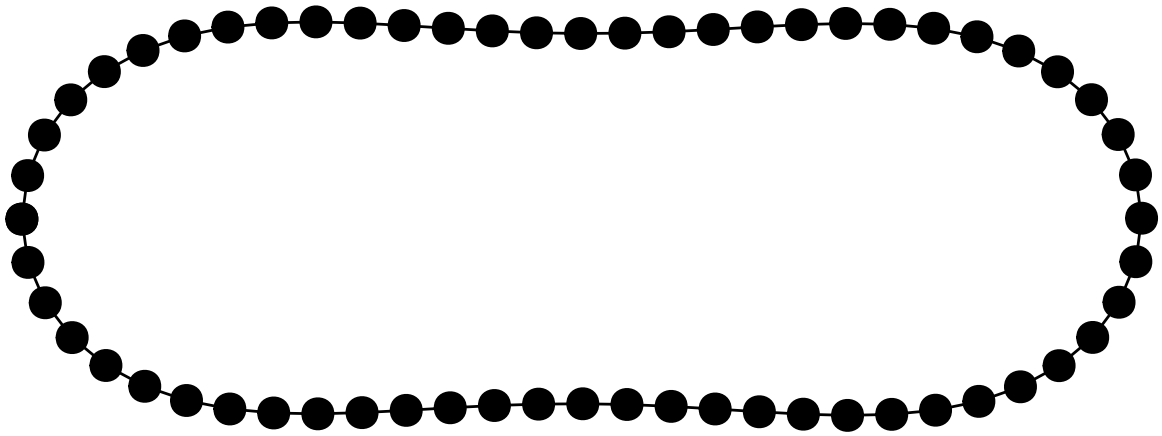

Figure 2.4: Schematic showing the discretization points of the membrane.

## 2.4 Numerical procedure

The displacement in the course of time of the vesicle membranes is obtained by updating the discretization points of the membrane (see Figure 2.4) after each time iteration, using a simple fixed time step Euler scheme, $\mathbf{r}_0(t+dt) = \mathbf{v}(t)dt + \mathbf{r}_0(t)$. Here $\mathbf{v}(t)$ is obtained using the equation 2.27 with the specific Green's functions, after evaluating the membrane force at every points. The main steps performed to get the vesicle dynamics are shown in Figure 2.5.

## 2.5 Derivation of Batchelor's equation

In this section we shall derive the expressions of the rheological quantities considered in this thesis, namely: the normalized effective viscosity $[\eta]$ (in the literature, we call it also *intrinsic viscosity*) and the normal stress difference $N$.

### 2.5.1 Expression of the averaged total stress $< \sigma_{ij}^T >$

Let's consider a suspension of vesicles as in Figure 2.1. The stress tensor $\boldsymbol{\sigma}^T$ of the suspension is a sum of two contributions:

$$\boldsymbol{\sigma}^T = \boldsymbol{\sigma}^F + \boldsymbol{\sigma}^M \tag{2.43}$$

The first term $\boldsymbol{\sigma}^F$ takes into account viscous forces which act in Newtonian fluids. The second one $\boldsymbol{\sigma}^M$ takes into account forces applied by vesicle membranes on Newtonian

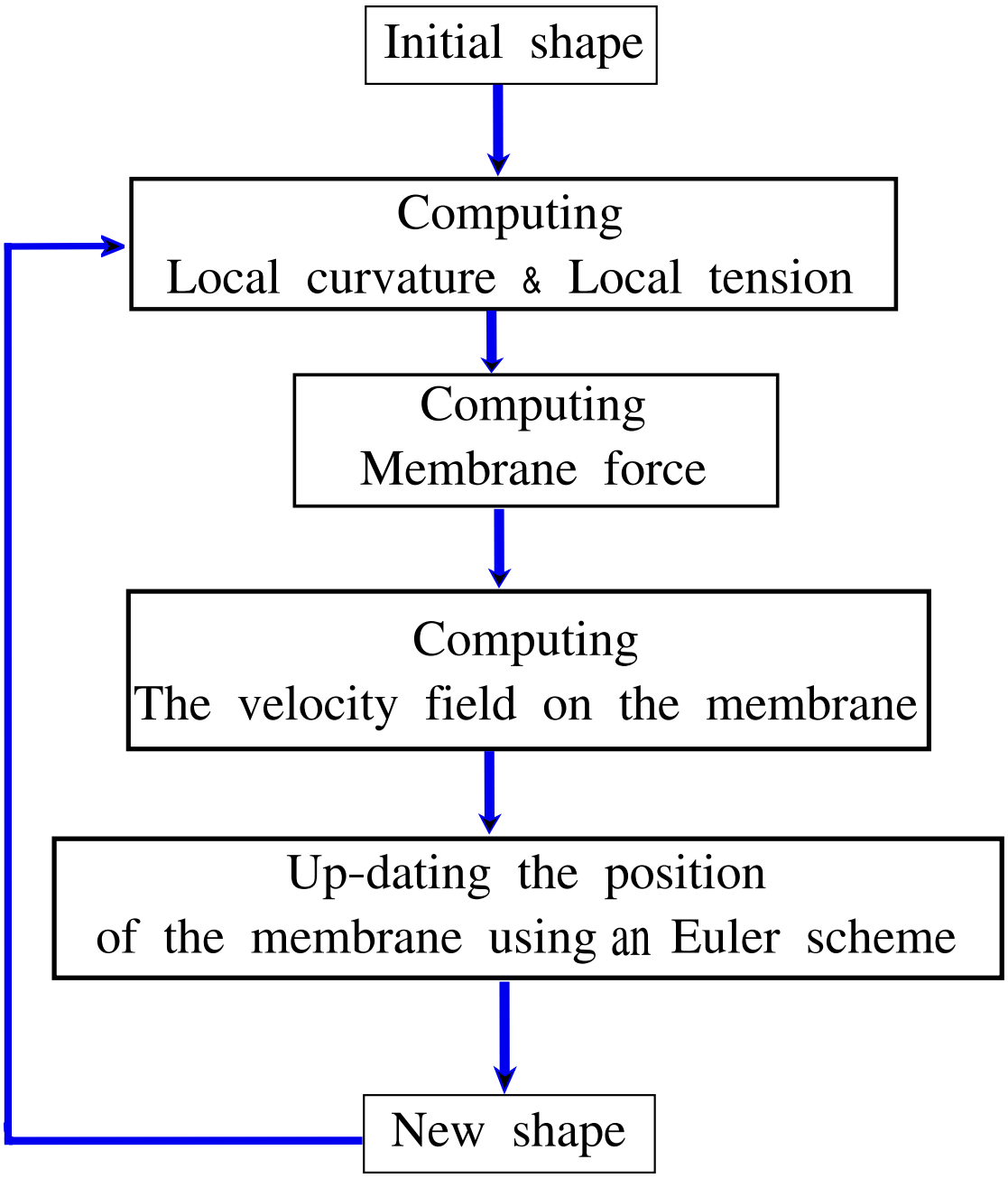


Figure 2.5: Flowchart showing the main steps carried out to get the vesicle dynamics.

fluids.

$$\sigma_{ij}^F = -p\delta_{ij} + \eta(\partial_i v_j + \partial_j v_i) \tag{2.44}$$

$$\nabla.\boldsymbol{\sigma}^M = \mathbf{f}_{\text{mem}\to\text{flu}}\delta(\mathbf{r} - \mathbf{r}_{\text{mem}}) \tag{2.45}$$

We evaluate the expression of $< \sigma_{ij}^F >$ using the well-known equality $\partial_k(x_j\sigma_{ik}) = \sigma_{ij} + x_j\partial_k\sigma_{ik}$, we get the average volume value of $\sigma_{ij}^F$ (at the end we switch to our 2D case):

$$\begin{aligned}
< \sigma_{ij}^F > &= \frac{1}{V}\int_{V_{\text{tot}}} \mathrm{d}V\, \sigma_{ij}^F \\
&= \frac{1}{V}\int_{V_{\text{out}}} \mathrm{d}V\, \sigma_{ij}^F + \frac{1}{V}\int_{V_{\text{in}}} \mathrm{d}V\, \sigma_{ij}^F \\
&= \frac{1}{V}\int_{\text{walls}} \mathrm{d}S\, x_j f_{\text{walls}\to\text{flu},i} - \frac{1}{V}\int_{\text{mem}} \mathrm{d}S\, x_j \sigma_{ik}^{F,out} n_k + \frac{1}{V}\int_{\text{mem}} \mathrm{d}S\, x_j \sigma_{ik}^{F,in} n_k \\
&\quad \text{with} \quad f_{\text{flu}\to\text{mem},i} = (\sigma_{ik}^{F,out} - \sigma_{ik}^{F,in})n_k \\
&=< \sigma_{ij}^T > - \frac{1}{V}\int_{\text{mem}} \mathrm{d}S\, x_j f_{\text{flu}\to\text{mem},i}
\end{aligned} \tag{2.46}$$

Therefore

$$< \sigma_{ij}^T > =< \sigma_{ij}^F > + \frac{1}{V}\int_{\text{mem}} \mathrm{d}S\, x_j f_{\text{flu}\to\text{mem},i} \tag{2.47}$$

Secondly, we can benefit from the explicit expression of $\sigma_{ij}^F$ to obtain another expression of $< \sigma_{ij}^F >$.

$$\begin{aligned}
< \sigma_{ij}^F > &= \frac{1}{V}\int_{V_{\text{out}}} \mathrm{d}V\, \sigma_{ij}^F + \frac{1}{V}\int_{V_{\text{in}}} \mathrm{d}V\, \sigma_{ij}^F \\
&= -\frac{1}{V}\int_{V_{\text{tot}}} \mathrm{d}V\, p\delta_{ij} + \frac{\eta_{\text{out}}}{V}\int_{V_{\text{out}}} \mathrm{d}V\, (\partial_i v_j + \partial_j v_i) + \frac{\eta_{\text{in}}}{V}\int_{V_{\text{in}}} \mathrm{d}V\, (\partial_i v_j + \partial_j v_i) \\
&= -\frac{1}{V}\int_{V_{\text{tot}}} \mathrm{d}V\, p\delta_{ij} + \frac{\eta_{\text{out}}}{V}\int_{V_{\text{tot}}} \mathrm{d}V\, (\partial_i v_j + \partial_j v_i) + \frac{\eta_{\text{out}}(\lambda - 1)}{V}\int_{V_{\text{in}}} \mathrm{d}V\, (\partial_i v_j + \partial_j v_i) \\
&\quad \text{with } \lambda = \eta_{\text{in}}/\eta_{\text{out}}, \\
&= -\frac{1}{V}\int_{V_{\text{tot}}} \mathrm{d}V\, p\delta_{ij} + \frac{\eta_{\text{out}}}{V}\int_{V_{\text{tot}}} \mathrm{d}V\, (\partial_i v_j + \partial_j v_i) + \frac{\eta_{\text{out}}(\lambda - 1)}{V}\int_{\text{mem}} \mathrm{d}S\, (n_i v_j + n_j v_i)
\end{aligned} \tag{2.48}$$

Finally,

$$\boxed{\begin{aligned}
< \sigma_{ij}^T > =& \frac{1}{V}\int_{V_{\text{tot}}} \Big( - p\delta_{ij} + \eta_{\text{out}}\,(\partial_i v_j + \partial_j v_i)\Big)\mathrm{d}V + \frac{1}{V}\int_{\text{mem}} \mathrm{d}S\, x_j f_{\text{flu}\to\text{mem},i} \\
&+ \frac{\eta_{\text{out}}(\lambda - 1)}{V}\int_{\text{mem}} \mathrm{d}S\, (n_i v_j + n_j v_i)
\end{aligned}} \tag{2.49}$$

Here $f_{\text{mem}\to\text{flu},i} = -f_{\text{flu}\to\text{mem},i}$ is the $ith$ component of the force $\mathbf{f}_{\text{mem}\to\text{flu}}$.

### 2.5.2 Expression of the normalized effective viscosity $[\eta]$

In two dimensions, using the equation 2.49, the effective viscosity $\eta_{\text{eff}}$ is given by:

$$\begin{aligned}\eta_{\text{eff}} &= \frac{< \sigma_{xy}^T >}{\dot{\gamma}} \\ &= \eta_{\text{out}} + \frac{1}{S\dot{\gamma}} \int_{\text{mem}} \mathrm{d}s\, y f_{\text{flu}\to\text{mem},x} + \frac{\eta_{\text{out}}(\lambda-1)}{S\dot{\gamma}} \int_{\text{mem}} \mathrm{d}s\, (n_x v_y + n_y v_x)\end{aligned} \tag{2.50}$$

with $S = L \times W$. Thus,

$$\boxed{[\eta] \equiv \frac{\eta_{\text{eff}} - \eta_{\text{out}}}{\eta_{\text{out}}\phi} = \frac{1}{nA\eta_{\text{out}}\dot{\gamma}} \left( \int_{\text{mem}} \mathrm{d}s\, y f_{\text{flu}\to\text{mem},x} + \eta_{\text{out}}(\lambda-1) \int_{\text{mem}} \mathrm{d}s\, (n_x v_y + n_y v_x) \right)} \tag{2.51}$$

Where $n$ is the number of vesicles each with an area $A$.

## 2.6 The normal stress difference

In two dimensions, using the equation 2.49, the normal stress difference is given by:

$$\boxed{\begin{aligned} N &= < \sigma_{xx}^T > - < \sigma_{yy}^T > \\ &= \frac{1}{S} \int_{\text{mem}} \mathrm{d}s\, (x f_{\text{flu}\to\text{mem},x} - y f_{\text{flu}\to\text{mem},y}) + \frac{2\eta_{\text{out}}(\lambda-1)}{S} \int_{\text{mem}} \mathrm{d}s\, (n_x v_x - n_y v_y) \end{aligned}} \tag{2.52}$$

# Chapter 3

# Shear-thinning and shear-thickening of a confined suspension of vesicles

In this chapter, we carry out 2D simulations of a vesicle suspension in confined shear flow to study the shear rate dependence of viscosity. The introduction of this work is given in Section 3.1. Section 3.2 contains the main results and their discussion. We discuss the shear-thinning and shear-thickening behaviors and their origins, as well as the transition from shear-thinning to shear-thickening. Section 3.3 is devoted to the conclusion and perspectives.

## 3.1 Introduction

Blood rheology, which includes its non-Newtonian characteristics, is important for both diagnosis and treatment. As we have stated in the first chapter, many models have been used to characterize the rheology of blood flow. However, these models are based on assumptions that are difficult to validate or justify. Up until now, the general strategy has consisted in adding progressively new ingredients, such as generalized models with shear-rate dependent viscosity, yield-stress behaviors, elastic stress..., in order to account for diverse properties of blood flow, which depend on regimes of flow strength.

As for any complex fluid [Larson, 1999], the rheology of blood escapes the traditional laws for simple fluids. Its complex character stems from an intimate link between the microscales (carried by RBC shapes and dynamics) and macroscales. In principle, a firm understanding of rheology should emerge by explicitly taking RBC shapes and dynamics into consideration. The increase in computational power

combined with the development of many numerical techniques has opened the way towards numerical studies of blood flow properties by allowing to account for several hundreds or thousands of cells at a time. Many studies have been devoted to the rheology of dilute suspensions of vesicles or capsules (another model of elastic shells mimicking RBC), theoretically [Misbah, 2006, Vlahovska and Gracia, 2007, Danker and Misbah, 2007a], numerically [Ghigliotti et al., 2009, Ghigliotti et al., 2010, Doddi and Bagchi, 2009, Bagchi and Murthy, 2009, Bagchi and Kalluri, 2010, Lamura and Gompper, 2015, Thiébaud and Misbah, 2013] and experimentally [Kantsler and Steinberg, 2005, Vitkova et al., 2008]. More recently, several simulations have been devoted to the study of more concentrated suspensions [Kalluri and Bagchi, 2011, Matsunaga et al., 2014, Reasor et al., 2013, Fedosov et al., 2014, Matsunaga et al., 2016, Thiébaud et al., 2014, Shen et al., 2018].

A less-treated issue concerns rheology in a confined geometry. Recently, the subject was approached [Thiébaud et al., 2014] by submitting a confined suspension to a shear flow. It was reported that the suspension exhibits several ordered structures with an important impact on rheology. For example, the normalized effective viscosity, defined as $[\eta] = \frac{\eta_{eff} - \eta_{out}}{\eta_{out}\phi}$ (with $\eta_{eff}$ the effective viscosity of the suspension, $\eta_{out}$ the viscosity of the ambient fluid and $\phi$ the vesicle concentration) exhibits ample oscillations with respect to $\phi$ and coinciding with the appearance of several ordered structures.

The aforementioned study [Thiébaud et al., 2014] focused on the evolution of rheological properties as a function of concentration $\phi$ and confinement. The viscosity contrast as well as the strength of the flow were kept fixed. Other studies [Kaoui et al., 2014, Lamura and Gompper, 2013] focused on the effect of viscosity contrast $\lambda$ on the dynamics and rheology of vesicle suspensions, while the effect of confinement has been investigated in Ref. [Kaoui et al., 2011] in the absence of a viscosity contrast. The main objective of this chapter is to investigate how does the flow strength as well as the viscosity contrast alter the rheological behavior of a confined suspension of vesicles.

## 3.2 Results

In the present systematic study we look at the rheological properties as a function of shear rate $\dot{\gamma}$ by varying the viscosity contrast $\lambda = \eta_{in}/\eta_{out}$, where $\eta_{in}$ and $\eta_{out}$ are the viscosities of the fluid medium inside and outside the vesicle, respectively. An interesting feature is discovered: the suspension can exhibit both shear-thinning

and shear-thickening depending on $\lambda$ (see below). Unlike the classical shear-thinning effect for blood, which is mostly explained by the shear-induced dissociation of RBC rouleaux (the rest being attributed to the effects of cell deformability), here, no rouleaux are allowed to form due to the absence of any non-hydrodynamic interactions between cells. Instead, the shear-thinning behavior comes exclusively from the way the suspension organizes itself as a function of the shear rate. It is sufficient to modify the viscosity of the enclosed fluid of the vesicles for the rheological behavior of the suspension to switch from shear-thinning to shear-thickening.

We shall consider a 2D suspension of vesicles. A preliminary study presented in [Thiébaud et al., 2014] has shown that the same type of order of the suspended entities takes place also in 3D with the same qualitative behavior regarding the changes of the effective viscosity with the concentration. This is why we believe that the overall behavior presented here should survive in 3D. The efficiency of 2D simulations from the computational time point of view allows one to explore several ranges of parameters in order to identify the relevant regimes of interest.

### 3.2.1 Shear-thinning

We first analyze the effect of the capillary number $C_\kappa$ on the rheology of a vesicle suspension with a viscosity contrast $\lambda = 1$. We recall the first rheological quantity of interest: the normalized effective viscosity $[\eta]$ (equation 2.51) [Thiébaud and Misbah, 2013, Ghigliotti et al., 2010]:

$$[\eta] \equiv \frac{\eta_{\text{eff}} - \eta_{\text{out}}}{\eta_{\text{out}}\phi} = \frac{1}{nA\eta_{\text{out}}\dot{\gamma}} \left( \int_{\text{mem}} \mathrm{d}s\, y f_{\text{flu}\to\text{mem},x} + \eta_{\text{out}}(\lambda - 1) \int_{\text{mem}} \mathrm{d}s\, (n_x v_y + n_y v_x) \right) \tag{3.1}$$

This expression is the extension to vesicles of the Batchelor [Batchelor, 1970] result originally derived for suspensions of rigid particles. The second quantity of interest is the normalized normal stress difference (using equation 2.52):

$$[N] \equiv \frac{\langle \sigma_{xx} \rangle - \langle \sigma_{yy} \rangle}{(\eta_{\text{eff}} - \eta_{\text{out}})\dot{\gamma}}. \tag{3.2}$$

When $\lambda = 1$ (considered in this section), the vesicles exhibit a TT motion (the membrane circulates around the interior of the vesicle). In this case the systematic study of the suspension under different capillary numbers reveals a shear-thinning behavior. The results are shown in Figure 3.1, for the concentrations $\phi = 5.58\%$, $\phi = 9.77\%$, and $\phi = 19.55\%$. It is interesting to note that blood also exhibits a shear-thinning behavior, which is mostly related to dissociation of RBC rouleaux, but here

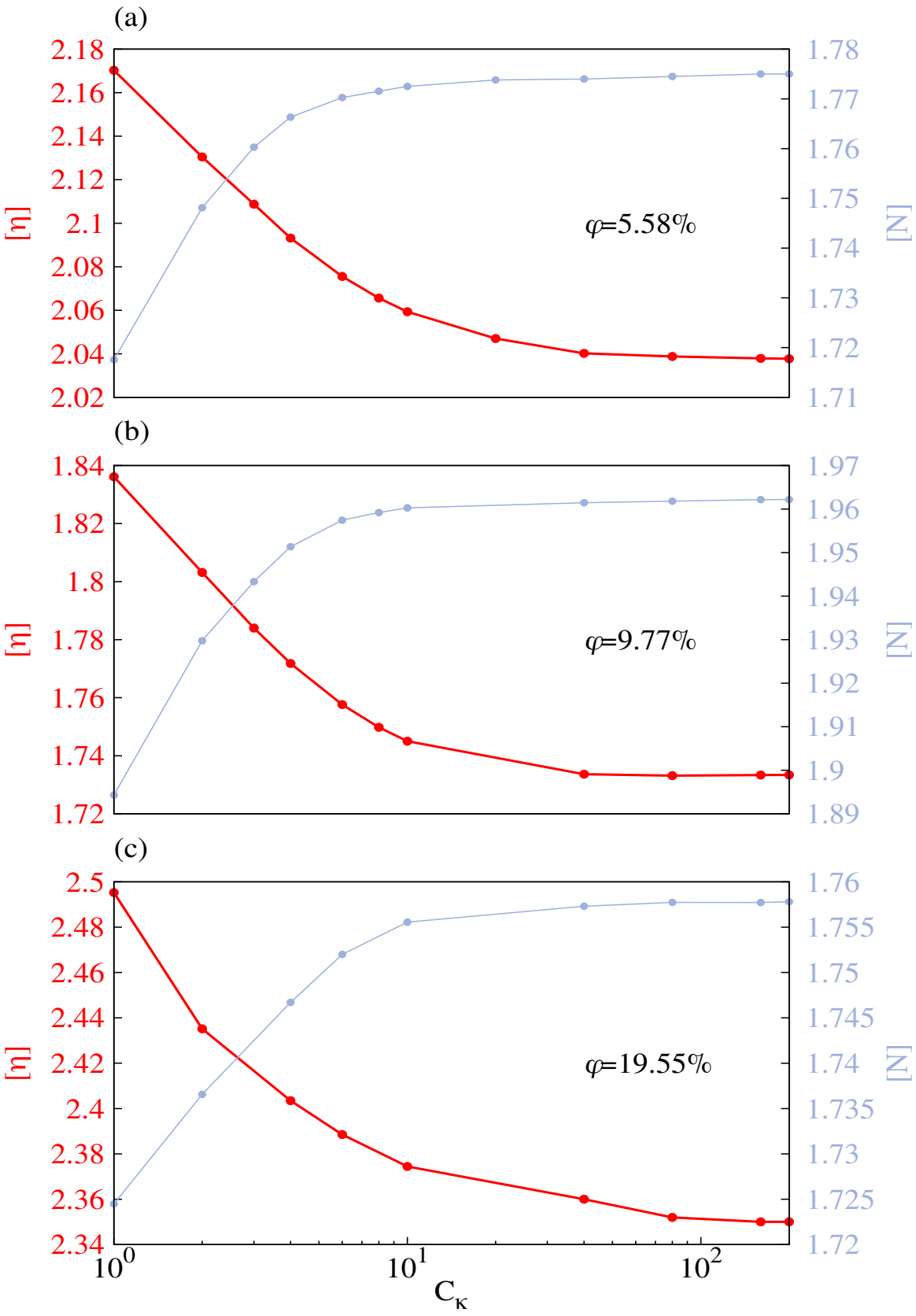


Figure 3.1: The normalized effective viscosity $[\eta]$ and the normalized normal stress difference $[N]$ as a function of capillary number $C_\kappa$ for different concentrations. For all explored concentrations, the suspension exhibits a shear-thinning behavior.

rouleaux are absent from the beginning because we do not include non-hydrodynamic interactions between vesicles in our model. The second source of the shear-thinning behavior of blood was attributed to RBC deformation [Ghigliotti et al., 2010, Forsyth et al., 2011, Lanotte et al., 2016, Chien et al., 1967a]. In the present study, we show that the changes of the orientation angle of the vesicles can also affect the effective viscosity of the suspension. We will see below that the situation is quite subtle since a change of the internal viscosity (without changing the overall nature of the vesicle motion or their spatial organization) will lead to shear-thickening. It is interesting to observe that the overall trend of the shear-thinning/shear-thickening (see below for shear-thickening) behavior is independent of the concentration and of the spatial organization.

Figure 3.2 shows the spatial organization. Each vesicle is pushed by the walls (lateral migration) towards the centerline. Each vesicle at the center interacts hydrodynamically with its neighbors. The analysis of the flow field around the vesicles gives a precise hint towards the organization [Shen et al., 2017]. When the concentration exceeds a certain value (typically $\phi \sim 15\%$, see [Thiébaud et al., 2014]), addition of new vesicles within the single file decreases the equilibrium distance between two neighbors, and then the hydrodynamic interactions between particles become pronounced. Therefore, the single-file arrangement becomes unstable against the formation of a two-file structure.

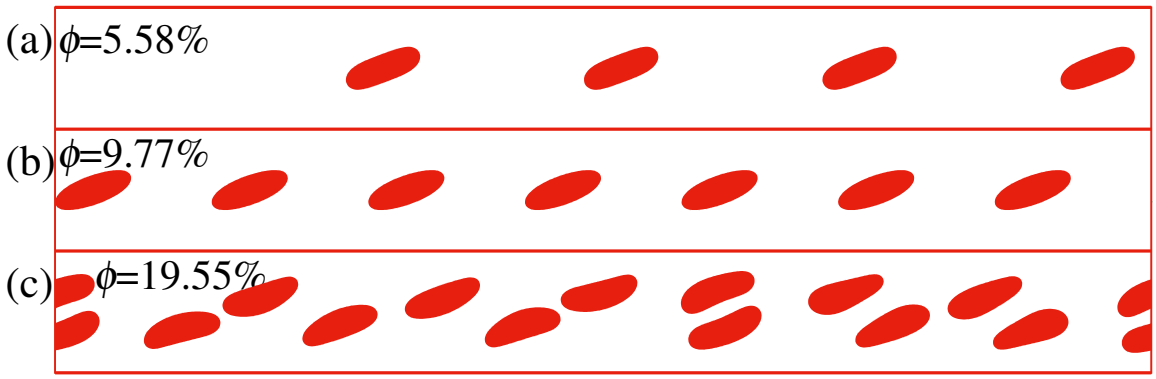


Figure 3.2: Typical configurations of a suspension of vesicles for several concentration $\phi$ and typical capillary numbers $C_\kappa$. $(a)$: $C_\kappa = 3$ $(b)$: $C_\kappa = 80$ $(c)$: $C_\kappa = 10$.

Note in Figure 3.1 that the normalized effective viscosity (for a given $C_\kappa$) is not monotonous with concentration. It is higher for $\phi = 5.58\%$ than for $\phi = 9.77\%$ and

it is smaller for $\phi = 9.77\%$ than for for $\phi = 19.55\%$. This behavior was initially reported in [Thiébaud et al., 2014] and some heuristic explanations put forward.

#### 3.2.1.1 Origins of the shear-thinning behavior

Let us provide now some support to the shear-thinning behavior. The first analysis is based on the streamline structure (Figure 3.3). Those lines are plotted using stream function $\psi(x, y)$, which is introduced by the definitions:

$$v_x = \frac{\partial \psi}{\partial y}, \quad v_y = -\frac{\partial \psi}{\partial x} \tag{3.3}$$

The stream function is constant along the lower wall, according to second equation in (3.3). Consequently, we can write

$$\psi(x_0, y_0) = \int_{-W/2}^{y_0} v_x(x_0, y) dy + C, \tag{3.4}$$

where $C$ is an arbitrary constant independent of $x_0$ and $y_0$. A streamline is defined by equation

$$\psi(x_0, y_0) = K, \tag{3.5}$$

where $K$ is a constant characterizing the streamline. Knowing $v_x$ and $v_y$ from the boundary integral equation, we obtain $\psi$ by calculating the integral (3.4) numerically. Taking a specific desired initial position $(x_0, y_0)$, fixes a given value of $K$. The streamlines are obtained by linking the points which have the same given value of stream function $K$.

In Figure 3.3, the streamlines are more deformed (and this implies higher dissipation) for small capillary number (left panel) than for the higher one (right panel). In the purpose of providing an argument about the possible source of the shear-thinning behavior of these confined suspensions, we can link this phenomenon to the deformation of vesicles. The shape evolution of a vesicle as a function of $C_\kappa$ is shown in Figure 3.4. The key parameter that controls the deformation of vesicle by varying the capillary number $C_\kappa$ is the *Taylor deformation index* $D$ defined as:

$$D = \frac{a - b}{a + b}, \tag{3.6}$$

where $a$ and $b$ are the lengths of the major and minor axes of the vesicle, respectively. It is interesting to note that this parameter decreases with $C_\kappa$ (Figure 3.5), in a marked contrast with the behavior of drops [Kennedy et al., 1994, Barthes-Biesel and Acrivos, 1973]. At equilibrium the vesicle has a biconcave shape. The straining

part of the shear flow tends to align the vesicle along some angle with respect to the flow direction, and this leads to an increase of the long axis of the vesicle. At the same time the short axis expands in order to preserve the constant perimeter by suppressing the dip of the biconcave shape. The expansion of the short axis is larger than that of the long axis, which reduces the Taylor deformation index of the vesicle. The straightening of the concavities and the decrease of the Taylor deformation index means that flow lines inside the vesicle become closer to a circle (Figure 3.3), which reduces the dissipation in the internal fluid. This provides a simple explanation to the shear-thinning behavior.

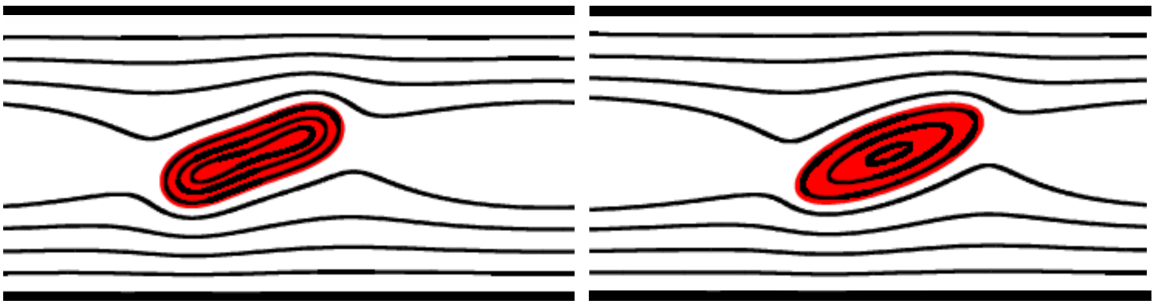

Figure 3.3: Streamlines inside and outside a single vesicle of the suspension for the viscosity contrast $\lambda = 1$, for two capillary numbers: $C_\kappa = 1$ (left) and $C_\kappa = 200$ (right). In this case the inclination angle of the vesicles is almost constant with $C_\kappa$, whereas the shape undergoes some moderate change. Owing to this, the streamlines also deform following the deformation of vesicles. We can see in this case that the streamlines inside and outside of the vesicles are more deformed for lower $C_\kappa$ than for higher $C_\kappa$, in agreement with the shear-thinning behavior. The same set of values of the stream function is used for streamlines in left and right panels.

### 3.2.2 Shear-thickening

An interesting fact is that the same suspension can exhibit a shear-thickening for a different internal viscosity, albeit neither the spatial configuration nor the dynamics of each vesicle is different from the previous case (i.e. each vesicle undergoes a TT motion and the vesicles organize in a regular file).

As we can see in Figure 3.6, the suspension becomes more and more viscous with the capillary number $C_\kappa$. The spatial organization of the vesicles in this case is shown in Figure 3.7. The shear-thickening behavior is present despite the fact that the Taylor deformation index $D$ also decreases (i.e. as in the case where $\lambda = 1$) with $C_\kappa$ (see Figure 3.5, red curve). This means that the behavior of the Taylor deformation index is not the only source of the evolution of the viscosity. We have thus attempted to

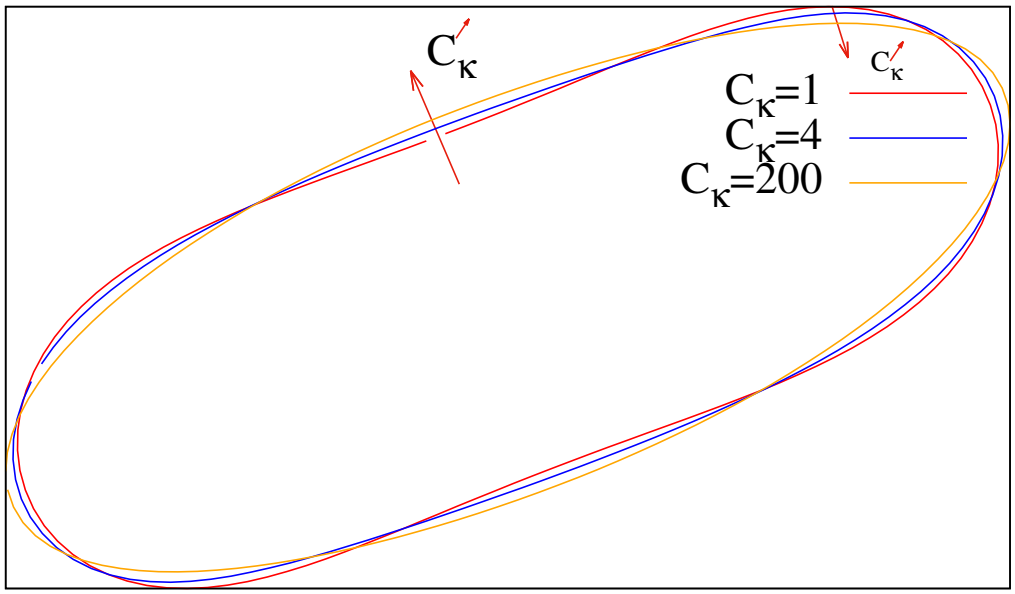


Figure 3.4: Steady contours of a vesicle as a function of the capillary number $C_\kappa$ for a viscosity contrast $\lambda = 1$. The capillary number $C_\kappa$ increases in direction of the arrows.

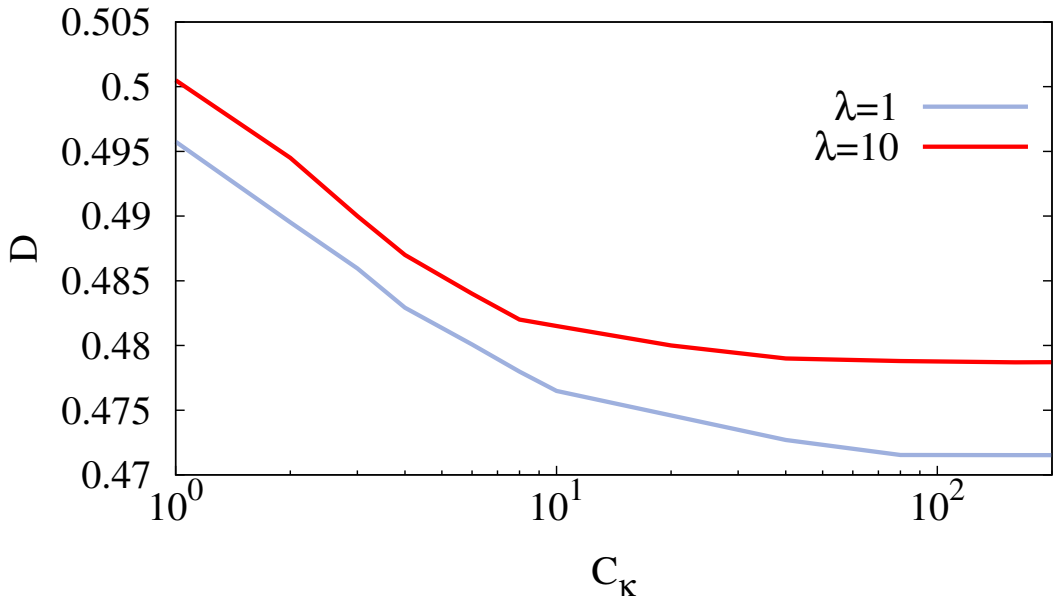


Figure 3.5: The Taylor deformation index $D$ as a function of capillary number $C_\kappa$ for $\lambda = 1$ and $\lambda = 10$ ($\phi = 5.58\%$).

dig further into the reason for this opposite behavior. We found that in this case there are two antagonist effects: (i) the decrease of the Taylor deformation index $D$ with shear rate which leads to shear-thinning (as seen before for $\lambda = 1$), and (ii) a significant increase of the TT angle with shear rate that causes the vesicles to oppose more resistance to the flow, leading to shear-thickening. It turns out that this last effect dominates, leading globally to an increase of the viscosity with the shear rate.

The value $\lambda = 10$ is above the critical value for the transition from TT to tumbling (TB) in the unconfined regime [Ghigliotti et al., 2010]. In the presence of confining walls the transition towards TB occurs at higher values of viscosity contrast $\lambda$, (for $W = 5R_0$, $\lambda_c \approx 10$, [Thiébaud and Misbah, 2013]). It is found here that the shear rate also delays the transition towards TB, in that the shear rate tends to significantly increase the TT angle, as seen below.

#### 3.2.2.1 Effect of the inclination angle

In order to investigate further the reasons causing the shear-thickening behavior, we have analyzed the behavior of the the inclination angle of vesicles $\Psi$ as a function of shear rate, expressed by $C_\kappa$ in dimensionless units, Figure 3.8. Our results show that the angle $\Psi$ increases with $C_\kappa$, meaning that the vesicles behave, upon increasing $C_\kappa$, more and more as obstacles against the flow, leading to a higher flow resistance.

It turns out that the increase of the inclination angle with capillary number is much more pronounced for high viscosity contrast than for low ones. This is a consequence of the fact that for small $\lambda$ the inclination angle is quite close to its maximum possible value, namely $\pi/4$, which corresponds to the elongational direction of the straining part of the shear flow. Thus the change of the deformation parameter when increasing the shear rate has only a minor effect. In contrast, for high enough $\lambda$ (sufficiently close to the tumbling threshold) the inclination angle is small and thus is quite sensitive to variations of the shape of the vesicle which occurs as a function of the capillary number. It follows that an increase of the shear rate, even if it induces a small reduction of the Taylor index, will cause a significant increase of the inclination angle. This tendency continues to operate until the angle has reached a value not too far from the maximum elongation direction of the straining component of the shear flow (see Figure 3.8). In summary, when $\lambda$ is rather small (far below the TT-TB transition), the main effect of the shear rate is the decrease of the Taylor deformation index (leading to shear-thinning). When $\lambda$ is close to the value leading to TT-TB transition, the

effect of the Taylor deformation index is minor, and the main effect arises from an increase of the TT angle.

In order to investigate the evolution of the TT angle as a function of capillary number $C_\kappa$, we plot the absolute difference of the angle for two values of the capillary number, $C_\kappa = 1$ and $C_\kappa = 80$, for several viscosity contrasts (between $\lambda = 1$ and $\lambda = 10$).

As already introduced above, in the case of $\lambda = 1$ the vesicles keep almost a constant TT angle upon increasing the capillary number $C_\kappa$, which leads to an almost zero absolute difference of the angle in this case Figure 3.9. By increasing viscosity contrast $\lambda$, the absolute difference of the TT angle between $C_\kappa = 1$ and $C_\kappa = 80$ is larger and larger as $\lambda$ increases, until it reaches a maximal explored value at $\lambda = 10$, yielding the maximal absolute difference of the angle of about $|\Psi(C_\kappa = 80) - \Psi(C_\kappa = 1)|/\pi \simeq 0.03$. Beyond $\lambda = 10$, for the degree of confinement $C_n = 0.4$, the vesicles undergo a TB motion [Thiébaud and Misbah, 2013], a regime which is outside of the scope of the present study.

Figures 3.10 and 3.11 show the streamlines for two extreme values of the capillary number. The first figure represents the streamlines of the full field, whereas the second one represents that of the induced field (that is the full flow field from which we subtract the imposed shear flow). It is clearly seen that the streamlines are much more squeezed for the higher shear rate, indicating a clear increase of hydrodynamical dissipation, leading to shear-thickening.

For the sake of completeness, we have analyzed the evolution of the angle of a single vesicle and compared to that of a given vesicle in the suspension. This analysis is motivated by the determination of the contribution coming from a single entity, and that arising from the interaction among vesicles. The results are reported in Figure 3.8. It is seen that for a concentration of 5.58% the main effect comes from a single entity, and the effect of the interaction is quite minor.

### 3.2.3 Summary

Finally, it is interesting to note that the range of variation of the normalized effective viscosity for $\lambda = 10$ (Figure 3.6) remains below the range of the same quantity for $\lambda = 1$ (Figure 3.1), despite the fact (i) the fluid is more viscous inside the vesicles in the first case, (ii) the shear rate induces shear-thickening. The first result is consistent with that initially reported in [Misbah, 2006, Danker and Misbah, 2007a] according to which the viscosity decreases for higher and higher viscosity contrast $\lambda$, provided the vesicle still remains in the TT regime. This effect is attributed to the fact that upon

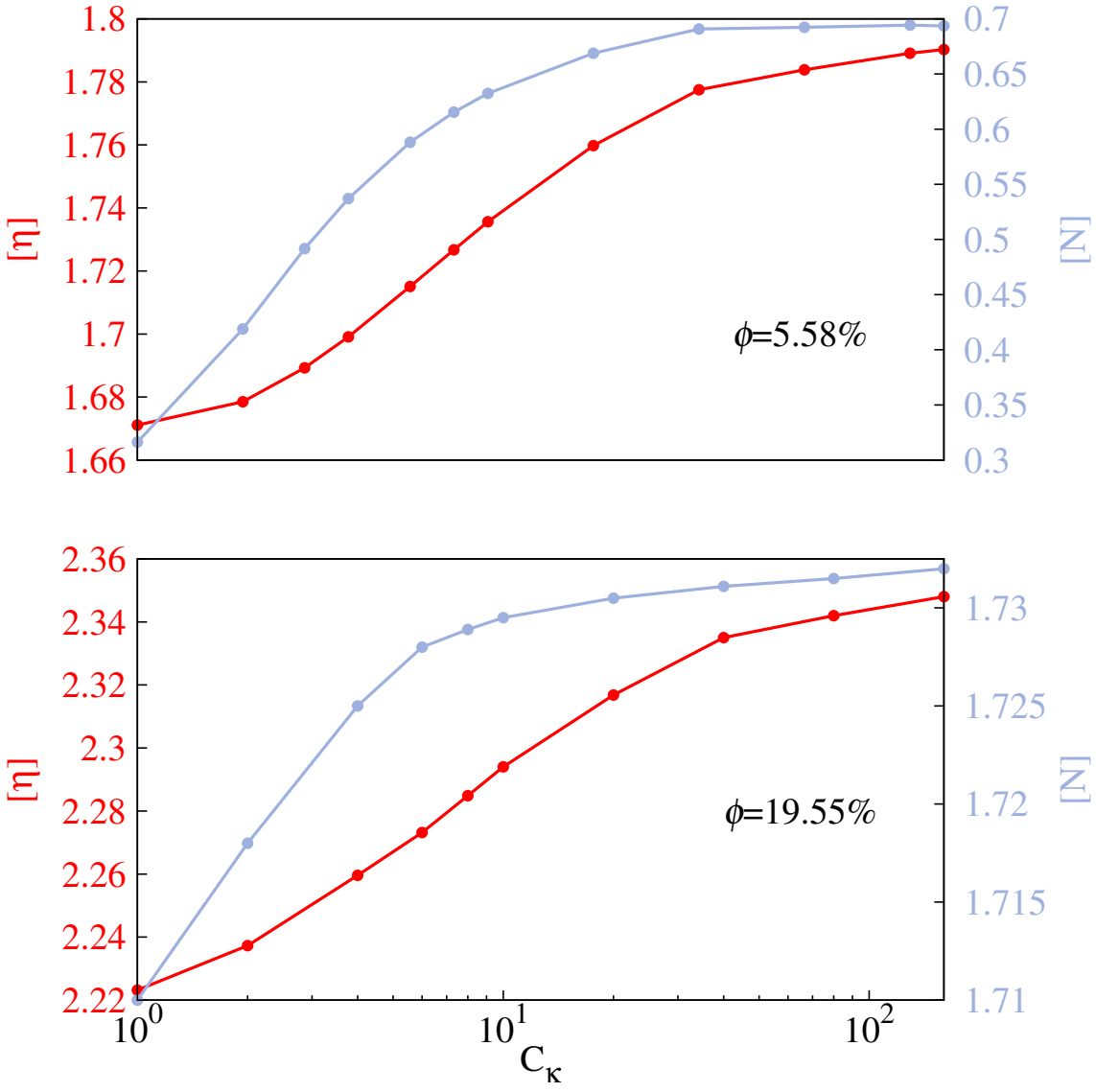


Figure 3.6: The normalized effective viscosity $[\eta]$ and the normalized normal stress difference $[N]$ as a function of capillary number $C_\kappa$ for $\phi = 5.58\%$ and $\phi = 19.55\%$. For all explored concentrations, the suspension exhibits a shear-thickening behavior.

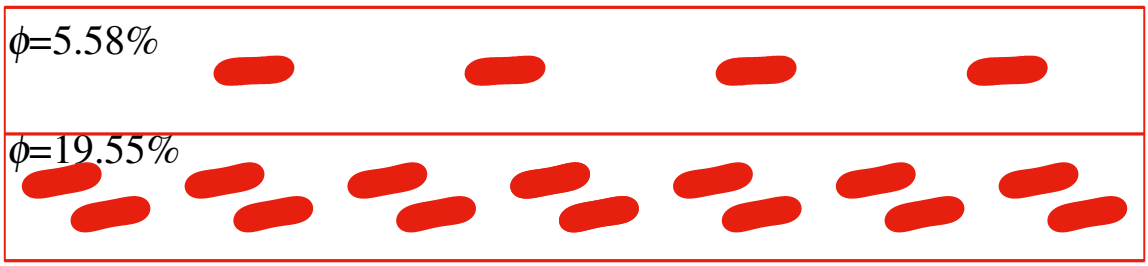


Figure 3.7: Typical configurations of a vesicle suspension. Top: $\phi = 5.58\%$, $C_\kappa = 1$ and $\lambda = 10$. Bottom: $\phi = 19.55\%$, $C_\kappa = 1$ and $\lambda = 10$.

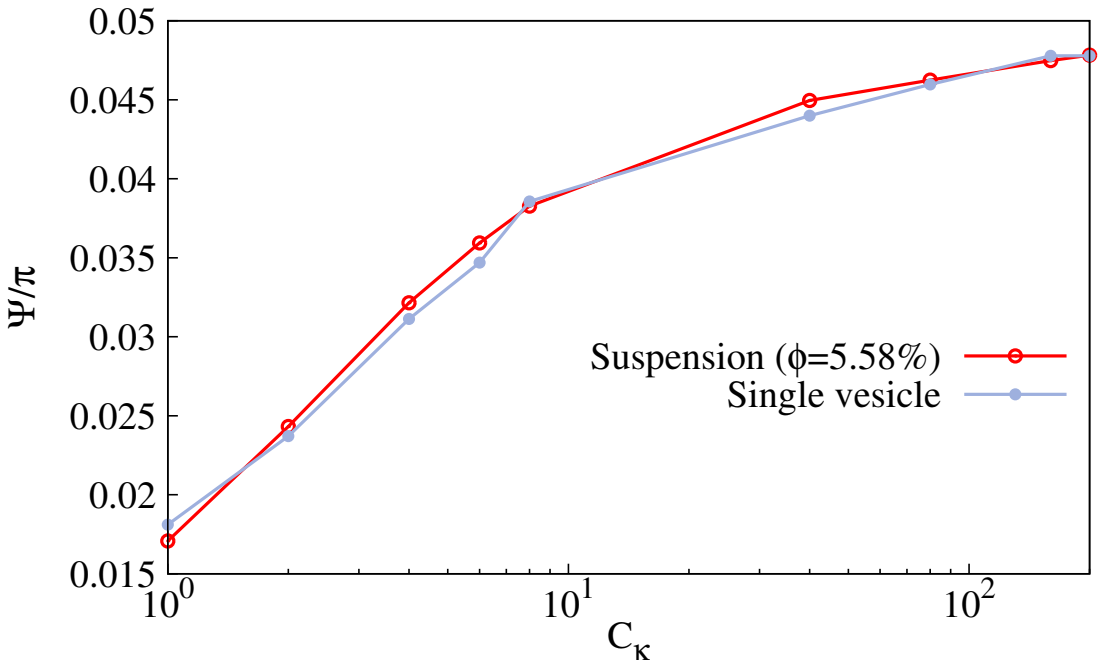


Figure 3.8: Inclination angle of vesicles ($\phi = 5.58\%$) as a function of $C_\kappa$ for a viscosity contrast $\lambda = 10$. The angle increases with $C_\kappa$.

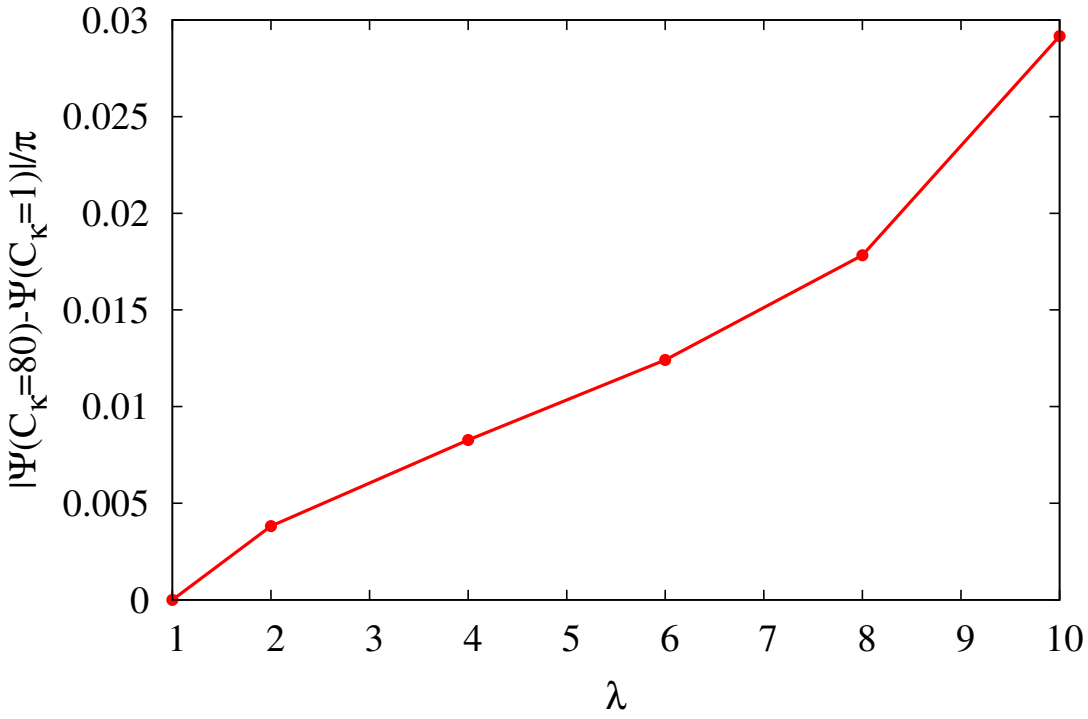


Figure 3.9: Absolute difference of the inclination angle corresponding to two capillary numbers ($C_\kappa = 1$ and $C_\kappa = 80$) as a function of the viscosity contrast $\lambda$.

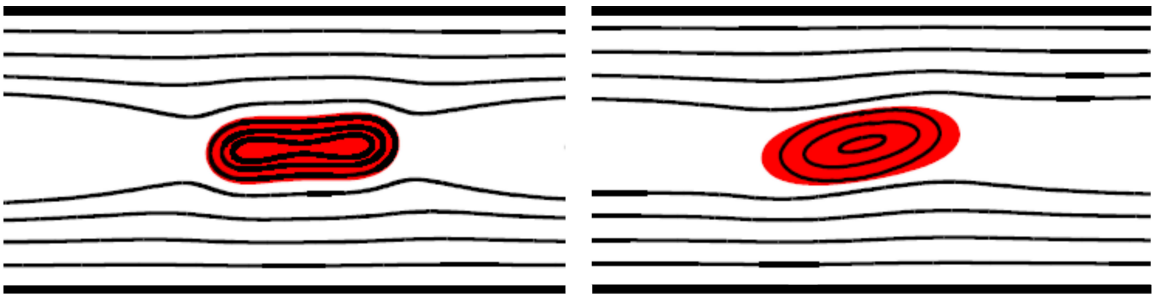

Figure 3.10: Streamlines inside and outside a vesicle for the viscosity contrast $\lambda = 10$, for two capillary numbers: $C_\kappa = 1$ (left) and $C_\kappa = 200$ (right). Here ($\lambda = 10$), the inclination angle increases with $C_\kappa$. The same set of values of the stream function is used for streamlines in left and right panels.

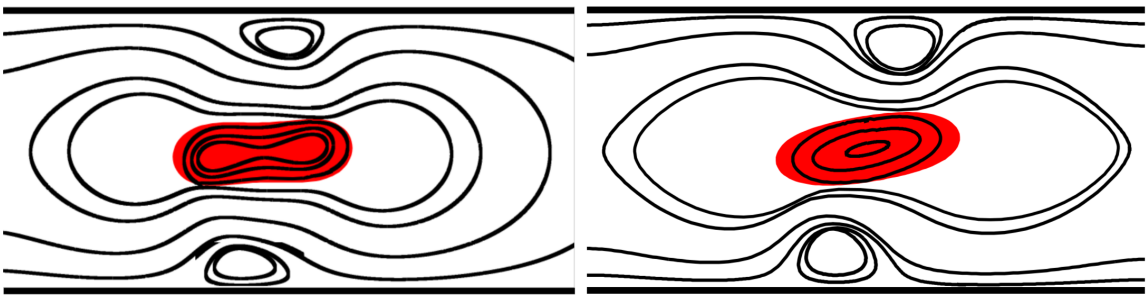

Figure 3.11: Streamlines associated with the induced flow inside and outside a vesicle for $\lambda = 10$, and for two capillary numbers: $C_\kappa = 1$ (left) and $C_\kappa = 200$ (right). The same set of values of the stream function is used for streamlines in left and right panels.

increasing $\lambda$ the inclination angle decreases, and thus the cross section against the fluid flow is reduced, leading to a lower viscosity. For $\lambda = 10$, the vesicle inclination angle is close to zero, and the viscosity attains its minimal value. The shear rate causes the vesicle to straighten up (leading to shear-thickening), but the inclination angle never reaches that obtained at $\lambda = 1$. Thus the normalized effective viscosity for $\lambda = 10$ remains always below that for $\lambda = 1$.

It is noteworthy that the shear-thinning and shear-thickening effects are exhibited by a single vesicle. Figure 3.12 shows the results for a single vesicle for two values of reduced area: $\tau = 0.7$ and $\tau = 0.9$. In both cases we find that the suspension follows the same behavior as for the concentrations shown above. For $\lambda = 1$ the suspension exhibits a shear-thinning behavior and for $\lambda = 10$ the suspension exhibits a shear-thickening behavior. It is interesting also to note that for both cases the Taylor deformation index decreases with $C_\kappa$ and the inclination angle of the vesicle amply increases with $C_\kappa$ for $\lambda = 10$, whereas the increase is minor for $\lambda = 1$. (see Figure 3.13). That this qualitative rheological behavior can be captured by a single vesicle model does not mean that the vesicle-vesicle interaction plays a minor role. Indeed, for a fixed shear rate, the normalized viscosity is a strongly nonlinear function of concentration, as reported in [Thiébaud et al., 2014, Shen et al., 2017].

### 3.2.4 Shear-thinning-shear-thickening crossover

We have seen above that depending on $\lambda$ the same suspension shows either a shear-thinning (low $\lambda$) or shear-thickening (large $\lambda$). The question naturally arises of whether there is a critical $\lambda$ at which the suspension switches from one behavior to the other. For that purpose, we have analyzed the behavior of the normalized

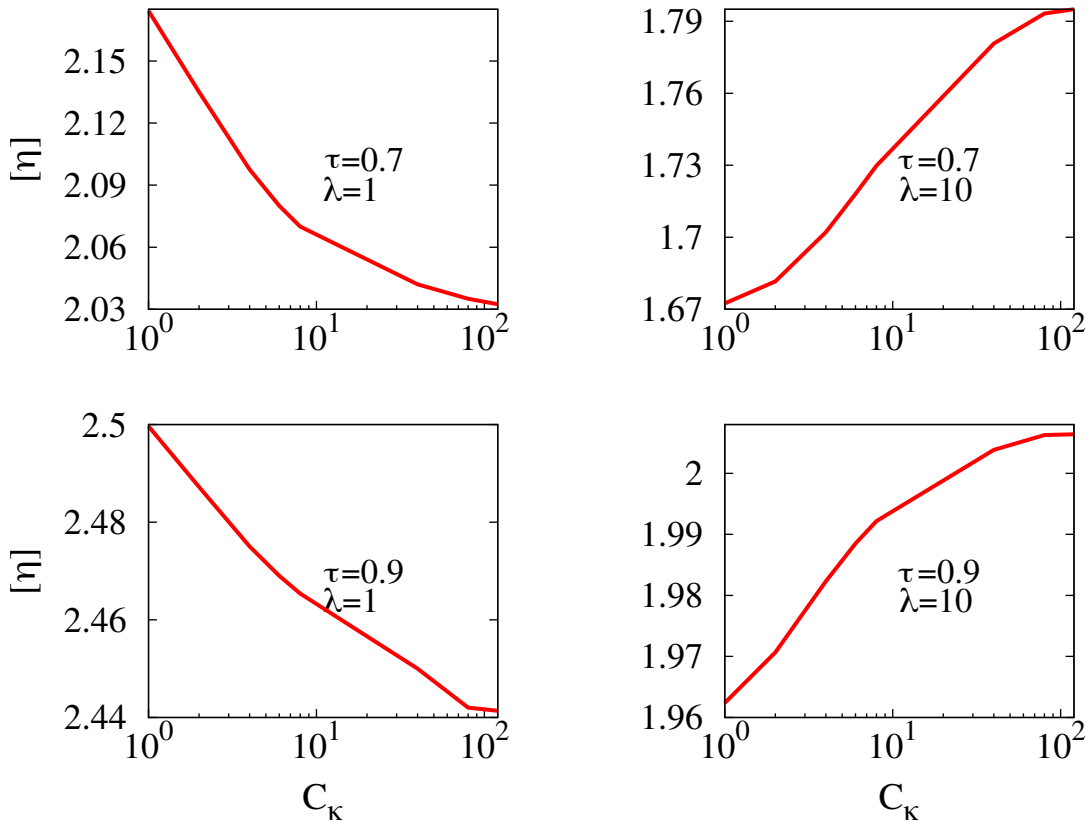


Figure 3.12: The normalized effective viscosity $[\eta]$ as a function of capillary number $C_\kappa$ for a single vesicle for two values of reduced area: $\tau = 0.7$ and $\tau = 0.9$. For $\lambda = 1$ ($\lambda = 10$) the suspension exhibits a shear-thinning (shear-thickening) behavior regardless of the reduced area $\tau$.

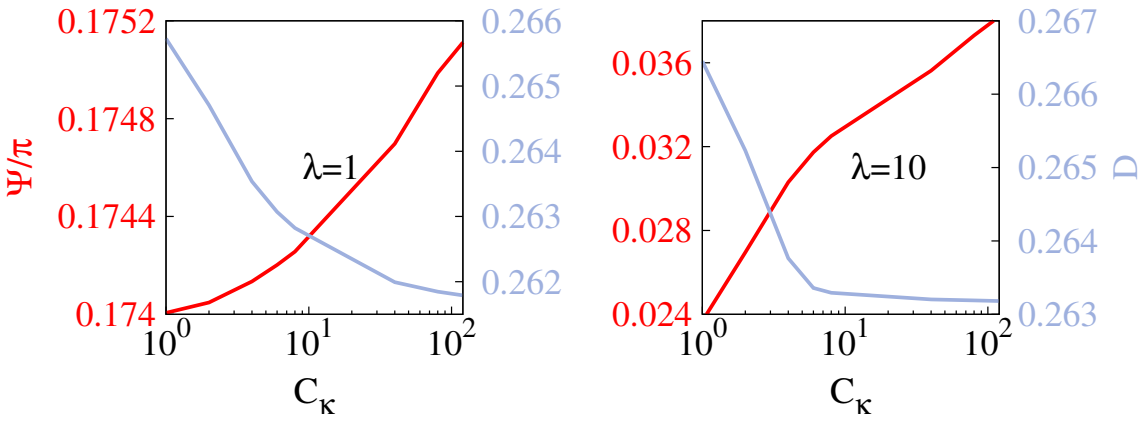


Figure 3.13: The evolution of the Taylor deformation index $D$ and the inclination angle of the vesicle $\Psi$ as a function of capillary number $C_\kappa$ for reduced area $\tau = 0.9$, for two values of viscosity contrasts: $\lambda = 1$ and $\lambda = 10$.

effective viscosity $[\eta]$ as a function of reduced shear rate $(C_\kappa)$ for several viscosity contrasts $\lambda$. The results are reported in Figure 3.14. We have seen before that for $\lambda = 1$, the suspension shows shear-thinning. The results in Figure 3.14 show that doubling the viscosity contrast, already shows the birth of a weak shear-thickening behavior, after a first interval of shear-thinning. Increasing progressively $\lambda$ favors more and more the shear-thickening behavior at the expense of the shear-thinning one. For high enough $\lambda$ the shear-thickening regime fully dominates.

As we have seen before there are two antagonist effects. The decrease of the Taylor deformation index and straightening of the vesicles which favor shear-thinning, and the increase of the TT angle which favors shear-thickening. For low enough $\lambda$, say $\lambda = 2$, one sees that a decrease of the Taylor deformation index $D$ with shear rate dominates over the increase of the TT angle (Figure 3.15), whereas at larger $\lambda$ (say $\lambda = 5$ and beyond) the opposite happens (Figure 3.15). This analysis shows that the prevalence of shear-thinning or shear-thickening is quite subtle and requires an investigation of the behavior of the suspended entities under a close scrutiny.

It can be generally expected that the effective viscosity of a suspension is affected by a multitude of factors, each acting in its own way. Since all of these factors vary on changes of the shear rate, it is impossible to isolate their effects independently. We can not therefore provide a robust criterion which discriminates between shear-thinning and shear-thickening. For example, it has been observed in [Beaucourt et al., 2004b] for 2D vesicles at low $C_\kappa$ and in [Kaoui et al., 2009b] for 3D vesicles, that the TT angle decreases with increasing $C_\kappa$ for fixed $\lambda$. The range of $C_\kappa$ explored in [Beaucourt et al.,

2004b] (a 2D study which is directly to be confronted to the present one) corresponds to the small capillary number regime ($C_\kappa = 0.075 - 0.75$). We have confirmed these results, which show an opposite behavior than the present results which focused on higher $C_\kappa$ ($C_\kappa = 1 - 200$). In other words, for a very small $C_\kappa$ the TT angle decreases when $C_\kappa$ is increased, while the opposite behavior is found here. This suggests that the full picture of vesicle dynamics and rheology is quite complex and that while the variations of the TT angle and of the Taylor deformation parameter can give useful insight into the rheological behavior of the suspension, there might be cases in which other factors play an important role.

Finally, it is interesting to note that the vesicle suspension can have a normalized effective viscosity $[\eta]$ which is significantly smaller than the Einstein one (for a dilute suspension of rigid disks, where $[\eta] = 2$). We have seen here that for $\lambda > 1$ we can achieve smaller viscosities as compared to the case with $\lambda = 1$. Indeed, in Figure 3.6 the minimal viscosity is of about 1.65, whereas for $\lambda = 1$ (Figure 3.1) it is equal to 2. As reported in [Thiébaud et al., 2014] (where only $\lambda = 1$ was treated), a minimal $[\eta]$ can be achieved at a special concentration. It is expected that if we scan different concentrations in the case of $\lambda = 10$, an even smaller value than 1.65 of $[\eta]$ can be achieved. Preliminary results show that indeed this minimal value can be significantly lowered. We hope to report along these lines, and more generally on the problem of monitoring a suspension that yields the smallest viscosity.

## 3.3 Conclusion

To sum up, we have presented numerical simulations of the rheological behavior of a confined suspension of vesicles under shear flow as a function of capillary number $C_\kappa$. Our simulations are based on the boundary integral method (2D). Special Green's functions are used in order to take into account the no-slip boundary condition at the bounding walls. The suspension of vesicles can either show shear-thinning behavior, which is related to the deformability of vesicles in flow, or shear-thickening behavior, which is related to the increase of TT angle of vesicles. We have also seen that the rheological system undergoes a gradual transition from a shear-thinning to a shear-thickening behavior upon increasing the viscosity contrast. Several blood diseases (such as sickle cell disease, malaria, etc..) are accompanied by an increase of the cytoplasm viscosity. It would be interesting to investigate the shear-dependent rheology in confined suspensions for various RBCs pathologies. Note that blood in

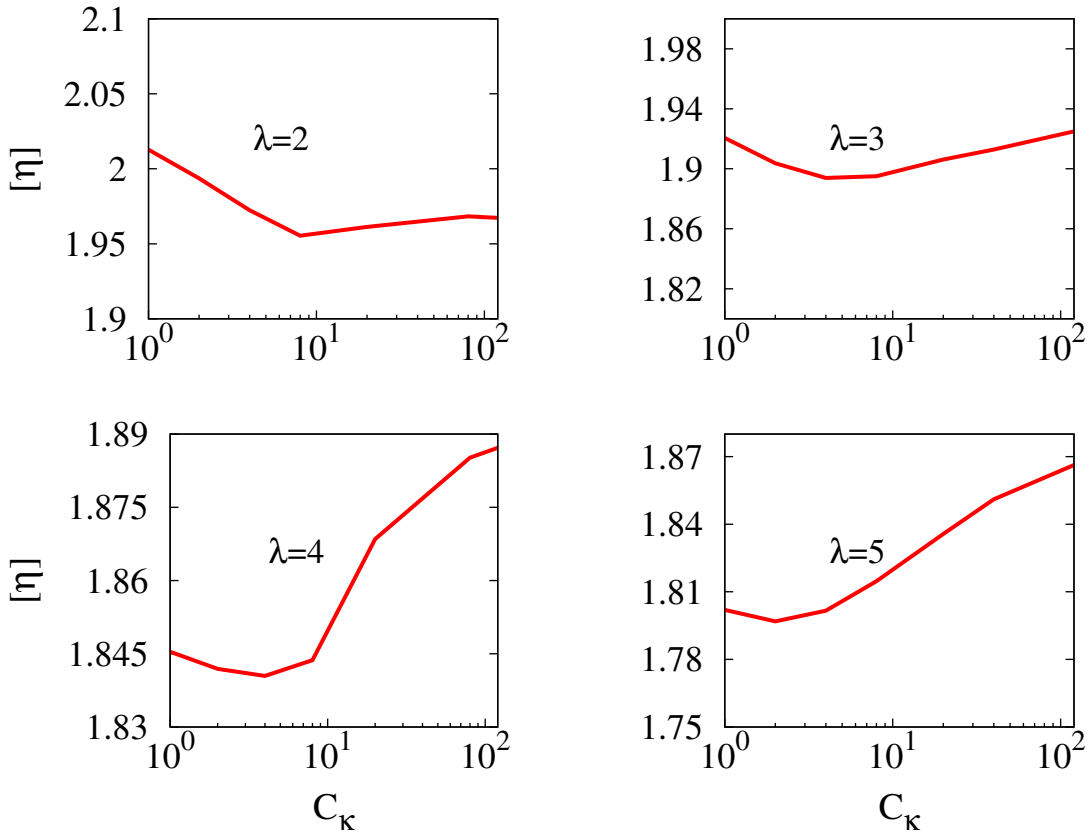


Figure 3.14: Shear-thinning to shear-thickening crossover for a suspension with concentration $\phi = 5.58\%$

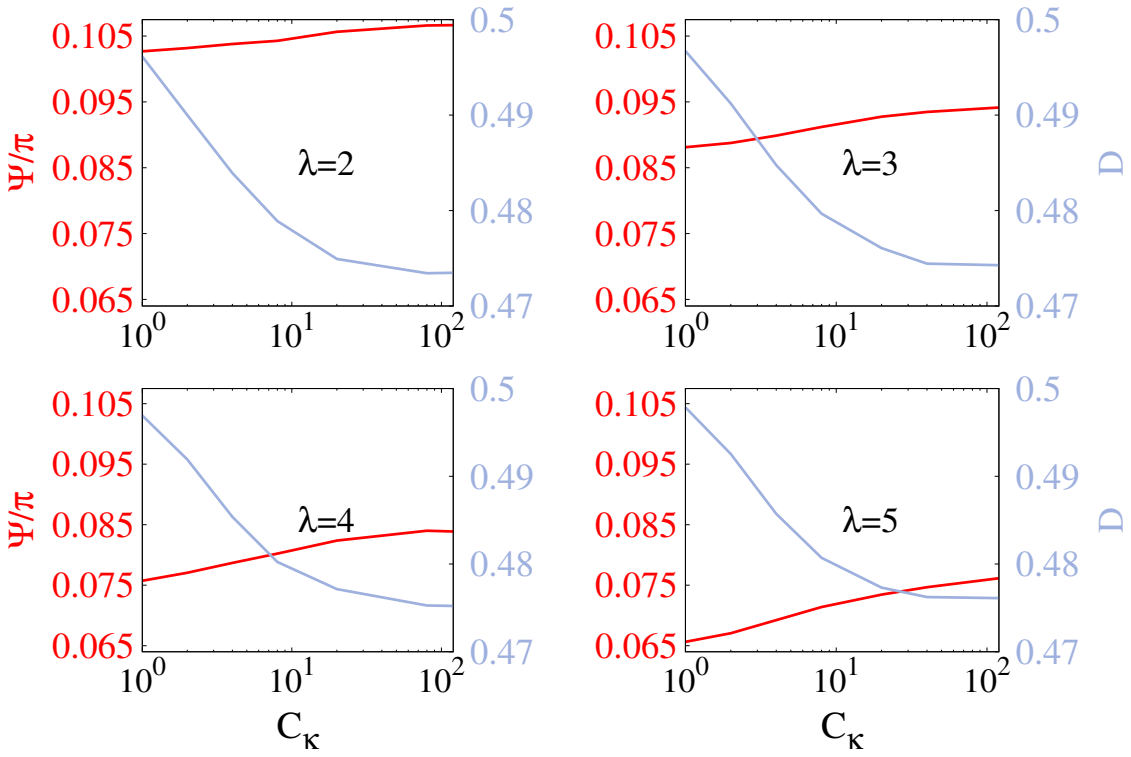


Figure 3.15: The evolution of the Taylor deformation index $D$ and the inclination angle $\Psi$ of the vesicle as a function of capillary number $C_\kappa$ for different values of the viscosity contrast $\lambda$.

unconfined geometry always shows a shear-thinning behavior, partly due to the dissociation of RBC rouleaux and partly due to the RBC deformation. The study of rheology reported here has shown that the situation is more complex with confined suspensions than with the unbounded case. This analysis introduces a new paradigm that opens a way for a refined analysis of confined rheology. Finally, we would like to draw the attention on the fact that the normalized effective viscosity undergoes here only moderate changes with shear rate (of about 10-15%), whereas the normalized normal stress difference can vary by a factor of up to two (see Figure 3.6). Here we have focused our study to the case of a 2D suspension. A preliminary study presented in [Thiébaud et al., 2014] has shown that the same type of order of the suspending entities takes place also in 3D. It is natural to expect a similar behavior regarding the shear-thinning and shear-thickening behavior as in 2D. In addition, the reduced volume of a RBC is lower than that analyzed here (the reduced volume for a RBC is about 0.6), and the deformation amplitudes, due to the dimensionality, may be significantly stronger than those reported here. This quantitative differences may trigger ampler manifestation of the rheological signatures. It is hoped to investigate this matter in the future.

# Chapter 4

# Does a vesicle migrate to the center or to the periphery in a bounded shear flow?

This chapter is concerned mostly with 2D simulations in order to investigate the lateral migration of a suspended vesicle in a bounded shear flow in the Stokes limit. The introduction and method are presented in Section 4.1 and Section 4.2 respectively. The emergence of novel off-centered stable positions beyond a critical viscosity contrast is discussed in Section 4.3. A systematic analysis is first performed in 2D (due to numerical efficiency). A collaboration with S. Gekle and his former PhD student A. Guckenberger (Bayreuth university, Germany) has confirmed the overall picture in 3D. We shall show the effects of the relevant parameters, namely: confinement, capillary number and reduced area as well as the initial conditions on the off-centered positions. Section 4.3 is devoted to the conclusion and perspectives.

## 4.1 Introduction

The problem of lateral migration (or cross-streamline migration) of small enough particles (where inertia can be neglected) is of considerable importance in many fields, such as in mechanics, physics, chemistry and biology [Larson, 1999, De Gennes and Gennes, 1979, Doi and Edwards, 1988, Fung, 2013]. A particular property of the inertialess limit (or the Stokes limit) is that a rigid particle, when it stays oriented in the shear plane, can not migrate perpendicularly to the flow direction in a linear shear flow. This is traced back to the invariance of the Stokes equations under time reversal. Soft particles, in contrast, can acquire a cross-streamline migration because their deformation can lead to an upstream-downstream asymmetry, breaking thus

the reversibility of the Stokes equations. A particularly studied example of interest to our study is the lift of a vesicle due to wall [Seifert, 1999, Sukumaran and Seifert, 2001, Olla, 2000, Cantat and Misbah, 1999, Olla, 1997a, Olla, 1997b, Olla, 1999, Coupier et al., 2008, Kaoui et al., 2008, Guckenberger et al., 2018, Abkarian and Viallat, 2008, Hariprasad and Secomb, 2015, Qi and Shaqfeh, 2017, Qi and Shaqfeh, 2018, Kaoui et al., 2009a, Beaucourt et al., 2004a]. This type of lift plays an important role in hemodynamics where RBCs have a tendency to accumulate towards the blood vessel center, leaving behind a cell-free layer close to the vessel wall. This effect is accompanied by an ample decrease of blood viscosity [Pries et al., 1992] upon decreasing the vessel diameter and is commonly known as the Fåhræus-Lindqvist effect [Fåhræus and Lindqvist, 1931].

When a vesicle is placed in a linear shear flow, i.e. between two parallel planes moving with equal and opposite velocities, it has been reported (in accordance to intuition) that the vesicle will feel symmetric lifts from both walls, so that the ultimate position is a centered one. When the vesicle settles in the center it undergoes a tank-treading motion (provided the viscosity contrast is small enough). For higher viscosity contrast the vesicle may undergo a tumbling dynamics, but the wall-induced lift still operates [Grandchamp et al., 2013, Shen et al., 2017] and pushes the vesicle (or red blood cell) towards the channel center. Indeed during tumbling, the particle is elongated along its longest axis during one part of the tumbling cycle and compressed during the other one due to the elongational component of the shear flow. This creates an asymmetry of the shape during the two halves of the tumbling period, leading to a net migration (albeit small compared to the case where the vesicle undergoes tank-treading).

In this chapter, by investigating systematically the question of a cross-streamline migration in a linear shear flow created by two counter-translating planes, we find that the problem can be more complicated than previously thought. Indeed, the centerline does not always correspond to the final position. Instead we find a complex phase diagram, where for low enough viscosity contrast the vesicle always reaches the center, for all sets of initial conditions that we have explored. However, beyond a critical viscosity contrast the vesicle can either reach the centerline or move towards one of the two walls and align with the flow. Whether the vesicle chooses one or the other solution depends on initial conditions.

## 4.2 Method and parameters

Here we recall the definition of some important parameters and their values used in this chapter. For both geometries (2D & 3D), in our simulations the viscosity contrast $\lambda = \eta_{in}/\eta_{out}$, where $\eta_{in}$, $\eta_{out}$ denote the inner and the outer fluids' viscosities is varied in a wide range $\lambda = 1-50$. The vesicle is subjected to a planar shear flow $v_x^0 = \dot{\gamma} y$ (or, in 3D $v_x^0 = \dot{\gamma} z$) with $v_x^0$ the component along the flow direction of the imposed flow $\mathbf{v}^0$. Its dynamics is formulated using a boundary integral method. Here the x-axis (x and y in 3D) is defined to be parallel to the walls. The vesicle membrane acts on the fluid via bending and tension forces, their expression are given by equation 2.2 for 2D and equation 2.4 for 3D vesicle model. The capillary number is defined as $C_\kappa = \eta_{out}\dot{\gamma} R_0^3/\kappa$, and it controls how the shapes of vesicles deform in response to an applied external flow. The confinement $C_n = 2R_0/W$, where $W$ is the channel width. The reduced area (for 2D) $\tau = 4\pi A/L^2$, where $L$ is the vesicle perimeter and the effective radius $R_0 = \sqrt{A/\pi}$. The reduced volume (for 3D) $\tau^{3D} = 6\sqrt{\pi}V/A'^{3/2}$ (with the vesicle volume $V$ and surface area $A'$) and an effective radius defined as $R_0 = (3V/(4\pi))^{1/3}$.

## 4.3 Results

We perform a systematic study for a single vesicle under confined shear flow. We shall show that beyond a critical viscosity contrast, there is coexistence of two stable branches of solutions (the centered and the off-centred one). According to the bifurcation theory nomenclature, there should exist a critical viscosity contrast at which the system undergoes a saddle-node bifurcation. Besides the analysis of the bifurcation, we shall also describe the basin of attraction of each solution (when they coexist), as well as the effect of other parameters (reduced area, and degree of confinement) on the overall solutions.

When the shear stress increases, it is found that the saddle-node bifurcation evolves into a pitchfork bifurcation. In that case, there is no coexistence, but rather the central position becomes unstable beyond a critical viscosity contrast in favor of an off-centered solution. The first and systematic study is dedicated to a 2D geometry. Due to computational efficiency, this will allow us to scan a quite large parameter space. At the end, we will devote a brief discussion to the same problem in 3D in order to highlight the robust nature of the problem.

### 4.3.1 Off-centered stable positions beyond a critical viscosity contrast

We first start by describing systematically the results for the 2D model. The 3D simulations show a qualitatively similar behavior, as shown in Subsection 4.3.6. Here we investigate the influence of the viscosity contrast $\lambda$ on the equilibrium lateral position of the vesicle. The lateral migration of a vesicle is described using the vesicle's center of mass. Initially the vesicle is located at a small enough distance ($0.72R_0$) from the lower wall and is then subjected to a shear flow. Figure 4.1 contains the first central result, showing the final position $h_f$ (distance from the center of the channel to the center of mass of the vesicle) as a function of $\lambda$. Here the other parameters are kept fixed: $\tau = 0.7$, $C_\kappa = 1$ and $W/R_0 = 5$. As shown in that figure, below a critical value of $\lambda$ ($\lambda_c \simeq 16$) the final position corresponds to the center of the channel; note that the centerline is at 0 on the vertical axis in (Figure 4.1a) and the lower wall is at $-0.5$. In this case (centered vesicle), the vesicle dynamics correspond to the classical behavior [Thiébaud and Misbah, 2013, Zhao and Shaqfeh, 2013, Ghigliotti et al., 2010, Rahimian et al., 2010, Vitkova et al., 2008, Danker et al., 2007, Boedec et al., 2017] : tank-treading motion (TT) when $\lambda$ is small enough ($\lambda \lesssim 10$) and tumbling regime (TB) for $\lambda \gtrsim 10$. In both cases the vesicle feels a wall-induced lift that pushes it towards the centerline. However, the vesicle in TT regime ($\lambda = 1$ Figure 4.2) reaches the centerline faster than in the case of TB motion ($\lambda = 11$). Figure 4.2a,b shows the behavior in the course of time in the case where the vesicle undergoes TT and TB, respectively.

An interesting feature is discovered for higher values of $\lambda$. Indeed, for $\lambda \gtrsim \lambda_c$, the vesicle, initially located close to the wall, lifts off slightly and never reaches the centerline. Instead, it tends with time to a final off-centered position (see Figure 4.2c,d). In addition, the vesicle, despite high values (up to 50) of the viscosity contrast never showed TB, and rather exhibits a flow alignment (FA), where the vesicle is off-centered and almost aligned with the flow (vesicle's long axis is parallel to the flow direction) while the membrane performs TT with a lower tank-treading velocity ($V_{tt}$) than that of the TT and TB motions (Figure 4.1b).

Note that above the critical value of viscosity contrast $\lambda_c$ but close to it, the vesicle reaches its final off-centered position in a non monotonous way with time, by undergoing quite ample oscillations (Figure 4.2c). Note finally, that when $\lambda > \lambda_c$ the vesicle always reaches an off-centered position. We will see later that the situation is more complex, since the final position is sensitive to initial position (see section 4.3.3).

In the following section we investigate the effect of the channel width on the dynamics of the vesicle and we shall provide some intuitive mechanisms controlling the equilibrium lateral position of the vesicle within the channel.

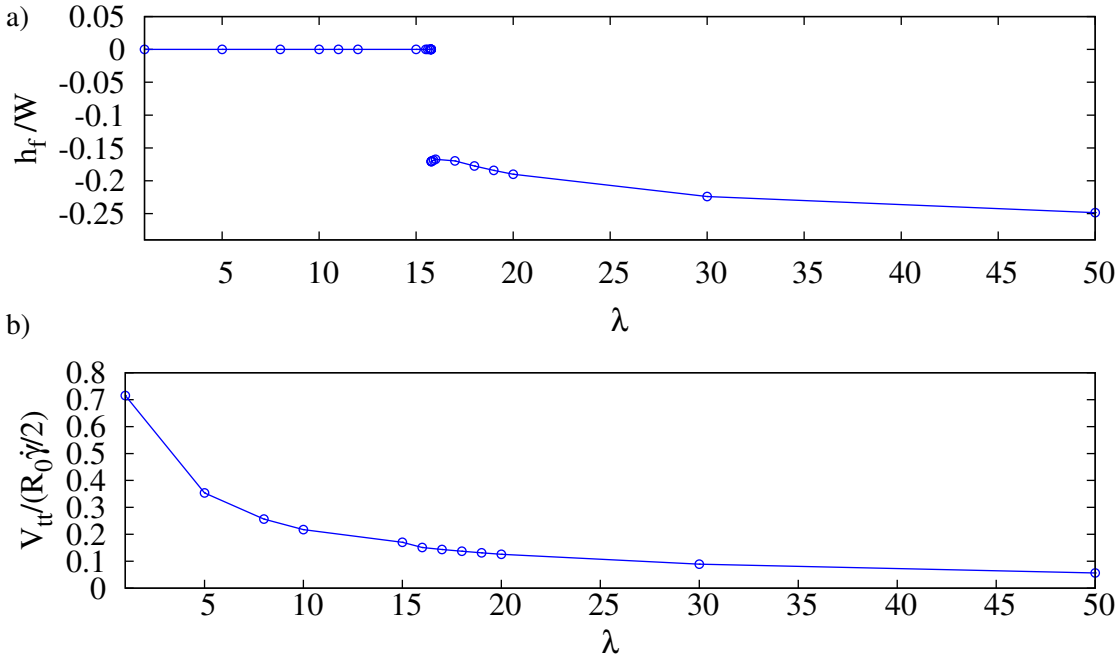


Figure 4.1: The evolution of the equilibrium lateral position $h_f$ and the dimensionless tank treading velocity $V_{tt}/(R_0\dot{\gamma}/2)$ (a and b *resp.*) according to the bifurcation parameter $\lambda$. Here $\tau = 0.7$, $C_\kappa = 1$ and $W/R_0 = 5$. $R_0\dot{\gamma}/2$ is the velocity of membrane of a circular vesicle under shear flow in unbounded geometry.

### 4.3.2 Effect of channel width and qualitative physical arguments for the emergence of the off-centered solution

We have analyzed the role played by the confinement (see Figure 4.3) by considering an initial position close enough to the lower wall. The three main regimes attained by a vesicle in shear flow for $W/R_0 = 5$, namely TT, TB and FA (see previous section) persist for all explored values of confinement. Each value of $W$ (Figure 4.3) is associated with a critical viscosity contrast $\lambda_c(W)$, below which the particle always migrates away from the wall to the centerline of the channel, whereas beyond $\lambda_c(W)$ an off-centred position with FA is attained by the vesicle.

A high confinement favors the centered solution, as can be seen in Figure 4.3 and 4.4. This result is quite intuitive. In short, the main effect of the confinement is to shift the transition threshold value $\lambda_c$ to higher values upon increasing the degree of confinement.

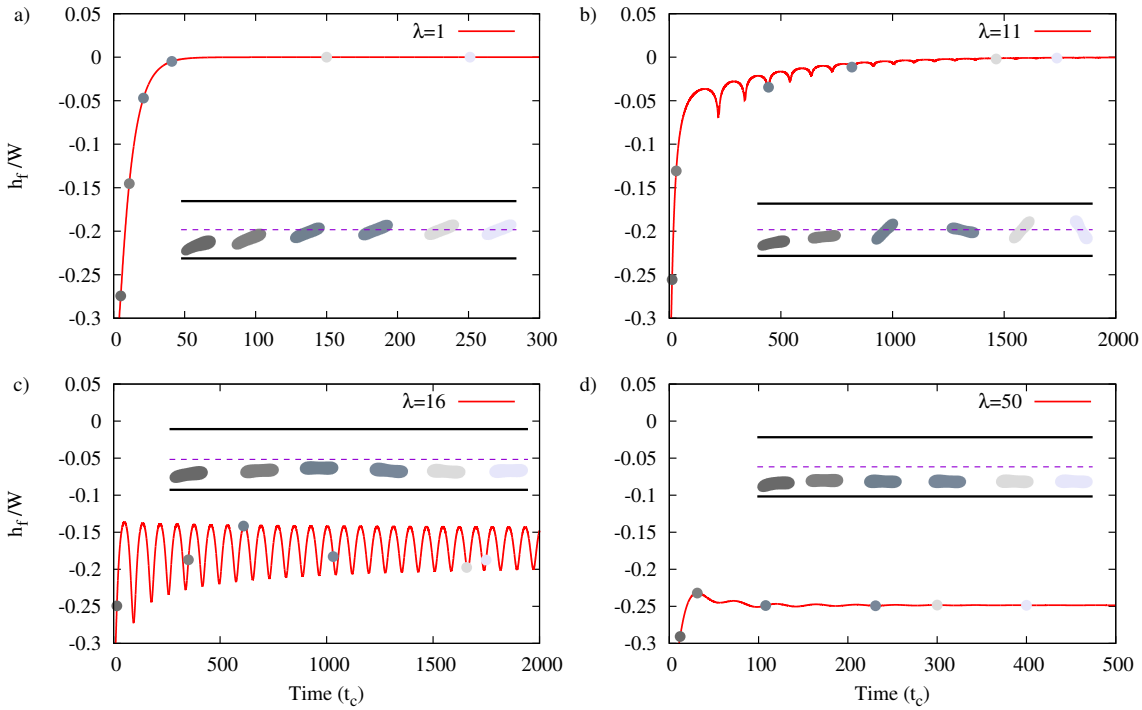


Figure 4.2: The evolution of the lateral position of the vesicle $h_f$ as a function of time (in units of $t_c$) for several $\lambda$. The center is at 0 on the vertical axis and the lower wall is at $-0.5$. In this case, below $\lambda_c = 16$, the vesicle is centered. For very low $\lambda$ (TT motion), it reaches the center of the channel faster while for larger lambda, but still below $\lambda_c$ TB motion is observed and the time to reach the center becomes significantly longer. Beyond $\lambda_c$ the vesicle is off-centered. A typical sequence of snapshots are shown. Here we set $C_\kappa = 1$, $\tau = 0.7$ and $W/R_0 = 5$. We note that in c) ($\lambda = 16$), the final value of $h_f$ is computed as a time average over more than $4000t_c$.

Let us now propose some mechanisms controlling the stable lateral position. Our results (Figure 4.3) show that below $\lambda_c$ the vesicle can either perform a TT motion or a TB motion. In the pure TT regime the wall-induced lift is so strong that the vesicle continues to migrate until it reaches the center where the effects of the two walls compensate each other. Upon increasing $\lambda$ the vesicle undergoes a TB transition. A linear shear flow can be viewed as a superposition of a rotational and an elongational flow (see Figure 4.5a). If $\lambda$ is not too large the TB vesicle still shows some deformation, and during one half of the TB cycle, the vesicle is oriented with its long axis having positive angle with the horizontal axis, in which case it is elongated by the shear flow, and will lift off with a certain amplitude. During the second half of the TB cycle the vesicle long axis is oriented along negative angles, and it is compressed by the shear flow. Thus its migration speed is lower than in the first half of the cycle. Thus, globally the vesicle will lift off, albeit less than in the TT regime, and finally reaches the center.

In the vicinity of $\lambda_c$, the vesicle still has a small tendency to lift-off (Figure 4.5b) due to a small upstream/downstream asymmetry, and may acquire a slightly positive angle (Figure 4.5c) [Olla, 1997b, Cantat and Misbah, 1999, Sukumaran and Seifert, 2001]. Since the viscosity contrast is large enough, the vesicle, once it has started lifting, will be subject to TB, which has an antagonist effect, causing the lift-off angle to decrease, and even to reverse it (TB is clockwise; Figure 4.5d). The vesicle will then have an anti-lift pushing it back towards the wall. Once close to the wall, the vesicle aligns with the wall. At the wall (Figure 4.5e) due to an overpressure ahead and underpressure at the rear [Olla, 1997b, Cantat and Misbah, 1999, Sukumaran and Seifert, 2001] the lubrication forces causing lift become again strong enough to lift-off the vesicle, which again faces the antagonist effect of TB, and so on. The interplay of these two antagonist effects leads to an oscillation of the vesicle position (as seen in Figure 4.2). When $\lambda$ is increased further and further the TB effect always wins and acts to stick the vesicle close to the wall and force it to align with the wall, leading to a permanent flow alignment.

In short, from figure 4.6, we see that the migration away from the walls is associated with a positive orientation angle, whereas the opposite happens for a negative tilt angle. Ultimately the vesicle settles at a certain $y$-position where it is almost aligned with the flow direction ($\Psi \simeq 0$).

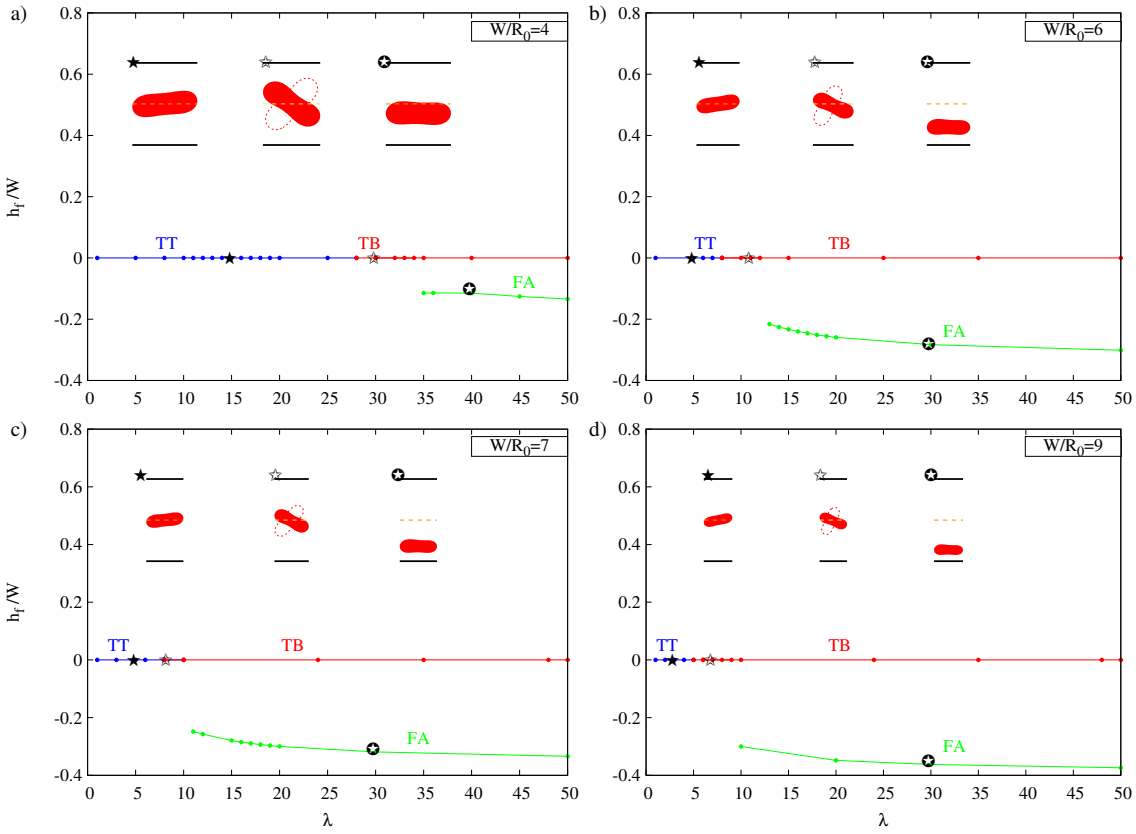


Figure 4.3: The evolution of the equilibrium lateral position $h_f$ as a function of the bifurcation parameter $\lambda$ for several channel width $W$. Here we set $C_\kappa = 1$ and $\tau = 0.7$ and the initial position of the vesicle is close enough to the lower wall. Beyond $\lambda_c$ the vesicle is initially set either at the center or at a small enough distance $(0.72R_0)$ from the lower wall. TT, TB and FA are shown.

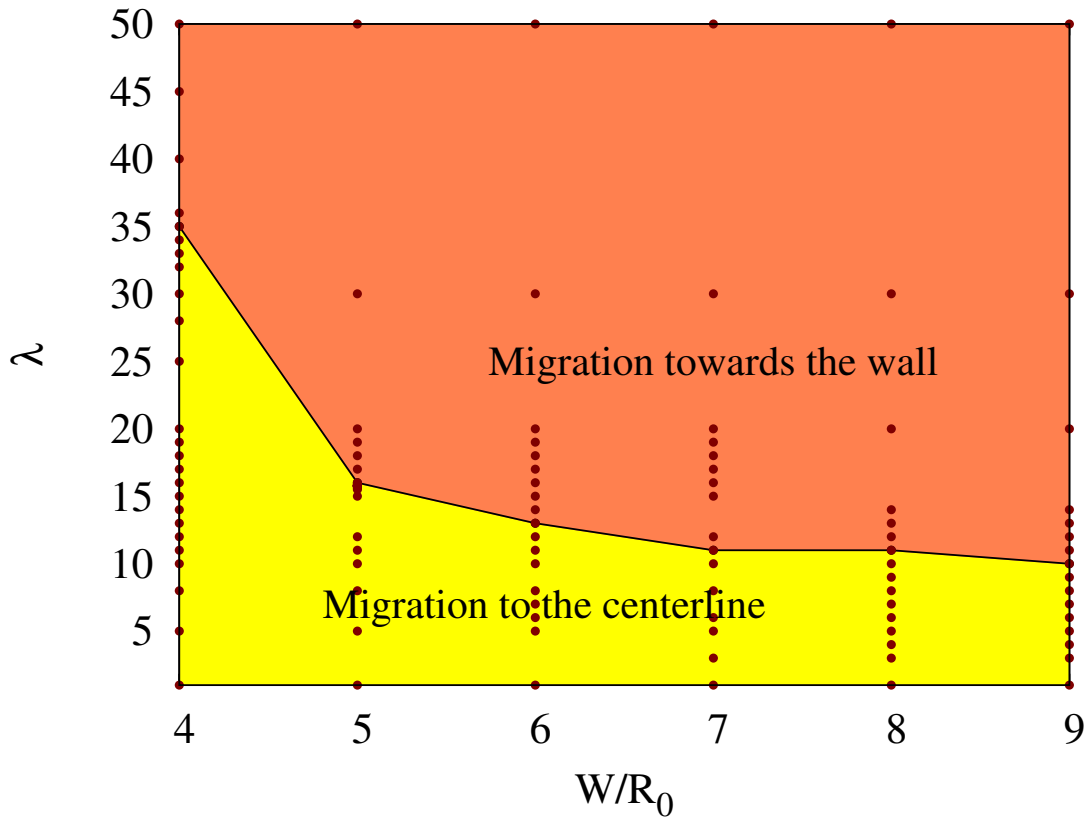


Figure 4.4: Phase diagram showing regions where migration is towards the center or towards the wall depending on $\lambda$ and $W$. Migration towards the centreline is favored by confinement (small $W$). The solid line is a guide for the eyes. The simulations data are shown as dots. Here we set $\tau = 0.7$ and $C_\kappa = 1$.

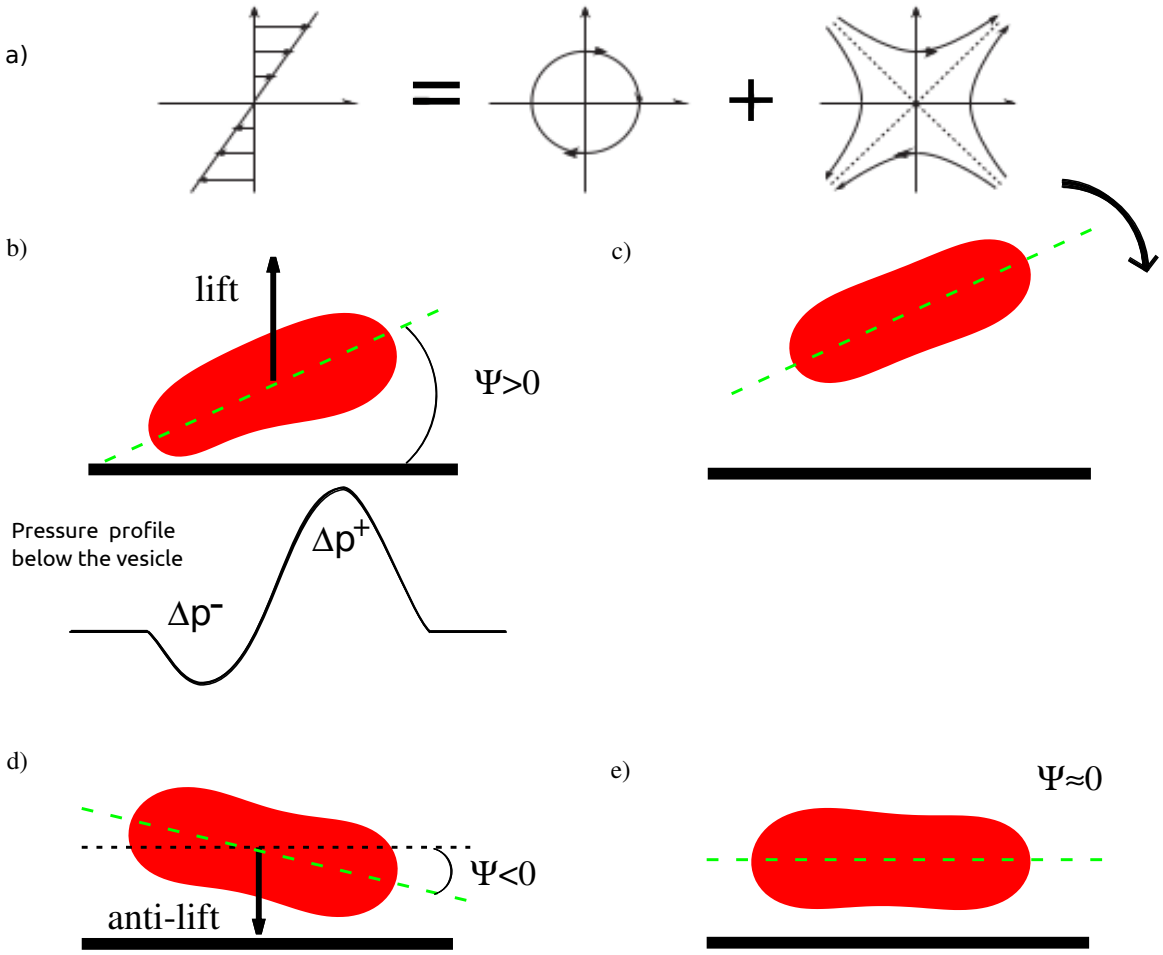


Figure 4.5: a): Decomposition of the linear shear flow into pure rotational and elongational components. b, c, d, and e): Schema showing the link between the orientation angle of the vesicle with the direction of the flow (horizontal axis) and the lift of the vesicle. We show here the pressure profile given in [Cantat and Misbah, 1999] as an illustration.

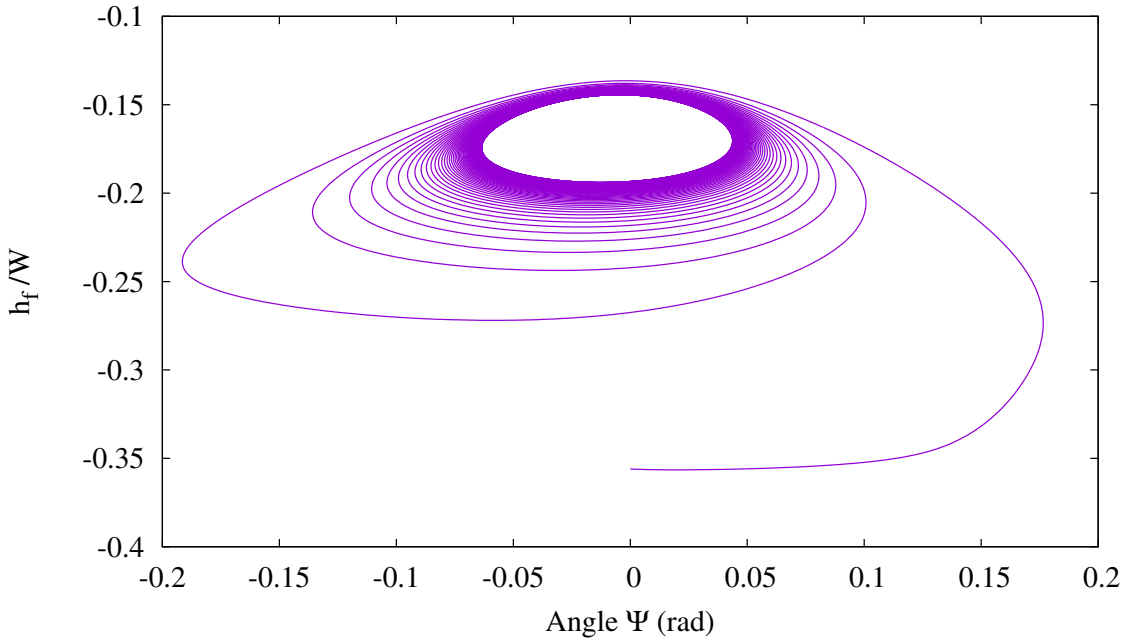


Figure 4.6: Angle $\Psi$ *vs* lateral position of the vesicle $h_f$. Here $\lambda = 16$, $C_\kappa = 1$ and $W = 5R_0$.

### 4.3.3 Effect of the initial position

We will now dig further into the existence of different branches of solutions. For that purpose, we investigate how the initial position of the vesicle affects its final stable position by performing a systematic study varying the initial position of the vesicle within a channel for different values of $\lambda$. We set $W = 5R_0$, $C_\kappa = 1$ and $\tau = 0.7$.

In Figure 4.7 we find that the initial position does not affect the final position of the vesicle if $\lambda \lesssim \lambda_c$. For all initial positions explored in the simulations, the vesicle is found to migrate towards the centerline independent of the initial position. In other words, the basin of attraction of this solution seems to be the whole channel width. The situation is different for $\lambda \gtrsim \lambda_c$. The vesicle can either migrate towards the wall or towards the centerline of the channel. It migrates towards the wall if its initial position is within the orange area (the basin of attraction) and towards the centerline if its initial position is within the yellow area (the basin of attraction of this solution) in Figure 4.7. The blue curve in Figure 4.7 corresponds to the final stable position of the vesicle if its initial position is within the orange area. Even when the initial position of the vesicle is above the solid blue curve but within the orange area (between the solid and dashed blue line), the vesicle is attracted towards the blue solid line, which is thus a stable branch.

In order to check the stability of this branch, we introduce a small perturbation of the equilibrium lateral position of the vesicle for a specific value of $\lambda$ as shown in Figure 4.8. After few characteristic times, the center of mass of the vesicle comes back to its equilibrium position, meaning (linear) stability of the solution. If we set initially the vesicle in the vicinity of the dashed blue curve, but in the yellow region, the vesicle migrates towards the centerline for each value of $\lambda$. Thus the solid blue line is a stable branch whereas the dashed blue line is unstable. The two stable lines (solid blue and solid green lines) are thus separated by the unstable (blue dashed line) branch. This is a typical situation of coexistence of solutions. The solid blue line is a node (in the language of dynamical systems) and the dashed line is a saddle. Thus, in principle the solid and dashed blue lines should intersect on the left side in Figure 4.7 (around $\lambda \sim 16$ with a vertical tangent), corresponding to a saddle-node bifurcation point [Misbah, 2017]. However, it was not easy to detect this point with a good enough precision, as there is a discontinuous jump close to the saddle-node point. We have seen that the final position of the vesicle is affected by its initial position if $\lambda \geq \lambda_c$.

Besides varying the initial position, we also run simulations for vesicles with the same position but different orientations. We observe that indeed the initial orientation of the vesicle can also affect its final position. I.e. whether the vesicle chooses one of the two steady branches depends on orientation.

### 4.3.4 Effect of capillary number

In this section we investigate the effect of capillary number $C_\kappa$ (this parameter controls the deformability of the vesicle under flow). Capillary numbers $C_\kappa \gg 1$ imply large flow rates and thus in general large deformation. The other parameters are kept fixed: $W = 5R_0$, $\tau = 0.7$ and we set the vesicle initially close enough to the lower wall. Here our aim is not to study sensitivity to initial conditions, but rather to analyze the evolution of the new off-centered solution. This is why the initial position is set close to the wall. The explored capillary number range is 0.5–10. Figure 4.9 illustrates the effect of $C_\kappa$ on the equilibrium lateral position of the vesicle within the channel. The main difference with previous results is that upon increasing $C_\kappa$ the line representing the final position as a function of $\lambda$ exhibits less and less stronger jumps at the bifurcation point. Our results show even that above a certain value of $C_\kappa$ ($C_\kappa \geq 2.5$), the equilibrium lateral position of the vesicle $h_f$ does not undergo any discontinuity as a function of $\lambda$. In other words, we have an evolution from a saddle-node bifurcation into a pitchfork one. To further support this conclusion,

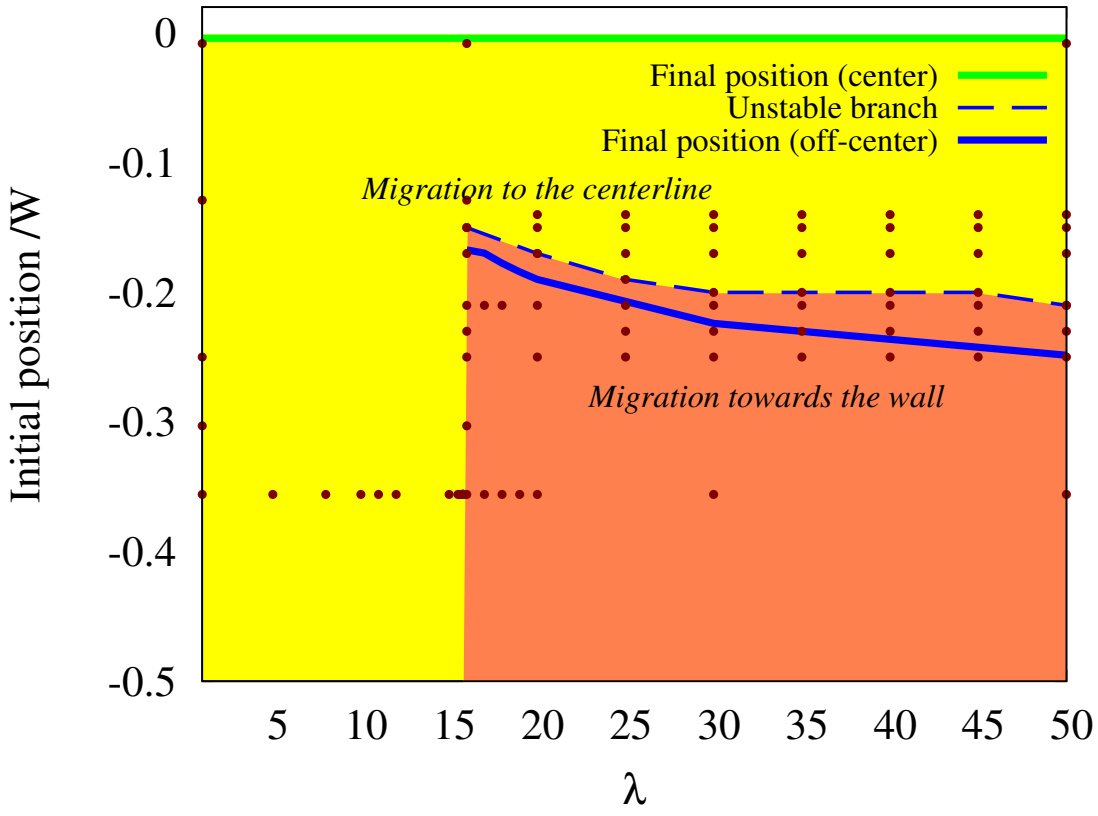


Figure 4.7: Phase diagram showing regions where migration is towards the center (if initial position is within yellow area) or towards the wall (if initial position is within orange area). The saddle-node bifurcation occurs at $\lambda_c \simeq 16$ for a reduced area $\tau = 0.7$, a capillary number $C_\kappa = 1$ and a channel width $W = 5R_0$. The channel center is at zero and the wall is at $-0.5$ on the vertical axis. The simulations data are shown as dots.

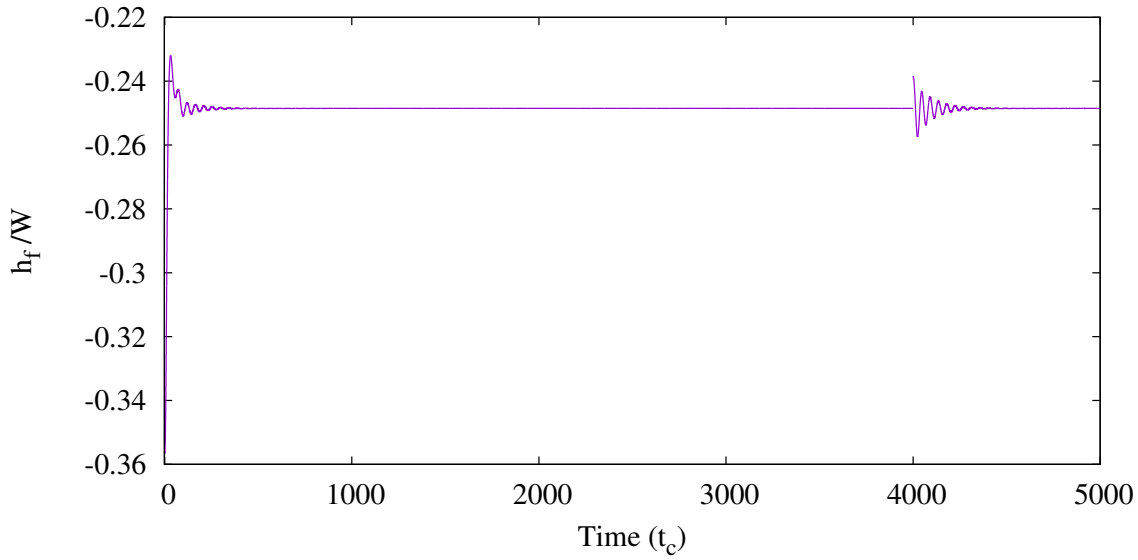


Figure 4.8: Lateral position of the vesicle $h_f$ *vs* time before and after a small destabilisation. From this figure we see clearly that the final solution (i.e. final position) is stable. Here $\lambda = 50$, $C_\kappa = 1$, $W = 5R_0$ and $\tau = 0.7$.

we have run simulations for $\lambda > \lambda_c$ by setting the vesicle in the centerline. After some time, due to numerical noise, the vesicle left the center towards an off-centered final position, meaning that (unlike the case where $C_\kappa$ is small) the central position is linearly unstable. It is interesting to note that the change of the nature of the bifurcation (from saddle-node to pitchfork) seems to coincide with the disappearance of the TB motion. More precisely, upon increasing the viscosity contrast $\lambda$ the vesicle shows TT motion with central position, and at a critical $\lambda$, its equilibrium position gradually moves from the center towards the wall (by still performing TT). When $\lambda$ is far enough from the critical value, the vesicle shows a flow alignment. Note that the absence of TB by increasing $\lambda$ is favored by the presence of the bounding walls. It is known in an unbounded linear shear flow in 3D that if the vesicle is in the TB regime, then an increase of $C_\kappa$ suppresses TB in favor of vacillating-breathing, or even flow alignment [Biben et al., 2011, Farutin et al., 2010, Kaoui et al., 2009b, Danker et al., 2007, Lebedev et al., 2007]. The phase diagram in Figure 4.10 shows the regions where the vesicle migrates towards the center and those where it migrates towards the wall (by having an initial position close to the wall). The widening of the basin of attraction of the central position beyond $C_\kappa \simeq 2.5$ is attributed to the ample increase of deformability that favors the wall induced migration.

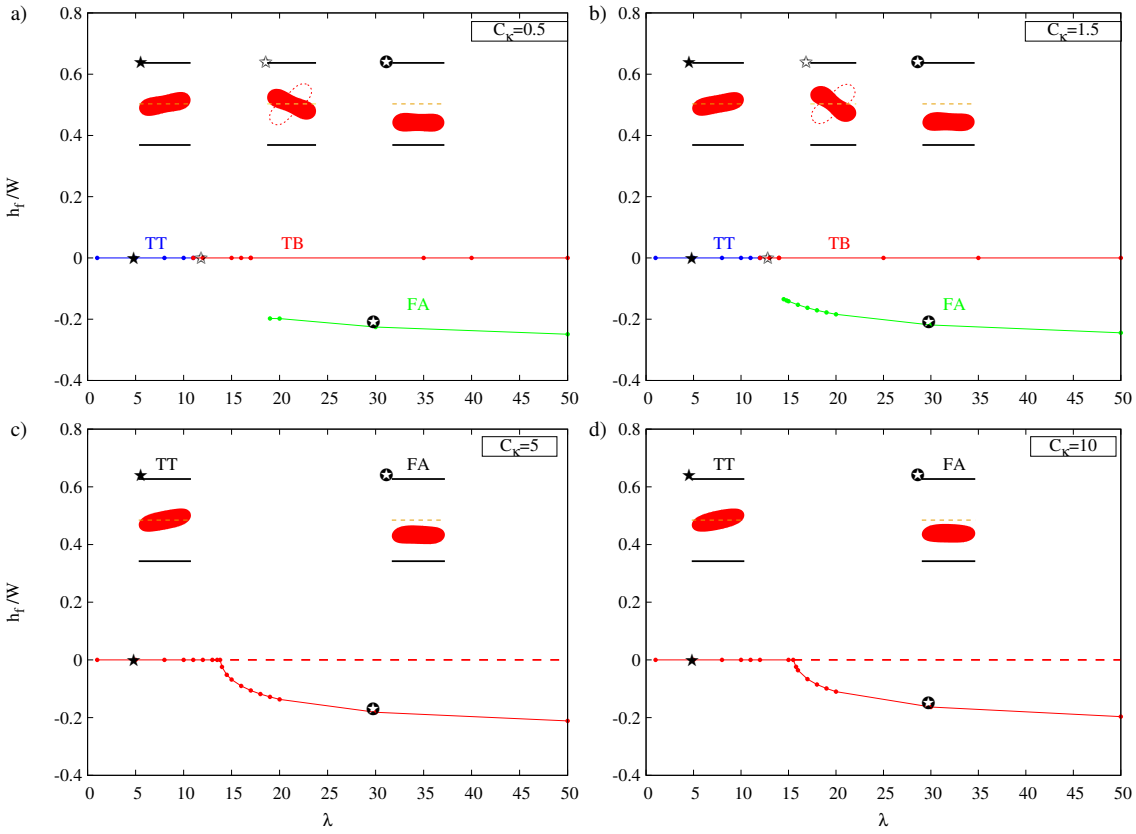


Figure 4.9: The evolution of the equilibrium lateral position $h_f$ according the bifurcation parameter $\lambda$ for several capillary numbers $C_\kappa$. The initial position of the vesicle is close enough to the lower wall. Beyond $\lambda_c$ the vesicle is initially set at the centerline or at a small enough distance $(0.72R_0)$ from the lower wall. TT, TB and FA are shown. Beyond a certain value of $C_\kappa$, the TB motion is suppressed.

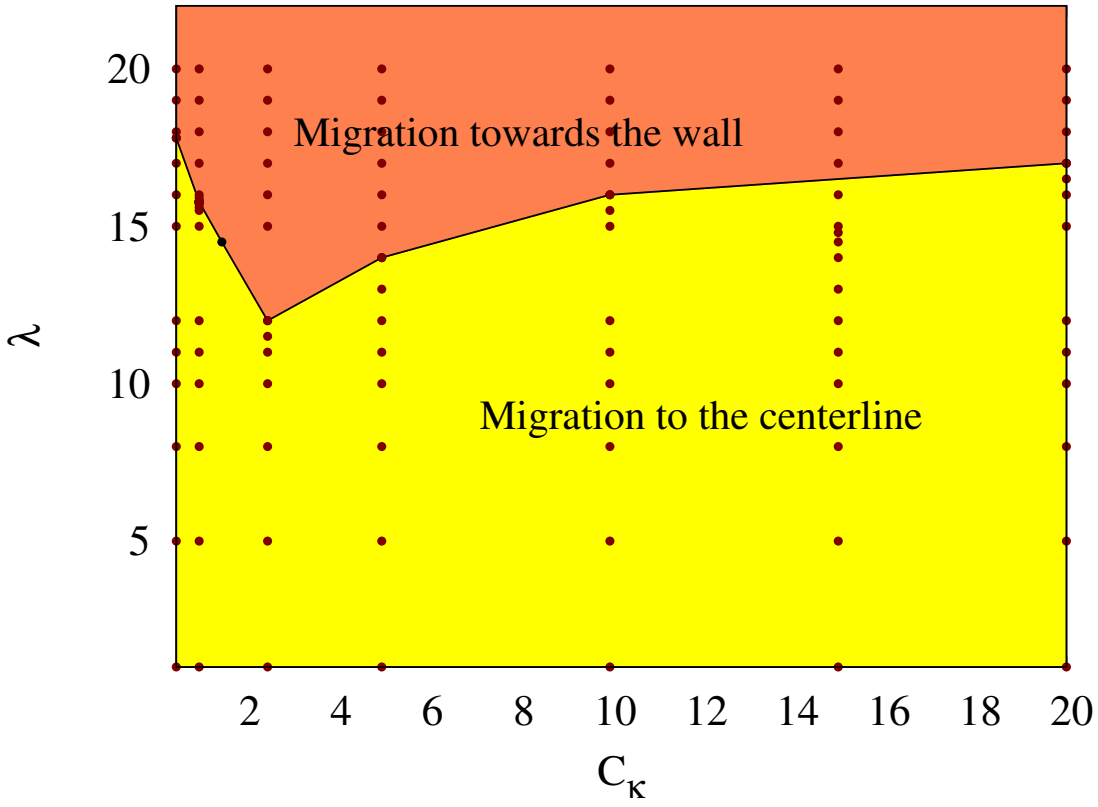


Figure 4.10: Phase diagram showing regions where migration is towards the center or towards the wall depending on $\lambda$ and $C_\kappa$. We see here that the capillary number ($C_\kappa$) has a non-monotonic effect on the lateral position of the vesicle, see the text for explanation. The solid line is a guide for the eyes. The simulations are shown as dots. Here we set $\tau = 0.7$ and $W = 5R_0$. Initially the vesicle is close enough to the one of the walls.

### 4.3.5 Effect of reduced area

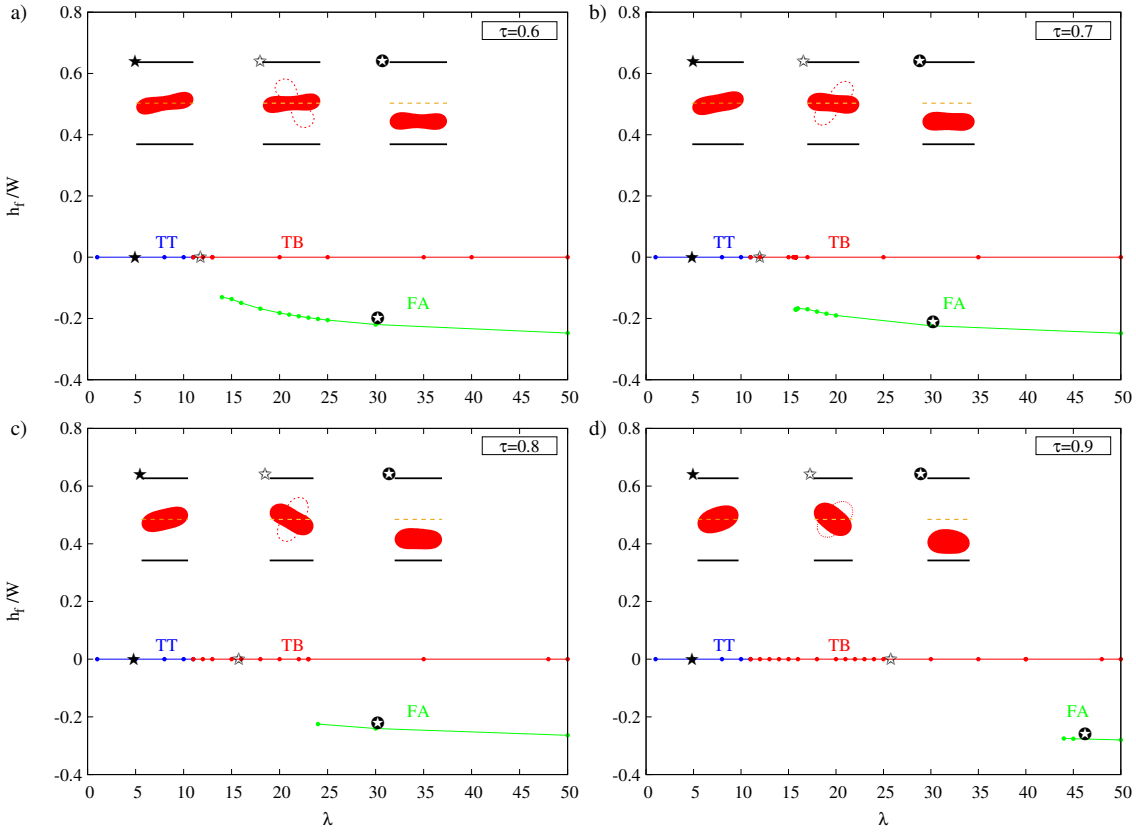


Figure 4.11: The evolution of the equilibrium lateral position $h_f$ according the bifurcation parameter $\lambda$ for several reduced area $\tau$. Here we set $C_\kappa = 1$ and $W = 5R_0$. Initially the vesicle is close enough to one of the walls. Beyond $\lambda_c$ the vesicle is initially set at the centerline or at a small enough distance ($0.72R_0$) from the lower wall. TT, TB and FA are shown.

Finally, let us give a brief report on the influence of the reduced area $\tau$ (for a circle $\tau = 1$, otherwise $\tau < 1$). The results are shown in Figure 4.11. The other parameters are fixed as follows: $W = 5R_0$ and $C_\kappa = 1$. The vesicle is set initially at a small distance from the lower wall. The range of viscosity contrast over which the TB motion survives (with, as before, migration towards the center) becomes wider with $\tau$. This means that the transition towards FA is delayed. This is shown by the widening of the yellow region in Figure 4.12. When $\tau$ increases the vesicle becomes more and more rounded (i.e less elongated) so that the TB strength becomes weaker to force the vesicle to align with the wall in the vicinity of the wall. The vesicle migration towards the center wins over the antagonist TB effect (see Figure 4.5 which explain competition between TB and lift-off).

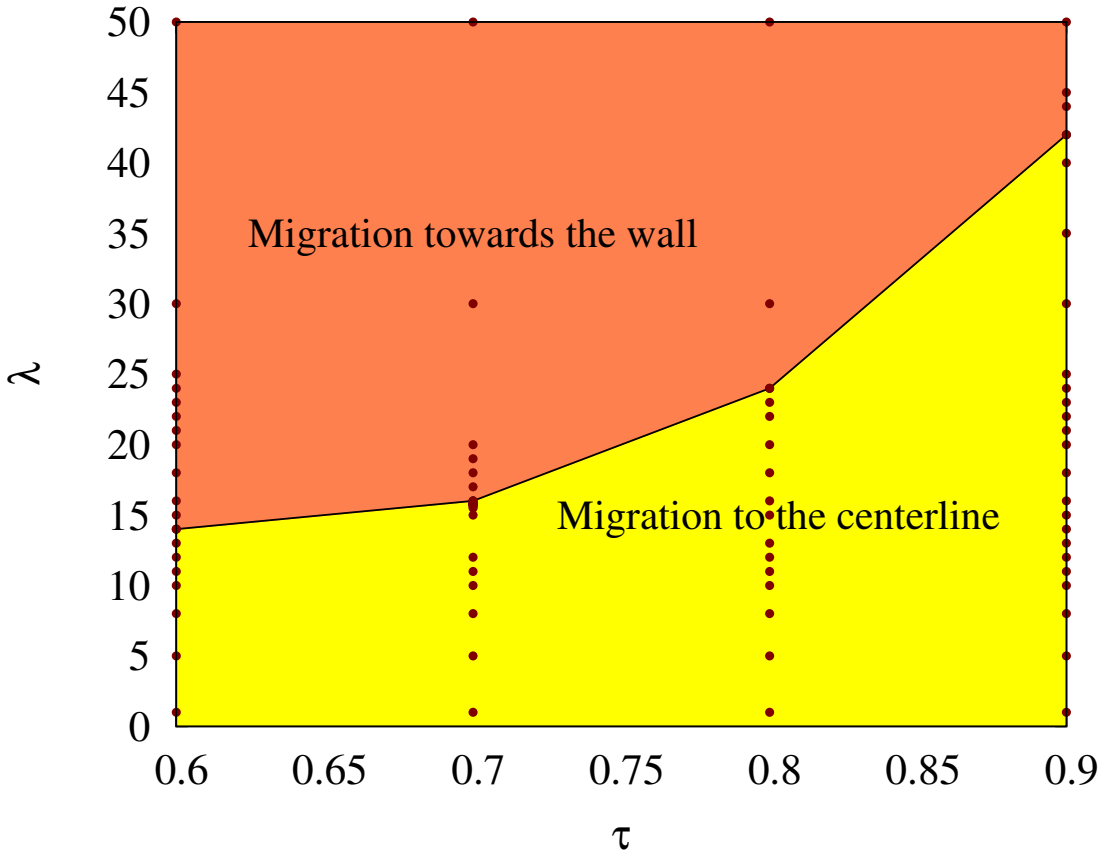


Figure 4.12: Phase diagram showing regions where migration is towards the center or towards the wall depending on $\lambda_c$ and reduced area $\tau$. Migration towards the centerline is favored with increasing $\tau$. The solid line is a guide for the eyes. The simulations data are shown as dots. Here we set $W = 5R_0$ and $C_\kappa = 1$.

### 4.3.6 3D Results

The question naturally arises whether the above 2D results are a consequence of dimensionality or whether they point to a more general phenomenon. To indicate that the observed phenomena are not an artefact of the 2D model, we here devote a brief discussion to the 3D case thus validating the key results of the 2D studies. The details of the numerical procedure can be found in [Guckenberger and Gekle, 2018] and in the Chapter 2. We have set the reduced volume $\tau^{3D} = 0.7$, the channel width $W = 5R_0$ and the capillary number $C_\kappa = 1$. For each value of $\lambda$, we start with the vesicle at different initial $z$-positions: In the center ($z_0 = 0$) and off-centered at $z_0/R_0 = \pm 1.2$, except for $\lambda > 40$, where we use $z_0/R_0 = \pm 1$ for stability reasons. We then consider the average $z$-position in the steady state which we denote as $\mathrm{h_f}$ as in the 2D case. The result can be seen in figure 4.13. For small values of $\lambda$, the vesicle always moves towards the center ($\mathrm{h_f} \approx 0$), in a good qualitative agreement with the previous 2D results. However, above a critical threshold of $\lambda \approx 25$, the vesicle assumes an off-centered position near the walls ($\mathrm{h_f} \neq 0$). The slight asymmetry for the two off-center starting positions at $\lambda = 25$ is a numerical artefact, stemming from the fact that we need to solve a Fredholm equation of the mixed-kind. In most cases, the vesicle tumbles. Exceptions are found only at $\lambda = 5$, where the vesicle assumes a tank-treading dumbbell shape when started off-centered, and at $\lambda \geqslant 40$, where the vesicle exhibits a rolling motion when started in the center. The latter also explains why the $z_0 = 0$ branch in figure 4.13 is distinct for $\lambda \geqslant 40$.

In short, we confirm in 3D that the vesicle under linear shear flow migrates towards the center for lower values of $\lambda$ and towards the wall for values of $\lambda$ above a critical value. These results are qualitatively consistent with the 2D results. Note that the presence of a third dimension can allow the vesicle to undergo different kinds of out-of plane motion which may make the phase diagram quite complex.

## 4.4 Conclusion

In this chapter, the dynamical behavior of a single vesicle in a confined shear flow as a function of viscosity contrast $\lambda$ has been investigated numerically. We have performed a systematic study in 2D on the effect of the relevant parameters: capillary number ($C_\kappa$), channel width ($W$) and reduced area ($\tau$) on the equilibrium lateral position of the vesicle. We have seen that below a critical viscosity contrast $\lambda_c$, the ultimate position of the vesicle is at the centerline, whereas above $\lambda_c$, the vesicle can be either

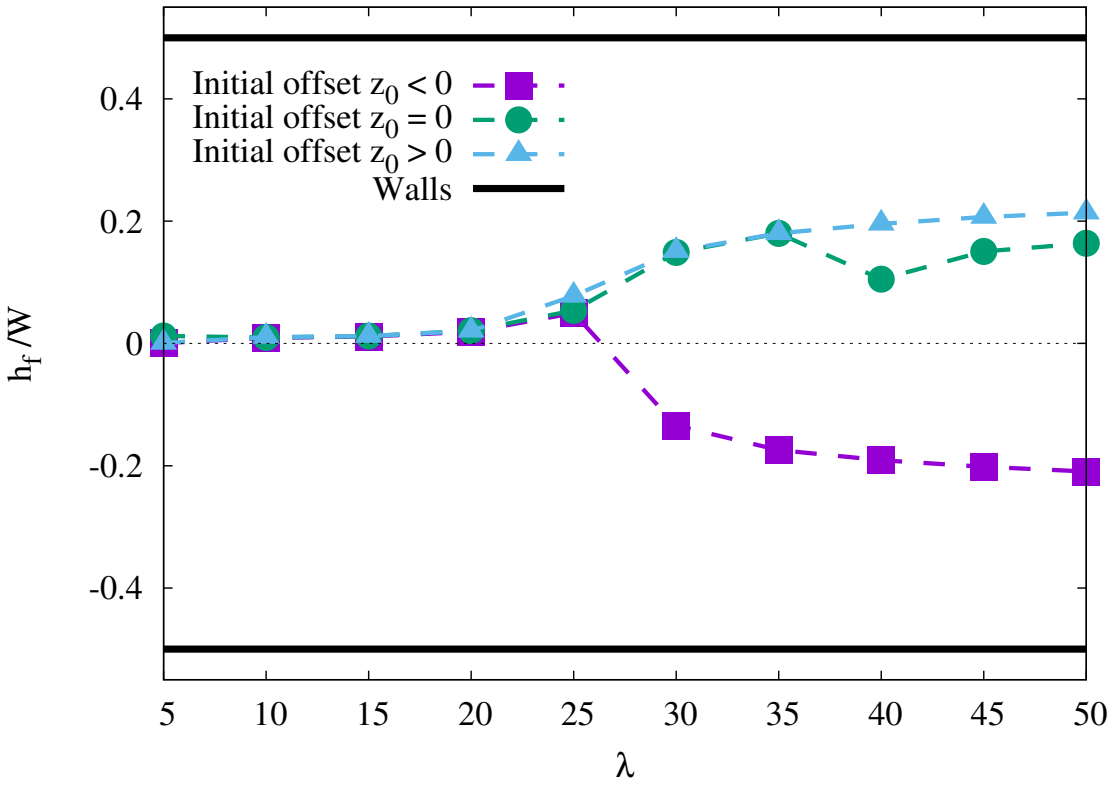


Figure 4.13: Average steady-state $z$-position $\mathrm{h_f}$ for a 3D vesicle as a function of the viscosity ratio $\lambda$. Three different initial positions are used: In the center ($z_0 = 0$) and near the walls ($z_0 \lessgtr 0$) . Here we set $W = 5R_0$, $\tau^{3D} = 0.7$ and $C_\kappa = 1$.

centered or off-centered depending on initial conditions. Finally, we carried out three-dimensional numerical simulation to confirm the overall picture obtained in 2D.

The revelation here of the existence of different kinds of solutions may lead to different suspension structuring when the concentration is increased. This structuring is expected to impact the rheological properties of the suspension. This constitutes the subject of Chapter 5. Finally, the dependence of solutions on the viscosity contrast as well as on the capillary number offers a versatile potential to manipulate and sort deformable particle depending on their internal viscosity and their compliance.

# Chapter 5

# Global rheology of a confined vesicle suspension

In this chapter, we present the effect of the novel off-centered position seen in Chapter 4 on the rheology of a vesicle suspension. An introduction is presented in Section 5.1. Sections 5.2 and 5.3 are devoted to the main results. We shall discuss the effect of the novel off-centered solution on the rheology of dilute and non-dilute suspension. A conclusion is given in Section 5.4.

## 5.1 Introduction

The rheology of blood flow depends upon the dynamics and spatial organization of the components. We pay a particular attention to the link between the structure of vesicles (used as a simple model of RBCs) under confined shear flow and the rheology of the suspension. In the previous chapter we have seen an important salient feature of a vesicle in a confined shear flow. We found that the ultimate lateral position of the vesicle may be at the centreline or at an off-centered position depending on the initial conditions. Here we numerically investigate the relationship between the lateral position of a vesicle and the rheology of the suspension under shear flow using a boundary integral method. The rheological properties of such suspensions are not yet fully understood. Among the dynamics of the vesicle under flow, the equilibrium lateral position has a strong impact on rheology of the suspension.

Understanding the rheology of a vesicle suspension has many applications, among them the rheology of blood in microcirculation is a classic example of a non-Newtonian fluid. For example, in blood vessels within the human body, red blood cells undergoing lateral migration concentrate in the center of the blood vessel due to their

deformability, leading to changes in blood viscosity, where this phenomenon takes the name of Fåhræus-Lindqvist effect [Fåhræus and Lindqvist, 1931].

Many studies have addressed the question of lateral migration of a vesicle under flow [Seifert, 1999, Sukumaran and Seifert, 2001, Olla, 2000, Cantat and Misbah, 1999, Olla, 1997a, Olla, 1997b, Olla, 1999, Coupier et al., 2008, Kaoui et al., 2008]. Migration away from the walls is generally associated with a positive orientation angle (angle between long axis of the vesicle and flow direction) [Olla, 1997b, Olla, 1997a, Olla, 1999, Nait-Ouhra et al., 2018]. Further heuristic explanations on the mechanisms of the lateral migration of the vesicle under a confined shear flow could be found in the previous chapter. Many other studies have addressed the rheology of a suspension of vesicles [Lamura and Gompper, 2013, Thiébaud and Misbah, 2013, Kaoui et al., 2014, Thiébaud et al., 2014].

Based on the results of the previous chapter, where we have found that the final position of the vesicle depends on initial conditions and viscosity contrast $\lambda$, we provide here a link between the final equilibrium lateral position of the vesicle and the rheology of the suspension for a wide range of viscosity contrast $\lambda$.

## 5.2 Results

We have performed a systematic study for a single vesicle under shear flow by varying the relevant parameters (confinement, capillary number and reduced area). We shall also consider both the dilute, semi dilute and more concentrated regimes up to about 35% of vesicle area fraction for which we have taken typical values of the parameters. We shall show that the initial conditions of the vesicles significantly alter the final spatial organization. As a consequence, the rheology is affected by the spatial organization (which depends an initial condition) up to a certain concentration. Beyond this concentration, the initial condition is irrelevant.

### 5.2.1 Rheology and its relation to attractors of vesicle positions in the channel

In this section we investigate the influence of the final equilibrium position ($h_f$) of a single vesicle on the rheology of the suspension by varying the viscosity contrast $\lambda$. We recall the first rheological quantity of interest: the normalized effective viscosity

$[\eta]$ (equation 2.51):

$$[\eta] \equiv \frac{\eta_{\text{eff}} - \eta_{\text{out}}}{\eta_{\text{out}}\phi} = \frac{1}{nA\eta_{\text{out}}\dot{\gamma}} \left( \int_{\text{mem}} \mathrm{d}s\, y f_{\text{flu}\to\text{mem},x} + \eta_{\text{out}}(\lambda - 1) \int_{\text{mem}} \mathrm{d}s\, (n_x v_y + n_y v_x) \right) \tag{5.1}$$

This expression is the extension of the Batchelor result for suspensions of rigid particles to vesicles [Batchelor, 1970]. Initially the vesicle is at a small distance ($0.72R_0$) from the lower wall and then shear flow is applied. Figure 5.1 displays the central result of this chapter. Here the relevant parameters are kept fixed as follows: $\tau = 0.7$, $C_\kappa = 1$ and $W/R_0 = 5$. As shown in Figure5.1, (our aim here is only the rheology

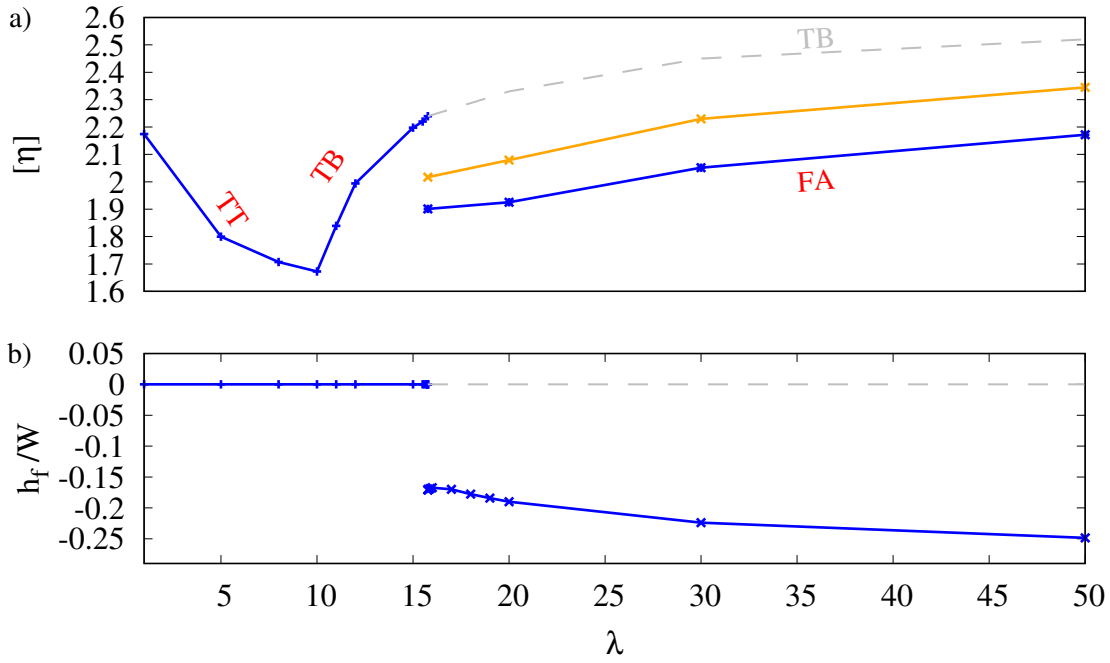


Figure 5.1: The evolution of the normalized viscosity $[\eta]$ and equilibrium lateral position $h_f$ (a and b *resp.*) as a function of the bifurcation parameter $\lambda$. TT: Tank-treading, TB: Tumbling, FA: Flow alignment. Here $\tau = 0.7$, $C_\kappa = 1$ and $C_n = 0.4$. The dashed gray lines correspond to the results where the vesicle initially started at the centerline or at its vicinity and ultimately gets centered. The orange line is the ensemble average of the viscosity (see text). The centerline is at $y/W = 0$ on the vertical axis in (Figure 5.1b) and the lower wall is at $y/W = -1/2$.

while the equilibrium lateral position has been studied in Chapter 4 and published in [Nait-Ouhra et al., 2018]), below a critical value of lambda ($\lambda_c \simeq 16$, a value which depends on the other parameters) the vesicle migrates towards the center of the channel. In this case (centered vesicle), the suspension shows a classical behavior [Danker and Misbah, 2007b, Thiébaud and Misbah, 2013, Zhao and Shaqfeh, 2013, Ghigliotti

et al., 2010, Rahimian et al., 2010, Vitkova et al., 2008, Danker et al., 2007] : in the tank-treading motion (TT) $[\eta]$ decreases with $\lambda$ until a minimal value. Then $[\eta]$ increases in the tumbling regime (TB) (Figure 5.1a). Above $\lambda_c$, if the initial position is close enough to the wall (the distance from the lower wall in the simulation is $0.72R_0$), the vesicle settles in an off-center position [Nait-Ouhra et al., 2018] as shown in Figure 5.1b. This solution coexists with the centered solution. The vesicle aligns with the flow and we have referred to this solution as flow alignment (FA), whereas in the coexisting centered regime the vesicle shows TB. The two corresponding branches are labeled FA and TB in Figure 5.1a. In other words, the suspension presents two possible values of viscosity due to the existence of two different attractors. The orange branch in Figure 5.1 shows the ensemble average of $[\eta]$ obtained from the following expression: $[\eta] = P_{FA}[\eta]_{FA} + P_{TB}[\eta]_{TB}$, where $P_{FA}$ ($P_{TB}$) is the probability that the final configuration is FA (TB) and $[\eta]_{FA}$ ($[\eta]_{TB}$) is the normalized viscosity corresponding to the FA (TB) regime. The probability is calculated, for a given $\lambda$, as the interval of initial conditions leading to a given solution (bassin of attraction was calculated in Ref. [Nait-Ouhra et al., 2018], Figure 7) divided by the whole interval of initial conditions. Whether the system selects one solution or the other depends on initial conditions. The viscosity in the FA regime is significantly smaller than that in the TB regime. This is quite intuitive since a TB vesicle has a larger cross section in the channel than a FA vesicle, opposing thus higher resistance to the flow. When $\lambda$ increases further the viscosity of the FA solution shows an increase of the suspension viscosity. This is due to the fact that the FA vesicle is closer and closer to the wall, and thus the cell free layer becomes smaller and smaller.

### 5.2.2 Effect of degree of confinement

In this section we investigate the effect of the degree of confinement on the dynamics and rheology of a very dilute suspension of vesicles. We take a single vesicle initially placed close to the lower wall. We set $\tau = 0.7$, $C_\kappa = 1$ and vary $\lambda$ (key parameter in this study) for several $C_n$. The results are depicted in Figure 5.2 which shows the same qualitative behavior as seen in the previous section. The same dynamics of the vesicle for $C_n = 0.4$ (previous section) persists for all values of confinement investigated here, that is, TT, TB and FA motion are observed. For each value of $C_n$ (Figure 5.2) there is a different critical viscosity contrast $\lambda_c$, below which the vesicle migrates to the centerline and $[\eta]$ shows a non-monotonic behavior as already discussed in the previous section. Beyond $\lambda_c$ the vesicle settles at an off-center position, exhibiting a sudden decrease of the normalized viscosity $[\eta]$ of the suspension (Figure 5.2), which

then increases with increasing $\lambda$. In conclusion, the same trend is observed pointing to the robustness of the phenomenon.

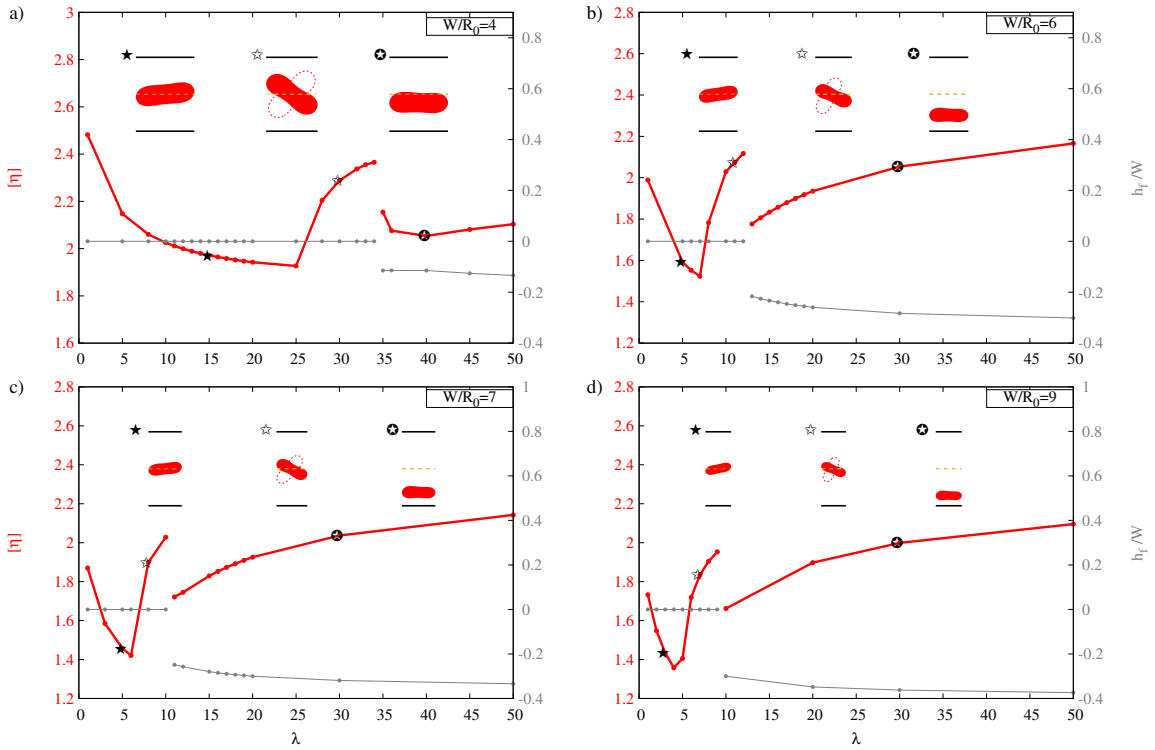


Figure 5.2: The evolution of $[\eta]$ and equilibrium lateral position $h_f$ as a function of $\lambda$ for several degrees of confinement $C_n$. Here we set $C_\kappa = 1$ and $\tau = 0.7$. The vesicle is initially set at a small enough distance ($0.72R_0$) from the lower wall. TT, TB and FA are shown. The channel center is at zero and the walls are at $y/W = \pm 1/2$ on the right vertical axis. Note that the TB branch continues for larger $\lambda$ but here we only show the results until the FA branches appears.

### 5.2.3 Effect of capillary number

In this section we consider the effect of capillary number $C_\kappa$ on the dynamics and rheology of the vesicle by fixing the other parameters, $C_n = 0.4$, $\tau = 0.7$. Figure 5.3 illustrates the effect of $C_\kappa$ on the dynamics and rheology. The main difference with previous results is that upon increasing $C_\kappa$ the gray line representing the off-centered position as a function of $\lambda$ exhibits weaker and weaker jumps at the bifurcation point, until the transition becomes continuous. The saddle-node bifurcation transforms into a pitchfork bifurcation. This transition also affects the behavior of the normalized viscosity $[\eta]$ which shows weaker jumps until showing a continuous behavior. A point worth of mention is that the TB regime completely disappears in favor of a continuous

transition from a TT solution to a FA one. We also note that for a given $\lambda$ in the off-centered case (FA regime in Figure 5.3), the distance between the vesicle and the wall increases as a function of capillary number $C_\kappa$ implying a decrease of the normalized viscosity with $C_\kappa$ (shear-thinning behavior).

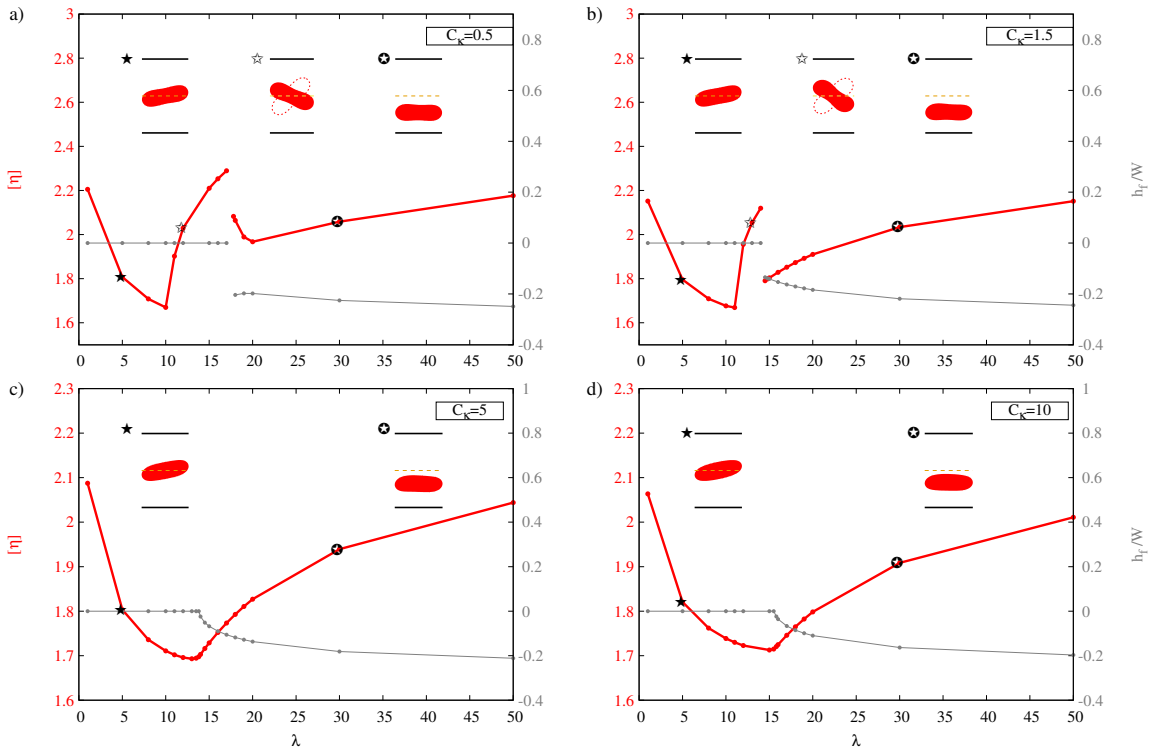


Figure 5.3: The evolution of $[\eta]$ and equilibrium lateral position $h_f$ according the bifurcation parameter $\lambda$ for several capillary numbers $C_\kappa$. The vesicle is initially set at a small enough distance ($0.72R_0$) from the lower wall. TT, TB and FA are shown. Beyond a certain value of $C_\kappa$ (c and d panels) , the TB motion is suppressed and the evolution of $[\eta]$ as a function of $\lambda$ does no longer exhibit any jump. The channel center is at zero and the walls are at $y/W = \pm 1/2$ on the right $y$ vertical axis. Note that the TB branch (when it exists) continues for larger $\lambda$ but here we only show the results until the FA branches appears. For the continuous curves (i.e. when there is no jump), the TB regime does not exist.

### 5.2.4 Effect of reduced area

We carried out a systematic study on the effect of reduced area $\tau$ (for a circle $\tau = 1$, otherwise $\tau < 1$) on the equilbrium lateral position of a vesicle and its effect on the rheology of the suspension. The results are reported in Figure5.4. The other parameters are fixed to $C_n = 0.4$ and $C_\kappa = 1$. When $\tau$ is small enough, we find the same trends as before. However, as $\tau$ increases (approaching 1), the situation changes

significantly. For example, for $\tau = 0.9$ while the vesicle migrates out of center (for $\lambda > 40$), the normalized viscosity still exhibits a jump. Contrary to the other values of $\tau$, the viscosity is higher for the off-centered solution at the transition point. This is due to two effects: (i) the higher value of $\tau$ lowers the lift due to wall so that the fluid left between the vesicle and the wall is smaller, leading to higher dissipation. (ii) The vesicle has a shape close to a circle causing a higher cross-section against the flow. These two effects together yield higher viscosity than a tumbling vesicle at the center. Even if the vesicle tumbles at the center, due to its quasi-circular shape, its elongation is weaker now causing less and less resistance against the flow.

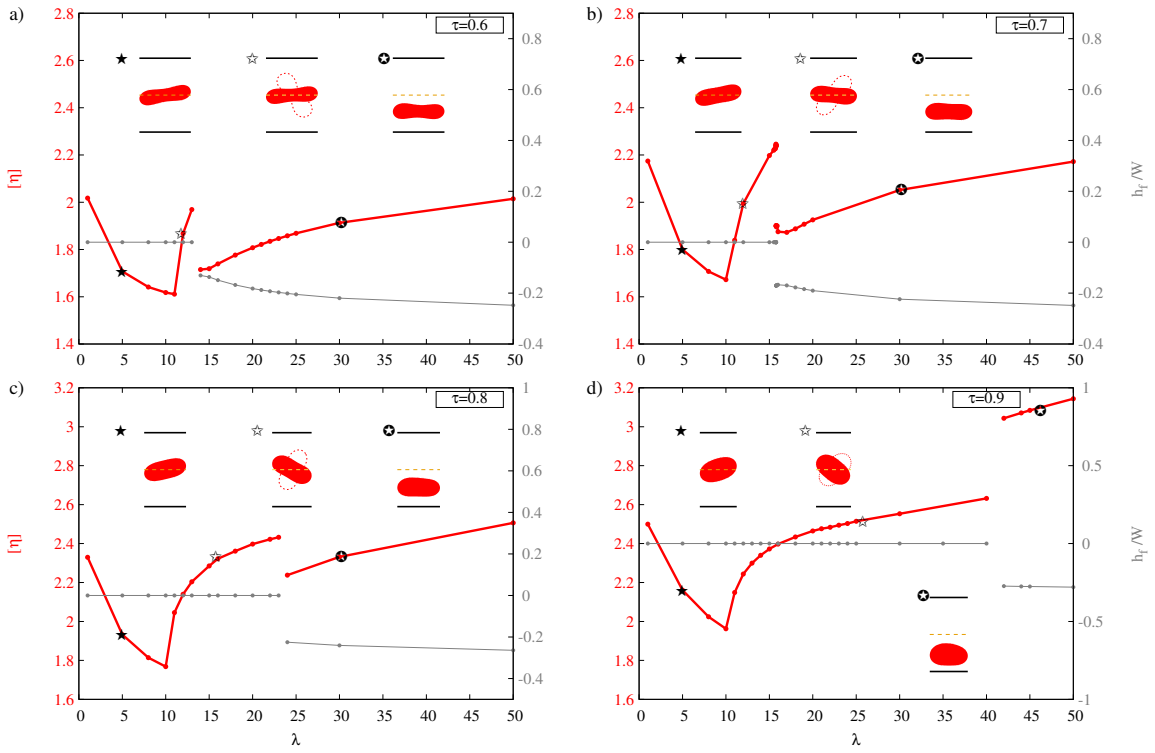


Figure 5.4: The evolution of $[\eta]$ and equilibrium lateral position $h_f$ as a function of the bifurcation parameter $\lambda$ for several reduced areas $\tau$. Here we set $C_\kappa = 1$ and $C_n = 0.4$. The vesicle is initially set at a small enough distance ($0.72R_0$) from the lower wall. TT, TB and FA are shown. The channel center is at zero and the walls are at $y/W = \pm 1/2$ on the right $y$ vertical axis. The normalized viscosity $[\eta]$ shows in the FA regime a jump with higher values than those of the TB regime for $\tau = 0.9$. This contrasts with the behavior for other value of $\tau$, see text. Note that the TB branch continues for larger $\lambda$ but here we only show the results until the FA branches appears.

## 5.3 Suspensions

We have seen above that depending on $\lambda$ a single vesicle may migrate to the center or towards the wall and this significantly alters the rheology of the suspension. The question naturally arises of whether this off-centered position may survive for higher concentrations. We have investigated this question by varying concentration and by choosing various initial vesicle positions with the aim to see whether or not the final configuration is sensitive to initial conditions. Periodic boundary conditions are used along $x$, and the box length is $L_x = 40.5R_0$ and the enclosed area of a single vesicle is $A = \pi R_0^2$. The other parameters are kept to $\lambda = 20$, $C_n = 0.4$ and $C_\kappa = 1$ for which a single vesicle would select an off-centered position. We first discuss the dilute and the semi-dilute regimes. We compare the results to those obtained in Ref. [Thiébaud et al., 2014] for another set of parameters ($\lambda = 1$, $C_n = 0.4$ and $C_\kappa = 1$) where only the centered solution exists; i.e. for this viscosity contrast $\lambda = 1$, there exists no second attractor (off-centered) for a single vesicle.

The results are presented in Figure5.5. We see that for $\lambda = 20$, and below a certain concentration ($\varphi \simeq 12.4\%$), the normalized viscosity $[\eta]$ may have several values for the same concentration ($\varphi$) depending on the final configuration (which depends on the initial configuration) of the suspension. This means that for dilute and semi-dilute suspensions, several stable spatial configurations are possible which give rise to different values of normalized viscosity $[\eta]$ or effective viscosity $\eta_{eff}$ (Figure5.6). It is interesting to note that, below a certain concentration ($\varphi \simeq 6.2\%$), the suspension of relatively rigid vesicles ($\lambda = 20$) may have a much lower value of $[\eta]$ than that of a suspension of soft vesicles ($\lambda = 1$ Figure5.5). This lower value for more rigid particles is associated with the existence of stable off-centered positions, as described above. The highly non-monotonic behavior of $[\eta]$ for $\lambda = 1$, described in [Thiébaud et al., 2014], as a function of $\varphi$ is due to the existence of ordered solutions with a single (for low enough $\varphi$) and double (for larger $\varphi$) file configurations.

For a large enough $\lambda$ for which two attractors exist for a single vesicle, the situation is quite different. We have fixed $\lambda = 20$. We find, depending on initial conditions (as described in the caption of Figure5.5) that for a small enough $\varphi$ ($< 6.2\%$) there exist two solutions (i) centered single file (as found for $\lambda = 1$) undergoing tumbling giving rise to the viscosity values shown as points ($a'$, $b'$ and $c'$) in Figure5.5 and (ii) off-centered single file solution exhibiting flow alignment having the viscosity shown as points ($a$, $b$ and $c$) in Figure5.5. In other words, for low enough $\varphi$ the single ordered file seems to exists whatever the value of $\lambda$ is. For $\lambda = 20$ the existence of FA single

file exists only for a low enough concentration (points $a$, $b$ and $c$ in Figure5.5). In this low concentration regime the normalized viscosity shows a plateau owing to the weak hydrodynamic interaction.

However, when the concentration increases slightly beyond point $c$ in Figure5.5 the hydrodynamic interaction among vesicles starts to play a role, but still the existence of two attractors continues to affect rheology up to about $\varphi = 12\%$. The situation becomes more complex than for a lower concentration. Indeed, the single file FA solution undergoes a transition towards the centered TB file (point $d$ and inset $d$ in Figure5.5). From point $c$ (FA file) to point $d$ (TB centered solution, see inset $d$) the viscosity increases as expected, since TB vesicles in the centerline have a higher cross section. When the concentration is increased further (from point $d$ to $e$) the single file TB solution still exists, but $[\eta]$ decreases. The reason is that the insertion of a new vesicles fills the gap between already existing vesicles and reduces the strength of recirculation zones between vesicles. This reasoning is similar to that evoked for $\lambda = 1$ (single file TT solution) [Thiébaud et al., 2014]. For solutions $d$ and $e$ the initial condition corresponds to a centered set of solution. It seems thus that the central attractor is robust despite the presence of hydrodynamic interaction. This is, however, not the case for the the second (off-centered) attractor. We have prepared half of vesicles with the off-centered position (at the attractor position for a single vesicle) and the other half at the opposite position (which is also an attractor as well) with the hope of obtaining a double file solution (as with $\lambda = 1$ [Thiébaud et al., 2014]). All simulations with these initial conditions led to a disordered final solution (represented by inset $f$ in Figure5.5). The same outcome is obtained with random initial position. It seems thus that the second attractor has become unstable in the presence of hydrodynamic interactions.

A further increase of $\varphi$ (for $\lambda = 20$) beyond point $e$, destroys the single file TB solution in favor of an apparently disordered solution (see inset $f$), leading to higher and higher viscosity. This is drastically different from the case of $\lambda = 1$, where the system organizes into a double file that survives up to about $\varphi = 35\%$. At that concentration, the suspension for $\lambda = 20$ shows a significantly higher $\eta_{eff}$, which is about 1.45 times that corresponding to $\lambda = 1$.

In summary, the suspension viscosity shows a rich behavior depending on the viscosity contrast $\lambda$. For small enough $\varphi$, the more rigid particles can either show lower or higher normalized viscosity depending on initial conditions. This points to a non trivial fact that data handling in experiments inherently contain statistical variances not only due to noise and natural imperfections and variety of samples, but

also due to the very nature of multi-stability of solutions reported on here. This sheds a new light for future interpretations of rheology of soft suspensions. Beyond a certain concentration, the softer particles exhibit order (e.g. double file), whereas more rigid particles show disorder, resulting in a much higher effective viscosity. Note finally, that the appearance of order (soft enough particles) and disorder (for more rigid particles) is not a 2D property, but also a 3D property, shown both theoretically for model systems (drops, capsules, vesicles) and experimentally for RBCs [Shen et al., 2018]. The present study can thus serve as a guide for a systematic analysis in 3D.

## 5.4 Conclusion

A major central point of this study is that the existence of two attractors leads to a rheology which depends on initial configurations. This happens in the dilute and the semi-dilute regimes, up to about a concentration of 12%. Beyond that concentration, the attractors loose their identities. Still, the viscosity contrast affects significantly the value of the effective viscosity as shown in Figure 5.6. Several diseases (such as malaria) are accompanied by hardening of the RBC cytoplasm, a fact which can be mimicked by a higher internal viscosity (and thus higher viscosity contrast). This leads to a higher effective viscosity in microcirculation compromising the efficiency of oxygen transport.

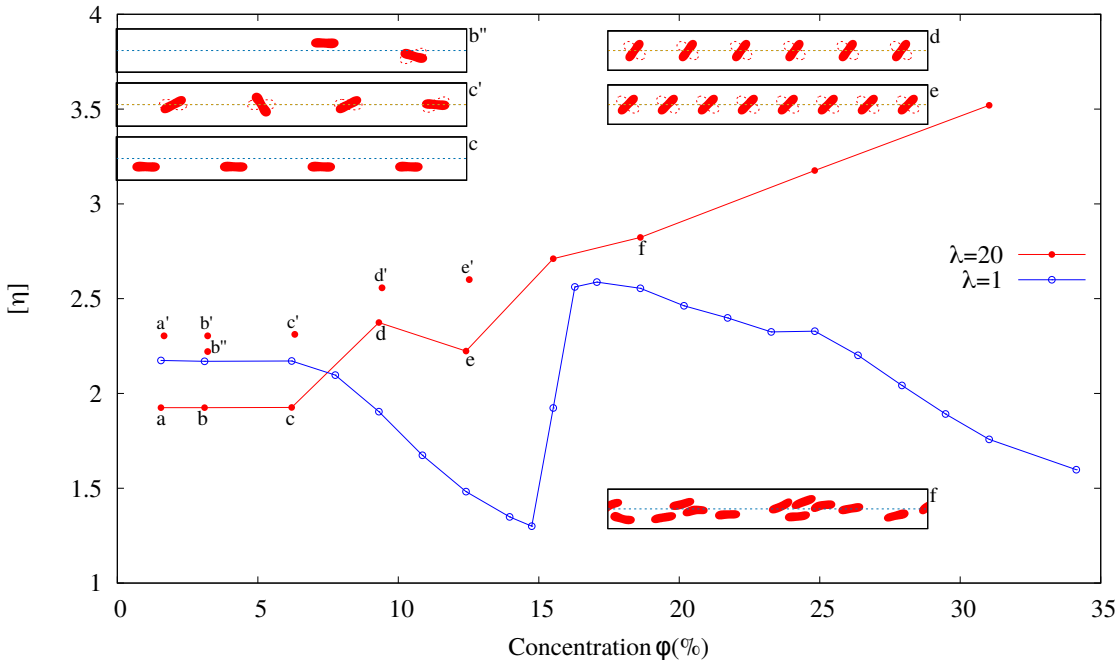


Figure 5.5: The evolution of $[\eta]$ as a function of concentration $\varphi$ for typical values of $\lambda$. Here we set $C_\kappa = 1$ and $C_n = 0.4$. The initial position of the vesicles has impact on the rheology up to $\varphi \simeq 12.4\%$. Points $a$, $b$ and $c$ on the curve correspond to FA configuration (a typical configuration is shown in inset $c$). Points $a'$, $b'$ and $c'$ on the curve correspond to another type of configuration (centered TB; a typical configuration is shown in inset $c'$) obtained from different initial conditions as compared to $a$, $b$ and $c$ configurations. Point $b''$ on the curve corresponds to another configuration which is a mixed state, in which a vesicle undergoes an off-centered TB, whereas the second one shows FA (see inset $b''$). Points $d$ and $e$ on the curve correspond to centered TB configuration (see inset $d$ and $e$ *resp.*). Points $d'$, $e'$ and f on the curve correspond to disordered configuration (a typical configuration is shown in inset $f$). The blue curve ($\lambda = 1$) is taken from Ref. [Thiébaud et al., 2014]. Configurations a, b and c are obtained from initial conditions where the vesicle are equidistant and set close to lower wall ($0.72R_0$ distance from the wall). Configuration $d$ and $e$ are obtained with initial set of equidistant vesicles at the center. Configuration $f$ is obtained with random initial positions. Configurations $a'$, $b'$ and $c'$ are obtained from initial conditions where the vesicle are equidistant and set at the center. It is noteworthy that we may also obtain the points $b'$ and $c'$ with initial random positions with a much longer simulation time. Configurations $d'$ and $e'$ are obtained with initial random positions. Configuration $b''$ is obtained with a vesicle at the center and the other close to the wall ($0.72R_0$ distance from the wall).

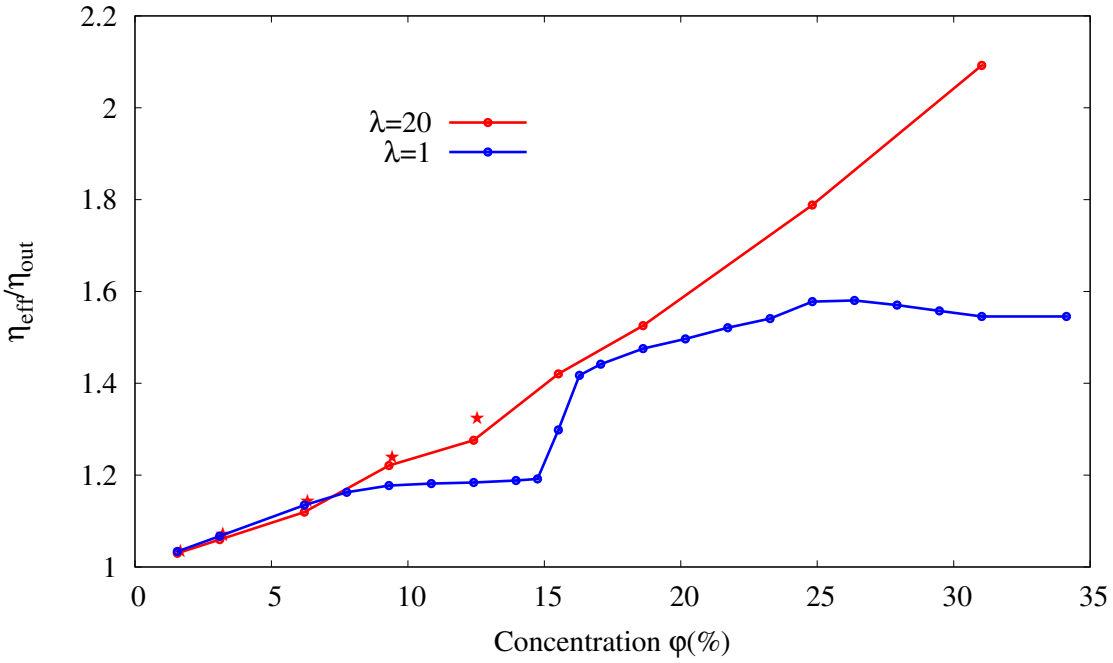


Figure 5.6: The evolution of the effective viscosity $\eta_{eff}$ as a function of concentration $\varphi$ for two values of $\lambda$. The filled circles (red curve) and the stars correspond to $\lambda = 20$, a value which leads to different spatial configurations of the suspension which in turn give rise to different values of $\eta_{eff}$ (or $[\eta]$) as explained in the caption of Figure 5.5. The stars are the counterparts of the points $a' - e'$ and $b''$ in Figure 5.5. In the dilute regime the suspension of relatively rigid vesicles ($\lambda = 20$) may have a lower value of $\eta_{eff}$ than that of a suspension of soft vesicles ($\lambda = 1$). This is traced back to the existence of off-centered positions for $\lambda = 20$ as discussed in the text. In the more concentrated regime, the suspension of relatively soft vesicles ($\lambda = 1$) has a much lower $\eta_{eff}$ than that of a suspension of relatively rigid vesicles. This is traced back to the existence of ordered solutions with a double file configuration for $\lambda = 1$ and disordered solutions for $\lambda = 20$. See the text for more details.

# Chapter 6

# Local rheology of a confined vesicle suspension

In this chapter, we investigate the local rheology of a suspension of vesicles under confined Poiseuille flow. We extracted the local averaged shear rate, concentration profile and local shear stress for different values of channel's width and global concentration. An introduction is presented in Section 6.1. The method and physical quantities are depicted in Section 6.2. The effect of flow strength on the constitutive law of a suspension of vesicles is discussed in Section 6.3.1. A universal law is discussed in Section 6.3.2.2. We shall show that the local fluidity can be well described as a function of the local concentration only, independent of the channel's width within which the suspension flow takes place or the global concentration of the suspension. Sections 6.4 is devoted to a conclusion.

## 6.1 Introduction

Blood cells are mainly RBCs, which transport oxygen and expulse wastes, and have a volume concentration (hematocrit) of $40-45\%$, which represents $99\%$ of the cellular fraction. In microcirculation, the objective of this thesis, they flow in vessels with diameters in the range $[5\mu m - 30mm]$ [Baskurt et al., 2011]. Here we are interested in small capillaries where the exchange of the oxygen and the carbon dioxide takes place. In the literature there is a tremendous amount of works which have been devoted to studying the global rheology of blood flow (see Section 1.3 in Chapter 1). A rheological property that is commonly of interest is the normalized viscosity $[\eta]$ as seen in the previous chapters, which describes the effective viscosity of the whole suspension. However despite this large interest in a better understanding of the rheology of blood flow, to the best of our knowledge, there is almost no study addressing the issue

of local rheology of blood flow. To date, there has been a great advance in local rheology of soft glasses, a class of materials including e.g. foams, emulsions and colloidal gels [Goyon et al., 2008, Sbragaglia et al., 2012, Benzi et al., 2014, Benzi et al., 2016, Mansard and Colin, 2012, Goyon et al., 2010, Dollet et al., 2015]. These studies pointed out the existence of cooperativity effect for dense suspensions (i.e. local fluidity is not only a function of local stress and local shear rate, but also depends on the state of the surrounding particles). We will investigate here also the presence or the lack-thereof of cooperativity within a model of RBCs suspension.

In the microcirculation, the blood is far from being a homogeneous fluid. Most of the research on confined blood flow has focused on the famous Fåhræus and Lindqvist effect [Fåhræus and Lindqvist, 1931, Pries et al., 1992, Popel and Johnson, 2005, Pries et al., 1996], where the RBCs tend to accumulate towards the blood vessel center. The latter effect leads to strong spatial variations of the RBCs concentration profile [Shen et al., 2016, Narsimhan et al., 2013, Saadat et al., 2019, Qi and Shaqfeh, 2017]. Thus the notion of an overall effective viscosity is ill-defined, since it is assumed that the shear rate is constant in the gap. Indeed, based on this effective viscosity we could identify several non-Newtonian rheological characteristics of blood such as shear-rate-dependent-viscosity (shear-thinning and shear-thickening), yield stress, etc... However, this overall effective viscosity does not fully describe the blood flow rheology. Therefore we must resort to an analysis of local rheology, where many different inhomogeneous structures of the suspended entities emerge, e.g. shear bands, cell free layers, etc...

The aim of the present Chapter is to infer the constitutive law of blood in a wide range of parameters (channel's width $W$, global hematocrit $\varphi_0$ and flow strength $\alpha$). We shall introduce unprecedented results of blood flow, which link the local fluidity (inverse of local viscosity) to the local concentration regardless of the gap's width and global concentration. In this study, we shall consider 2D vesicle using *Boundary Integral Method* (BIM). A collaboration with J. Harting and O. Aouane (Helmholtz-Institute Erlangen-Nürnberg, Germany) has confirmed the overall picture in 3D capsule (another model of RBC) using *Lattice Boltzmann method* (LBM).

## 6.2 Method and physical quantities

In this chapter two different methods have been used: *Boundary Integral Method* and *Lattice Boltzmann Method*. We consider a set of 2D vesicles and 3D capsules under confined pressure-driven flow. In 3D, the membrane has additionally a shear elastic energy. Here we only give the value of parameters used in this study (which are introduced in previous chapters) and introduce some new others. The imposed 2D Poiseuille flow is given by:

$$\begin{cases} v_x^0 = \alpha y\,(W - y) \\ v_y^0 = 0 \end{cases} \tag{6.1}$$

here the walls are at $y = 0$ and $y = W$, where $W$ is the channel width. $\alpha = \Delta P/(2\eta_{out}L)$ is considered to be the flow strength and its unit is $1/(t_c R_0)$, where $t_c = 1/\dot{\gamma}_{wall}$ and $\dot{\gamma}_{wall}$ is shear rate at the wall ($\dot{\gamma}_{wall} \sim 10^3 s^{-1}$). $\Delta P/L$ is the pressure drop over the channel divided by its length and $\eta_{out}$ is the viscosity of the suspending fluid. The viscosity contrast is set to one ($\lambda = 1$) and the reduced area is kept at 0.7 ($\tau = 0.7$). In this chapter we vary the value of channel width $W$ (or confinement), flow strength $\alpha$ and global concentration $\varphi_0$.
In 3D, we have set the reduced volume $\tau^{3D} = 0.65$ and the viscosity contrast $\lambda = 5$. The capillary number based on shear elasticity modulus $\kappa_s$ is given by $C_s = \eta_{out}\dot{\gamma}R_0/\kappa_s$. Since the 2D and 3D simulations have revealed the same overall qualitative features, most results focus here on 2D.
The physical quantities of interest to be extracted locally in this study are the following:

- Local shear rate or velocity profile ($\dot{\gamma} = \partial_y v_x$).
- Local shear stress $\sigma$.
- Local concentration $\varphi$.

In Figure 6.1 and its caption, we explain the method used to calculate the local concentration, and it is akin to the calculation of other quantities.

### Local shear stress in 2D

The stress distribution can be extracted (just by using momentum conservation) from mechanical equilibrium by considering the *Stokes* limit: $div\boldsymbol{\sigma} = \mathbf{0}$, which leads to i) $\partial_y \sigma_{xy} = \partial_x\,(p - \sigma_{xx})$ and ii) $\partial_x \sigma_{xy} = \partial_y\,(p - \sigma_{yy})$ where $p$ is the pressure, $x$ the

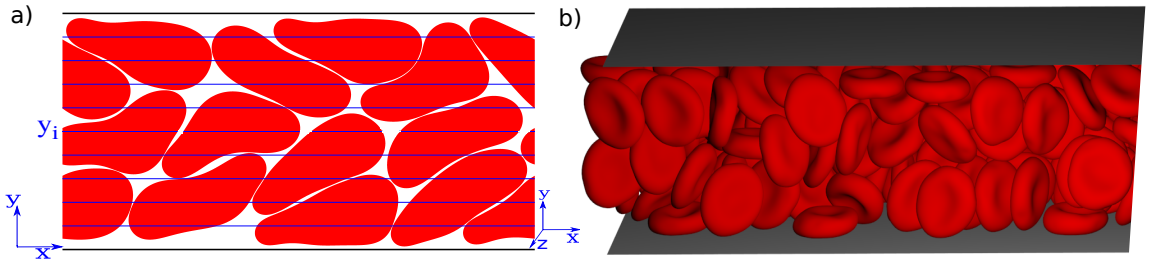


Figure 6.1: A graphical representation of how the local concentration is calculated in 2D and 3D. The computation domain is meshed with lines parallel to the walls (planes in 3D). For example the local concentration $\varphi$ at the position $y_i$ is the summation of the length of the segments over the total length of the channel (see a)). The same procedure is used in 3D using planes parallel to the walls. We use the same mesh to calculate other physical quantities, namely local stress and local shear rate (or velocity profile). All the quantities are averaged over horizontal line (plane in 3D) and over time. The 2D local stress $\sigma$ is obtained analytically, see the text.

streamwise direction and $y$ the spanwise direction. Using the two last equations and considering that the flow is fully developed (i.e., the stress components are streamwise invariant) we can get $\partial_y^2\sigma_{xy} = \partial_x^2\sigma_{xy} - \partial_y\partial_x\left(\sigma_{xx} - \sigma_{yy}\right) = 0$, then $\partial_y\sigma_{xy} = cte$. Using i) and the assumption that the stress vanishes at the center of channel, we easily get $\sigma_{xy} = -(\Delta p/L)\left(y - y_0\right)$ where $L$ is the channel length, $\Delta p = p_{inlet} - p_{outlet}$ and $y_0 = W/2$ is the center of channel. Using the expression of $\alpha$ introduced above, we get:

$$\sigma(y) = -2\eta_{out}\alpha\left(y - W/2\right) \tag{6.2}$$

In other words, whatever the constitutive law, the stress is given by this relation.

## 6.3 Results and discussion

We have split up this chapter into two parts: *In the first one* we have investigated the effect of the flow strength on the constitutive law of a suspension of vesicles. We shall show that all the rheological curves, which are obtained from different flow strength ($\alpha$), collapse into a single curve pointing out that the cooperativity does not make sense in our suspensions of vesicles. *Along the second part* we shall introduce a universal law for blood flow. We run many simulations with a global concentration ranging from dilute suspension up to $\varphi_0 \approx 70\%$ and channel width ranging from $3R_0$ to $9R_0$ (we remind that for RBC $R_0 \approx 3\mu m$). We shall show that for any given $\varphi_0$ and $W$ the relationship between the local fluidity $f$ and the local concentration $\varphi$ is deterministic and linear both for the 2D and 3D cases.

### 6.3.1 Does cooperative effect exist in blood flow?

We are interested in this section in the local flow curves of suspension of vesicles, which relate the local shear stress $\sigma$ to the local shear rate $\dot{\gamma}$. After the work of L. Bocquet and co-workers [Goyon et al., 2008], the study of non-locality and cooperativity effects of emulsions has gained interest. It has been demonstrated that a concentrated emulsion confined in gaps of different thicknesses shows an absence of an intrinsic local flow relating stresses and strain rates. They found experimentally that the weakly confined suspensions show the same local constitutive law for different flow strength and a simple Herschel-Bulkley model, $\sigma = \sigma_0 + A\dot{\gamma}^{1/2}$, with $\sigma_0$ a dynamical yield stress and $A$ a material constant, is enough to describe the flow. However, for highly confined suspensions, it was found that/ there is no universal local relationship between stress and shear rate and the suspensions exhibit different local flow rules for1 different pressure drop values as we can see in Figure 6.2. They have demonstrated that the local fluidity is not a function of the local stress, but also depends on the state of the system in the neighborhood of this zone, with a spatial correlation length typically equal to a few particles.

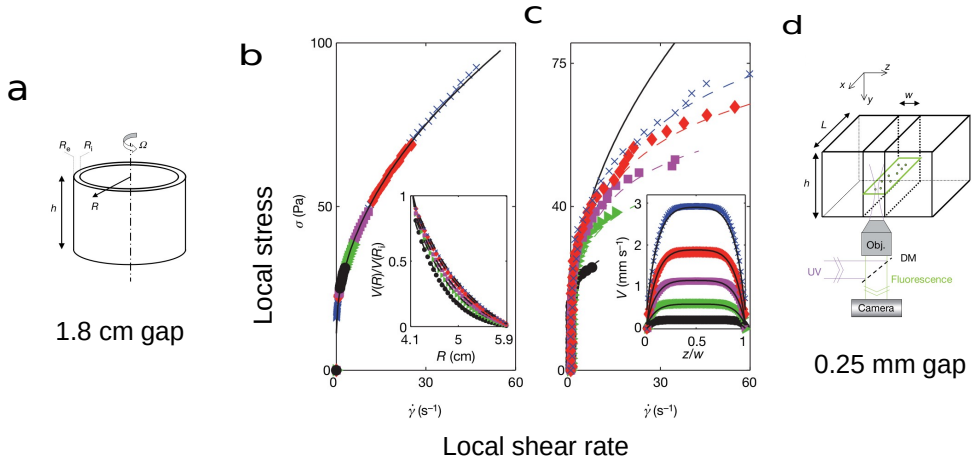


Figure 6.2: Local flow curves $\sigma(\dot{\gamma})$ (b and c) measured in the gap of $1.8cm$ of a Couette geometry (a) and in a microfluidic device with a gap of $250\mu m$ (d), during the flow of a concentrated emulsion of droplets ($\sim 6.5\mu m$ in diameter) with concentration $\varphi = 75\%$. Different colors correspond to different imposed rotational velocities (b) or different imposed pressure drops (c). Figure from [Goyon et al., 2008].

Following the aforementioned study, we consider a concentrated suspension of vesicles with $\varphi_0 = 81.68\%$ and $W = 5R_0$. We extract the relationship between local

stress and local shear rate for different flow strengths $\alpha$. The corresponding velocity profiles (along $x$ direction) are shown in Figure 6.3. In Figure 6.4 we show the main results. In that figure, all the curves show three main zones, the point at origin (in Figure 6.4) corresponds to the center of the channel and the last point on the curves on the right corresponds to the edge, these zones are (see Figure 6.5): i) center zone where the local shear rate is nearly zero, ii) shear band, where the local shear rate increases rapidly with position, and iii) cell-free layer, where $\sigma$ is linearly dependent on $\dot{\gamma}$ (Newtonian liquid). In Figure 6.4, we also remark that the cell-free layer thickness increases with the pressure drop as has been reported for instance in [Freund and Orescanin, 2011] and references therein. From Figure 6.4, it seems that the suspension with a fixed concentration exhibits different constitutive laws as for droplets emulsion seen previously. However, by rescaling the local stress and the local shear rate by the corresponding flow strength $\alpha$, it turns out that all the rheological laws collapse into a single curve, thus ruling out the existence of any non-local and cooperativity effect.

In short, we exhibit here the absence of cooperativity effect in our confined vesicle suspension for $W = 5R_0$. A preliminary result for another value of confinement ($W = 20R_0$) also does not point to any clear cooperativity effect.

### 6.3.2 Universal law: local fluidity *versus* local concentration

#### 6.3.2.1 Effect of confinement and concentration on constitutive law

We first investigate the effect of confinement and global concentration (also known as hematocrit for RBCs) on the constitutive law of a suspension of vesicles. The results are presented in Figure 6.6 for concentrations $\varphi_0 = 44\%$ (Fig.6.6a) and $\varphi_0 = 69.12\%$ (Fig.6.6b), and for two values of confinement $W = 3R_0$ and $W = 7R_0$. We have seen before that the local rheological curves show three different zones, namely cell-free layer (absence of vesicles), shear band and the center of channel where the averaged streamwise velocity is almost flat. In Figure 6.6, we see that all these three zones are highly affected by the global parameters ($W$ and $\varphi_0$). For instance the cell-free layer thickness decreases with the concentration as it has been found in the literature [Qi and Shaqfeh, 2017, Fedosov et al., 2010, Xu and Kleinstreuer, 2019, Narsimhan et al., 2013]. From Figure 6.6, we can also see that the center zone (first part of the curves where $\dot{\gamma}$ increases slowly with $\sigma$), becomes larger when the concentration increased (from panel a) to b) in Figure 6.6) where the suspensions tends to be packed. In short, the local constitutive law shows different local behavior depending on the global

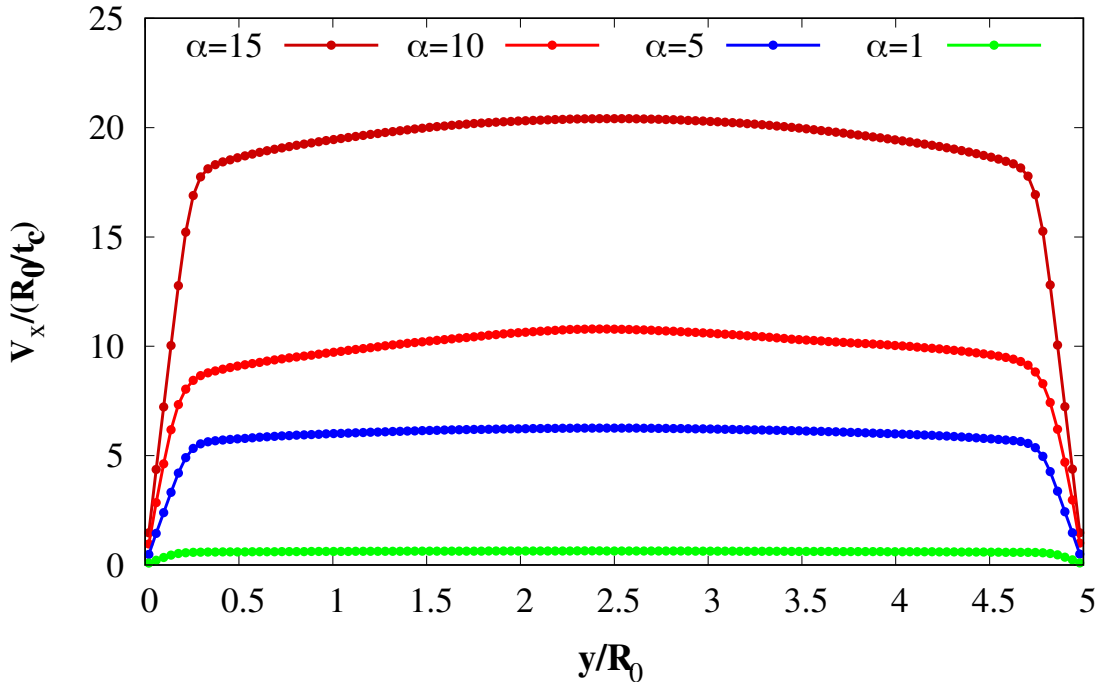


Figure 6.3: Averaged streamwise component velocity along the cross-flow coordinate $y/R_0$ for different pressure drops (or different flow strength $\alpha$). The simulations here are conducted at a $\varphi_0 = 81.68\%$ and $W = 5R_0$.

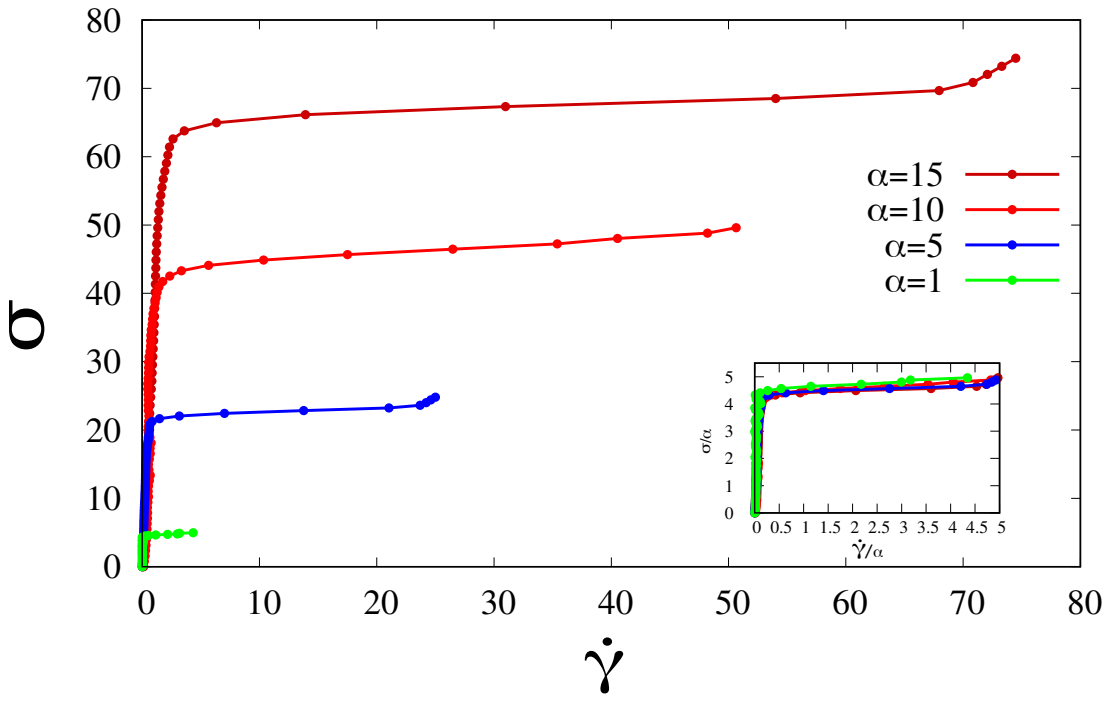


Figure 6.4: Local constitutive laws for a suspension of vesicles with $\varphi_0 = 81.68\%$ for different flow strengths $\alpha$. The inset reports the same laws rescaled by corresponding $\alpha$ ($\sigma/\alpha$ *vs* $\dot{\gamma}/\alpha$). Due to the symmetry reasons, we only plot the results for an half of the channel. Here the origin of the graph corresponds to the center of the channel.

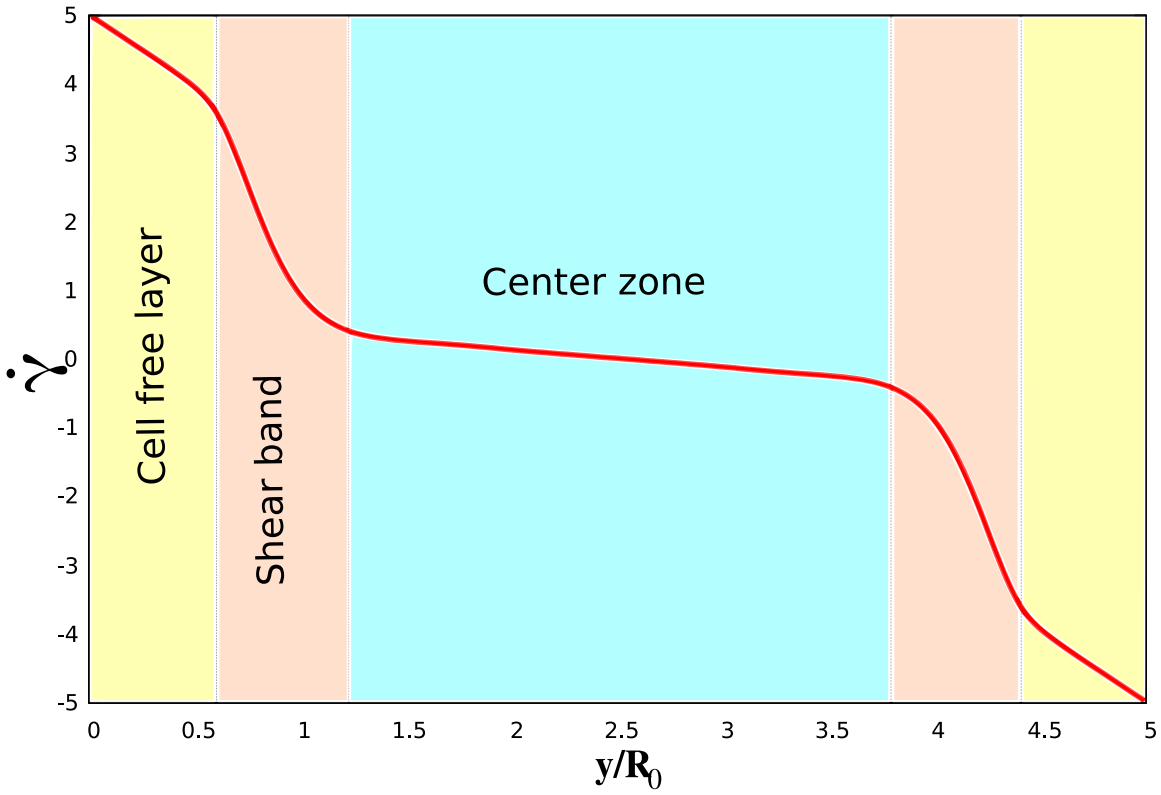


Figure 6.5: Shear rate as a function of position. Here we show the three main zones discussed in the text.

parameters, namely channel width $W$ and global concentration $\varphi_0$. The question, which then arises, is: Is there any universal law which links the local stress and local strain rate for any value of channel width $W$ and global concentration $\varphi_0$?

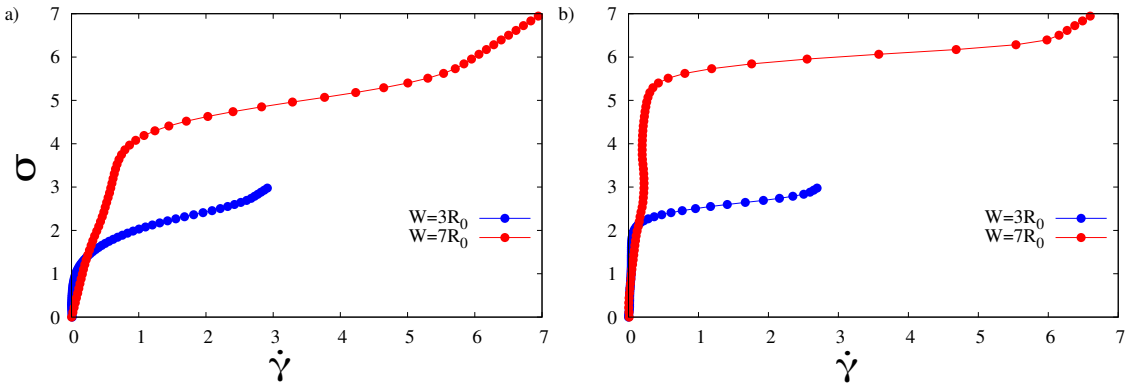


Figure 6.6: Local rheological curves, (i.e. the local stress *vs.* the local strain rate) for two values of confinement $W = 3R_0$ and $W = 7R_0$. a) $\varphi_0 = 44\%$. b) $\varphi_0 = 69.12\%$.

#### 6.3.2.2 Link between local stress and local strain rate for different local concentrations

To answer the above question, we have run simulations with different values of global concentration $\varphi_0$ and channel width $W$. In Figure 6.7 we show typical concentration profiles, which are roughly symmetric with respect to the center of channel. We can see that the concentration profiles may show one or more than one peak. These different distributions of particles are traced back to two antagonist effects: (i) the wall-induced lift that pushes the RBCs towards the channel center, and (ii) particle-particle hydrodynamic interactions induce random-like lateral motions of RBCs, with a net flux down the concentration gradient, toward the wall. This effect is known as shear-induced diffusion. Moreover, in the case of relatively low values of global concentration (blue curve in Figure 6.7), the first effect stated above prevails over the second one which is minor due to lesser number of particles (i.e. the interactions between particles are less pronounced), thus the RBCs migrate towards the center of the channel, forming a single peak. However, when the global concentration increases, the two antagonist effects become competitive, leading thus to two peaks (orange and red curves in Figure 6.7).

A central key point of our analysis is to seek whether or not for a local given concentration there exists a universal law? For that purpose we first investigate how

the fluidity ($f = \frac{\dot{\gamma}}{\sigma}$) evolves for any fixed value of local concentration, whatever the value of channel width $W$ and global concentration $\varphi_0$. To do so, we fix a value of local concentration $\varphi$ (dashed lines for example in Figure 6.7), then the intersection of $\varphi$ with the concentration profiles of all explored $W$ and $\varphi_0$ gives lateral positions (at least two intersections (positions), see Figure 6.7). From these lateral positions we obtain a local strain rate $\dot{\gamma}$ and calculate the equivalent local stress $\sigma$ by using equation 6.2. The obtained pairs ($\sigma$, $\dot{\gamma}$) are presented in Figure 6.8 for typical values of local concentration ($\varphi$ can be chosen in the range $[0 : 100\%[$).

The most striking result that emerges from Figure 6.8, is that, for a given value of $\varphi$, all the pairs ($\sigma$,$\dot{\gamma}$) fall closely on straight lines for all explored values of $W$ and $\varphi_0$. The slope of these lines is local viscosity $\eta$, and it is shown as a function of local concentration $\varphi$ in Figure 6.9a. The main results of this chapter are presented in Figure 6.9b. From there, we can see that the local fluidity (inverse of local viscosity) can be well described linearly as a function of the local concentration only, independently of the channel's width $W$ within which the suspension flow takes place or the global concentration of the suspension $\varphi_0$, pointing thus to a universal law for suspension of vesicles which is a simple model of blood flow. The 3D rheological law follows the same trends as in 2D (see Figure 6.10).
It is noteworthy that this law ($f = \frac{\dot{\gamma}}{\sigma} = 1 - 1.09\varphi$, obtained by fitting data points in Figure 6.9b with $f = a\varphi + b$) can be used in order to reproduce vesicle distribution $\varphi$ by giving shear rate $\dot{\gamma}$ or vice versa. In Figures (6.11, 6.12), we show profiles ($\varphi$ and $\dot{\gamma}$) obtained from our local rheological law and also those obtained directly from simulations. We emphasize that this universal law is able to reproduce the concentration and shear rate profiles.

## 6.4 Conclusion

In this chapter, the local rheology of a suspension of vesicles in a confined pressure-driven flow has been investigated numerically. We have shown that the flow strength does not affect the local constitutive law, thus no evidence of cooperativity effect in the suspensions is observed. We have also shown that the local fluidity is linearly dependent on the local concentration, whatever the value of channel width and global concentration of vesicles. This universal law constitutes a major breakthrough in the rheology of complex fluids (e.g. blood flow) in a soft matter area. This finding

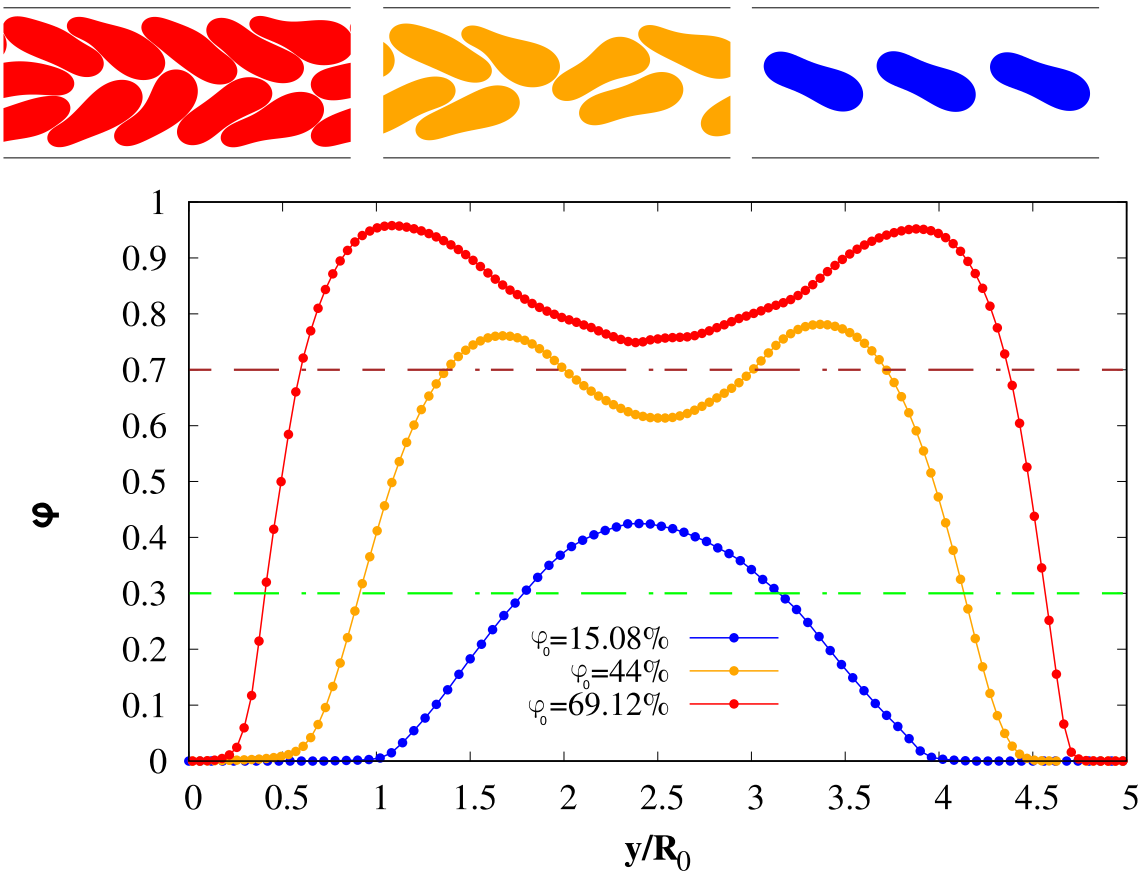


Figure 6.7: Concentration profiles of suspensions for different global concentrations $\varphi_0$. We also show the corresponding vesicle configurations. The dashed lines correspond to different random local concentrations. Here $W = 5R_0$.

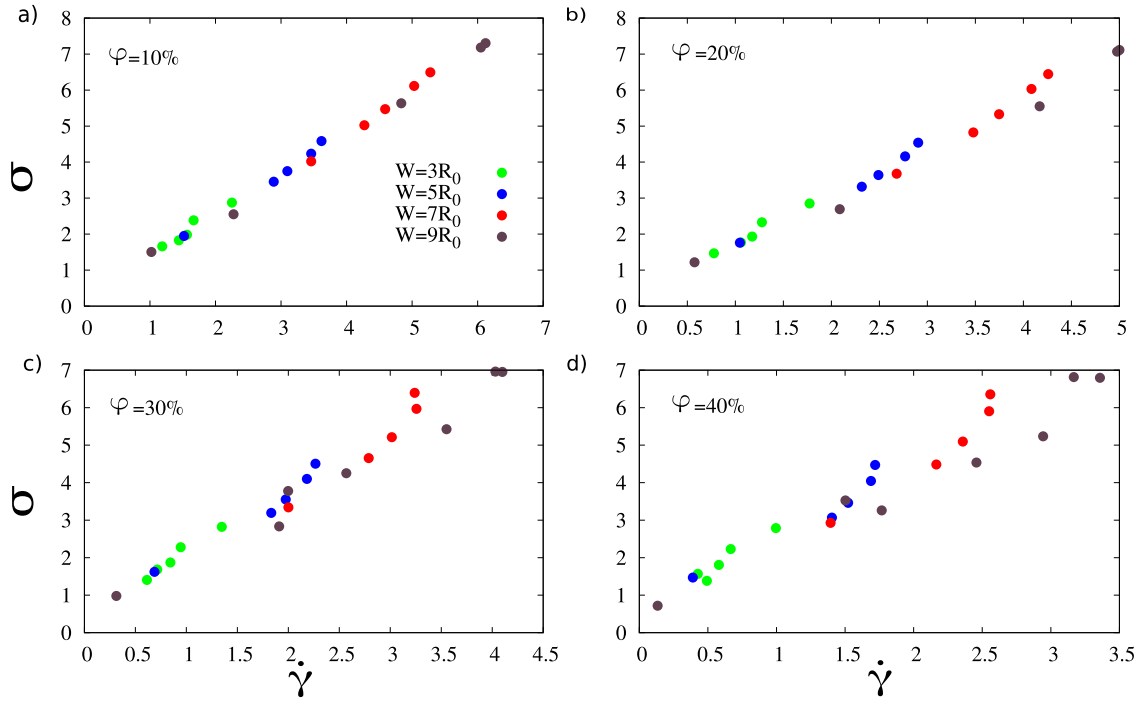


Figure 6.8: Local stress $\sigma$ *versus* local shear rate $\dot{\gamma}$ for different local concentrations $\varphi$ obtained from different values of channel width $W$ and global concentrations $\varphi_0$. The legend of a) applies also to other sub-figures. Here different points of the same color correspond to the different global concentrations $\varphi_0$.

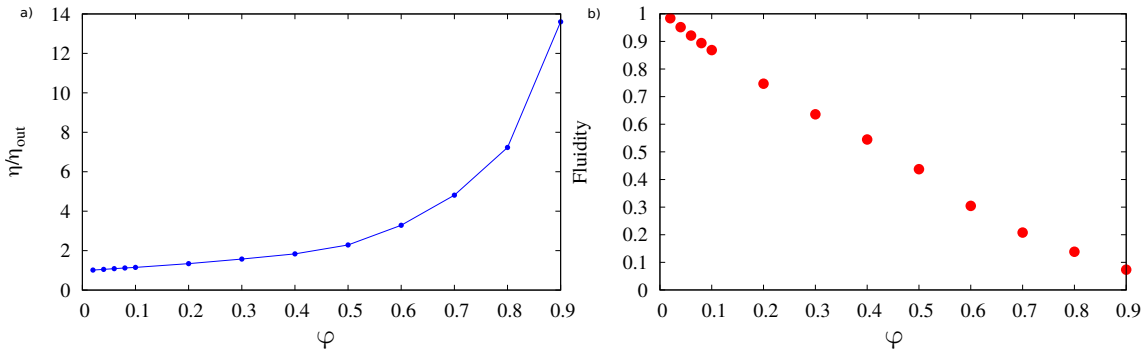


Figure 6.9: a) Local viscosity $\eta$ ( b) Local fluidity) as a function of local concentration $\varphi$ valid for any value of channel width $W$ and global concentration $\varphi_0$. The local viscosity $\eta$ diverges when $\varphi \to 1$, and $\eta \to \eta_{out}$ when $\varphi \to 0$. All points of fluidity are roughly on the same straight line: $f = 1 - 1.09\varphi$.

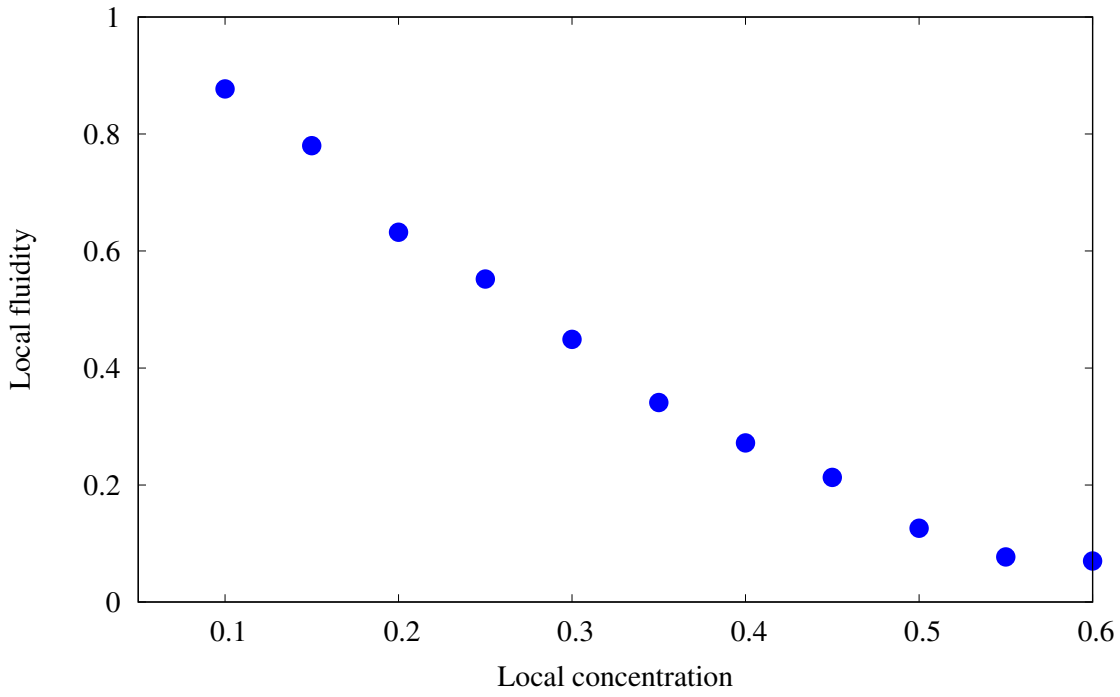


Figure 6.10: Local fluidity as a function of local concentration $\varphi$ for 3D case valid for any value of channel width $W$ and global concentration $\varphi_0$.

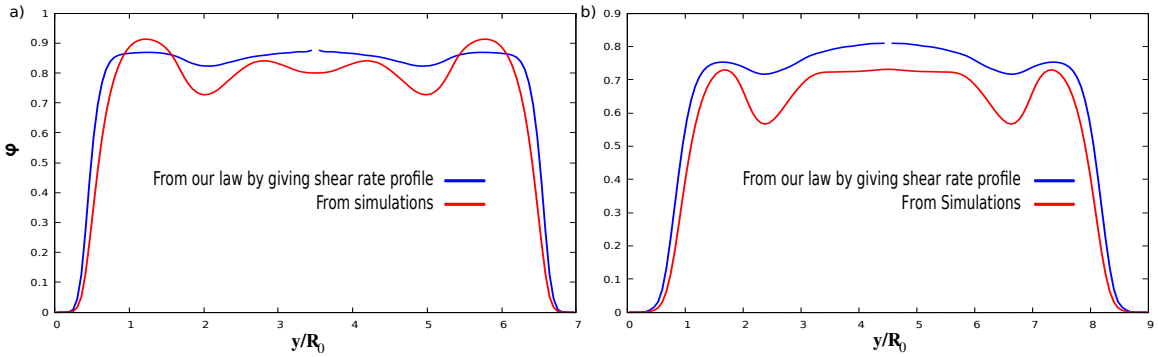


Figure 6.11: Concentration profiles $\varphi$ of suspensions of vesicles obtained from the fluidity law seen above providing the corresponding shear rate profiles (the stress is always given by 6.2) and $\varphi$ directly from simulations. It is clear that our universal law can reproduce the concentration profiles with some minor defects. a) $\varphi_0 = 69.11\%$ and $W = 7R_0$. b) $\varphi_0 = 53.86\%$ and $W = 9R_0$.

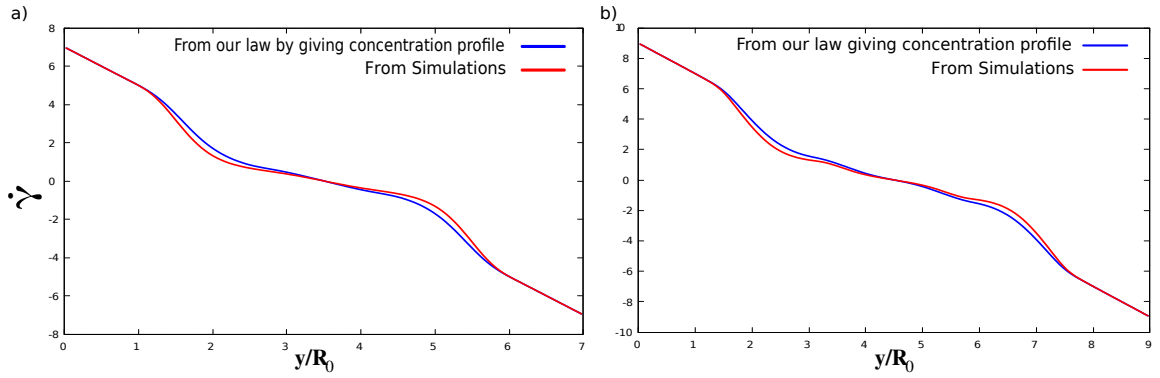


Figure 6.12: Shear rate profiles $\dot{\gamma}$ of suspensions of vesicles obtained from the fluidity law seen above providing the corresponding concentration profiles (the stress is always given by 6.2) and $\dot{\gamma}$ directly from simulations. It is clear that our universal law can reproduce the shear rate profiles with some minor defects. a) $\varphi_0 = 25.14\%$ and $W = 7R_0$. b) $\varphi_0 = 25.14\%$ and $W = 9R_0$.

constitutes a universal rheological law for RBCs, and it needs to be verified for other soft/hard particles.

# Chapter 7

# Conclusions and perspectives

In this chapter we briefly recall the main results and then present a list of questions which should constitute an interesting task for future investigations. The main topic of this thesis has focused on the rheology of RBC suspensions. The main findings and some perspectives are summarized below:

## 7.1 Summary of Chapter 3 and related perspectives

In Chapter 3, the shear-rate-dependent viscosity of a suspension of vesicles (a simple model of RBCs suspension) under confined shear flow is investigated in 2D numerical simulations. A link between the organization of the RBC suspension and rheology has been analyzed. An interesting feature is discovered: the suspension can exhibit both shear-thinning (decreasing viscosity with shear rate) and shear-thickening (increasing viscosity with shear rate) depending on viscosity contrast $\lambda$. This is traced back to the way the suspension organizes itself as a function of the shear rate.

The present work opens a set of perspectives:

- A more systematic analysis of the parameters is important to decipher the complex rheological behavior of blood flow. For instance, considering the particles with high values of viscosity contrast where the tumbling motion prevails.

- Here no rouleaux are allowed to form due to the absence of any nonhydrodynamic interactions between cells. The presence of macromolecules, like plasma proteins, allow to form rouleaux of RBCs. Taking into account the presence of adhesion between cells is an interesting task to be explored.

- In the microcirculation, RBCs flow in cylindrical channels and not in confined shear flow. An extended study in confined Poiseuille flow and 3D extension are needed for a more comprehensive understanding of blood rheology.

## 7.2 Summary of Chapter 4 and 5 and related perspectives

In Chapter 4 and 5, the lateral migration of a suspended vesicle in a bounded shear flow is investigated numerically. It has been long believed that a vesicle under confined linear shear flow in the absence of inertia will migrate across the streamline and settle in the center of the channel. Our numerical study reveals that this scenario does not always hold. By increasing the internal viscosity of the suspended entity (i.e. increasing $\lambda$), we discover that the final position can be off-centered, a solution (attractor) that may either coexist (saddle node bifurcation) or not (pitchfork bifurcation) with the stable centered solution. We fully characterize the different solutions as a function of relevant control parameter. The overall picture is confirmed in 3D and hence cannot be due to projection effects. The emergence of new solutions has strong impact on the rheological properties. The existence of two attractors continues to affect rheology up to a concentration $\varphi \approx 12\%$. It would be interesting to investigate the same study in the future in a pipe flow which is a more relevant scenario for blood flow, and to link between this work and oxygen transport in the microcirculation.

## 7.3 Summary of Chapter 6 and related perspectives

In Chapter 6, the local rheology of a suspension of vesicles under confined Poiseuille flow is addressed by means of computer simulations. We have extracted the local concentration of vesicles, the local shear rate and the local stress. We have found that a suspension of vesicles exhibits a single local rheological law whatever the flow strength is. Our main finding in this work is that the local fluidity can be described linearly as a function of the local concentration only, regardless the value of channel's width $W$ within which the flow suspension takes place or the global concentration of the suspension $\varphi_0$. This constitutes a universal law for blood flow. Some perspectives of this work are outlined here:

- Since our model does not take into account the adhesion force between cells, it will be an interesting task to implement adhesion for having a more complete description of blood flow, and see how the adhesion alter this local law.
- In the physiological conditions, the blood flows in a network structure. An extended study in complex geometries should be addressed in the future.
- An experimental protocol should be envisaged to confront with our numerical universal law.

# References


[Abkarian et al., 2007] Abkarian, M., Faivre, M., and Viallat, A. (2007). Swinging of red blood cells under shear flow. *Physical review letters*, 98(18):188302. 3

[Abkarian and Viallat, 2008] Abkarian, M. and Viallat, A. (2008). Vesicles and red blood cells in shear flow. *Soft Matter*, 4:653–657. 4, 52

[Bagchi and Kalluri, 2010] Bagchi, P. and Kalluri, R. M. (2010). Rheology of a dilute suspension of liquid-filled elastic capsules. *Phys. Rev. E*, 81:056320. 32

[Bagchi and Murthy, 2009] Bagchi, P. and Murthy, K. R. (2009). Dynamics of non-spherical capsules in shear flow. *Phys. Rev. E*, 80:016307. 32

[Barabino et al., 2010] Barabino, G. A., Platt, M. O., and Kaul, D. K. (2010). Sickle cell biomechanics. *Annu. Rev. Biomed. Eng.*, 12:345–367. 11

[Barthès-Biesel, 2012] Barthès-Biesel, D. (2012). *Microhydrodynamics and complex fluids*. CRC Press. 21

[Barthes-Biesel and Acrivos, 1973] Barthes-Biesel, D. and Acrivos, A. (1973). Deformation and burst of a liquid droplet freely suspended in a linear shear field. *J. Fluid Mech.*, 61(01):1–22. 36

[Baskurt et al., 2011] Baskurt, O., Neu, B., and Meiselman, H. J. (2011). *Red blood cell aggregation*. CRC Press. 84

[Baskurt and Meiselman, 2003] Baskurt, O. K. and Meiselman, H. J. (2003). Blood rheology and hemodynamics. In *Seminars in thrombosis and hemostasis*, volume 29, pages 435–450. Copyright© 2003 by Thieme Medical Publishers, Inc., 333 Seventh Avenue, New .... 9

[Baskurt et al., 1997] Baskurt, O. K., Temiz, A., and Meiselman, H. J. (1997). Red blood cell aggregation in experimental sepsis. *Translational Research*, 130(2):183–190. 11

[Batchelor, 1970] Batchelor, G. (1970). The stress system in a suspension of force-free particles. *J. Fluid Mech.*, 41(3):545–570. 8, 33, 74

[Beaucourt et al., 2004a] Beaucourt, J., Biben, T., and Misbah, C. (2004a). Optimal lift force on vesicles near a compressible substrate. *Europhys. Lett.*, 67(4):676. 52

[Beaucourt et al., 2004b] Beaucourt, J., Rioual, F., Séon, T., Biben, T., and Misbah, C. (2004b). Steady to unsteady dynamics of a vesicle in a flow. *Phys. Rev. E*, 69:011906. 3, 46

[Benzi et al., 2016] Benzi, R., Sbragaglia, M., Bernaschi, M., Succi, S., and Toschi, F. (2016). Cooperativity flows and shear-bandings: a statistical field theory approach. *Soft Matter*, 12(2):514–530. 85

[Benzi et al., 2014] Benzi, R., Sbragaglia, M., Perlekar, P., Bernaschi, M., Succi, S., and Toschi, F. (2014). Direct evidence of plastic events and dynamic heterogeneities in soft-glasses. *Soft Matter*, 10(26):4615–4624. 85

[Biben et al., 2011] Biben, T., Farutin, A., and Misbah, C. (2011). Three-dimensional vesicles under shear flow: Numerical study of dynamics and phase diagram. *Phys. Rev. E*, 83(3):031921. 17, 64

[Bodnár et al., 2011] Bodnár, T., Sequeira, A., and Prosi, M. (2011). On the shear-thinning and viscoelastic effects of blood flow under various flow rates. *Applied Mathematics and Computation*, 217(11):5055–5067. 7

[Boedec et al., 2011] Boedec, G., Leonetti, M., and Jaeger, M. (2011). 3d vesicle dynamics simulations with a linearly triangulated surface. *Journal of Computational Physics*, 230(4):1020–1034. 3

[Boedec et al., 2017] Boedec, G., Leonetti, M., and Jaeger, M. (2017). Isogeometric fem-bem simulations of drop, capsule and vesicle dynamics in stokes flow. *Journal of Computational Physics*, 342:117–138. 54

[Bookchin and Lew, 1996] Bookchin, R. M. and Lew, V. L. (1996). Pathophysiology of sickle cell anemia. *Hematology/oncology clinics of North America*, 10(6):1241–1253. 10

[Bow et al., 2011] Bow, H., Pivkin, I. V., Diez-Silva, M., Goldfless, S. J., Dao, M., Niles, J. C., Suresh, S., and Han, J. (2011). A microfabricated deformability-based flow cytometer with application to malaria. *Lab Chip*, 11(6):1065–1073. 11

[Brooks et al., 1970] Brooks, D., Goodwin, J., and Seaman, G. (1970). Interactions among erythrocytes under shear. *Journal of Applied Physiology*, 28(2):172–177. 10

[Brust et al., 2014] Brust, M., Aouane, O., Thiébaud, M., Flormann, D., Verdier, C., Kaestner, L., Laschke, M., Selmi, H., Benyoussef, A., Podgorski, T., et al. (2014). The plasma protein fibrinogen stabilizes clusters of red blood cells in microcapillary flows. *Scientific reports*, 4:4348. 5

[Cantat and Misbah, 1999] Cantat, I. and Misbah, C. (1999). Lift force and dynamical unbinding of adhering vesicles under shear flow. *Phys. Rev. Lett.*, 83(4):880. 52, 57, 60, 73

[Chien, 1970] Chien, S. (1970). Shear dependence of effective cell volume as a determinant of blood viscosity. *Science*, 168(3934):977–979. 5, 8

[Chien, 1975] Chien, S. (1975). Biophysical behavior of red cells in suspensions. *The red blood cell*, 2(4):1031–133. 2, 5

[Chien et al., 1970] Chien, S., Usami, S., and Bertles, J. F. (1970). Abnormal rheology of oxygenated blood in sickle cell anemia. *J. Clin. Invest.*, 49(4):623–634. 11

[Chien et al., 1967a] Chien, S., Usami, S., Dellenback, R. J., and Gregersen, M. I. (1967a). Blood viscosity: influence of erythrocyte deformation. *Science*, 157(3790):827–829. 5, 10, 35

[Chien et al., 1967b] Chien, S., Usami, S., Dellenback, R. J., Gregersen, M. I., Nanninga, L. B., and Guest, M. M. (1967b). Blood viscosity: influence of erythrocyte aggregation. *Science*, 157(3790):829–831. 5

[Cokelet et al., 1963] Cokelet, G. R., Merrill, E., Gilliland, E., Shin, H., Britten, A., and Wells Jr, R. (1963). The rheology of human blood—measurement near and at zero shear rate. *Transactions of the Society of Rheology*, 7(1):303–317. 5

[Copley et al., 1973] Copley, A., Huang, C., and King, R. (1973). Rheogoniometric studies of whole human blood at shear rates from 1000 to 0.0009 sec- 1. *Biorheology*, 10(1):17–22. 5

[Coupier et al., 2008] Coupier, G., Kaoui, B., Podgorski, T., and Misbah, C. (2008). Noninertial lateral migration of vesicles in bounded poiseuille flow. *Phys. Fluids*, 20(11):111702. 52, 73

[Danker et al., 2007] Danker, G., Biben, T., Podgorski, T., Verdier, C., and Misbah, C. (2007). Dynamics and rheology of a dilute suspension of vesicles: Higher-order theory. *Phys. Rev. E*, 76(4):041905. 54, 64, 74

[Danker and Misbah, 2007a] Danker, G. and Misbah, C. (2007a). Rheology of a dilute suspension of vesicles. *Phys. Rev. Lett.*, 98:088104. 8, 32, 40

[Danker and Misbah, 2007b] Danker, G. and Misbah, C. (2007b). Rheology of a dilute suspension of vesicles. *Phys. Rev. Lett.*, 98:088104. 74

[Das et al., 1997] Das, B., Enden, G., and Popel, A. S. (1997). Stratified multiphase model for blood flow in a venular bifurcation. *Annals of biomedical engineering*, 25(1):135–153. 7

[Davit and Peyla, 2008] Davit, Y. and Peyla, P. (2008). Intriguing viscosity effects in confined suspensions: A numerical study. *EPL*, 83(6):64001. 9

[De Gennes and Gennes, 1979] De Gennes, P.-G. and Gennes, P.-G. (1979). *Scaling concepts in polymer physics*. Cornell university press. 51

[Dintenfass, 1968] Dintenfass, L. (1968). Internal viscosity of the red cell and a blood viscosity equation. *Nature*, 219(5157):956–958. 5

[Dintenfass, 1980] Dintenfass, L. (1980). *Molecular Rheology of Human Blood: Its Role in Health and Disease (to Day and to Morrow ?)*, pages 467–480. Springer US, Boston, MA. 11

[Doddi and Bagchi, 2009] Doddi, S. K. and Bagchi, P. (2009). Three-dimensional computational modeling of multiple deformable cells flowing in microvessels. *Phys. Rev. E*, 79:046318. 32

[Doi and Edwards, 1988] Doi, M. and Edwards, S. F. (1988). *The theory of polymer dynamics*, volume 73. oxford university press. 51

[Dollet et al., 2015] Dollet, B., Scagliarini, A., and Sbragaglia, M. (2015). Two-dimensional plastic flow of foams and emulsions in a channel: experiments and lattice boltzmann simulations. *Journal of Fluid Mechanics*, 766:556–589. 85

[Dupire et al., 2012] Dupire, J., Socol, M., and Viallat, A. (2012). Full dynamics of a red blood cell in shear flow. *Proceedings of the National Academy of Sciences*, 109(51):20808–20813. 3

[Einstein, 1906] Einstein, A. (1906). Eine neue bestimmung der moleküldimensionen. *Ann. Phys.*, 324(2):289–306. 7

[Embury et al., 1994] Embury, S. H., Hebbel, R. P., Mohandas, N., and Steinberg, M. (1994). *Sickle cell disease: basic principles and clinical practice*. Raven Press New York. 10

[Errill, 1969] Errill, E. (1969). Rheology of blood. *Physiological reviews*, 49(4):863–888. 7

[Fåhræus and Lindqvist, 1931] Fåhræus, R. and Lindqvist, T. (1931). The viscosity of the blood in narrow capillary tubes. *Am. J. Physiol.*, 96(3):562–568. 5, 13, 52, 73, 85

[Farutin et al., 2010] Farutin, A., Biben, T., and Misbah, C. (2010). Analytical progress in the theory of vesicles under linear flow. *Phys. Rev. E*, 81(6):061904. 64

[Farutin et al., 2014] Farutin, A., Biben, T., and Misbah, C. (2014). 3D numerical simulations of vesicle and inextensible capsule dynamics. *J. Comput. Phys.*, 275:539–568. 17

[Farutin and Misbah, 2012] Farutin, A. and Misbah, C. (2012). Squaring, parity breaking, and s tumbling of vesicles under shear flow. *Physical review letters*, 109(24):248106. 3

[Fedosov et al., 2010] Fedosov, D. A., Caswell, B., Popel, A. S., and Karniadakis, G. E. (2010). Blood flow and cell-free layer in microvessels. *Microcirculation*, 17(8):615–628. 89

[Fedosov et al., 2014] Fedosov, D. A., Noguchi, H., and Gompper, G. (2014). Multiscale modeling of blood flow: from single cells to blood rheology. *Biomech. Model. Mechan.*, 13(2):239–258. 32

[Fischer et al., 1978] Fischer, T. M., Stohr-Lissen, M., and Schmid-Schonbein, H. (1978). The red cell as a fluid droplet: tank tread-like motion of the human erythrocyte membrane in shear flow. *Science*, 202(4370):894–896. 2

[Fisher and Rossmann, 2009] Fisher, C. and Rossmann, J. S. (2009). Effect of non-newtonian behavior on hemodynamics of cerebral aneurysms. *Journal of biomechanical engineering*, 131(9):091004. 5

[Fornari et al., 2016] Fornari, W., Brandt, L., Chaudhuri, P., Lopez, C. U., Mitra, D., and Picano, F. (2016). Rheology of confined non-brownian suspensions. *Phys. Rev. Lett.*, 116(1):018301. 10

[Forsyth et al., 2011] Forsyth, A. M., Wan, J., Owrutsky, P. D., Abkarian, M., and Stone, H. A. (2011). Multiscale approach to link red blood cell dynamics, shear viscosity, and atp release. *Proc. Natl. Acad. Sci. U.S.A.*, 108(27):10986–10991. 1, 35

[Franceschini et al., 2010] Franceschini, E., Yu, F. T., Destrempes, F., and Cloutier, G. (2010). Ultrasound characterization of red blood cell aggregation with intervening attenuating tissue-mimicking phantoms. *The Journal of the Acoustical Society of America*, 127(2):1104–1115. 11

[Freund and Orescanin, 2011] Freund, J. B. and Orescanin, M. (2011). Cellular flow in a small blood vessel. *Journal of Fluid Mechanics*, 671:466–490. 89

[Fung, 2013] Fung, Y.-C. (2013). *Biomechanics: circulation*. Springer Science & Business Media. 51

[Ghigliotti et al., 2010] Ghigliotti, G., Biben, T., and Misbah, C. (2010). Rheology of a dilute two-dimensional suspension of vesicles. *J. Fluid Mech.*, 653:489–518. 16, 32, 33, 35, 39, 54, 74

[Ghigliotti et al., 2009] Ghigliotti, G., Selmi, H., Kaoui, B., Biros, G., and Misbah, C. (2009). Dynamics and rheology of highly deflated vesicles. *Esaim: Proc.*, 28:212–227. 32

[Gijsen et al., 1999] Gijsen, F. J., van de Vosse, F. N., and Janssen, J. (1999). The influence of the non-newtonian properties of blood on the flow in large arteries: steady flow in a carotid bifurcation model. *Journal of biomechanics*, 32(6):601–608. 5

[Goldsmith et al., 1972] Goldsmith, H., Marlow, J., and MacIntosh, F. C. (1972). Flow behaviour of erythrocytes-i. rotation and deformation in dilute suspensions. *Proc. R. Soc. Lond. B*, 182(1068):351–384. 2

[Goyon et al., 2010] Goyon, J., Colin, A., and Bocquet, L. (2010). How does a soft glassy material flow: finite size effects, non local rheology, and flow cooperativity. *Soft Matter*, 6(12):2668–2678. 85

[Goyon et al., 2008] Goyon, J., Colin, A., Ovarlez, G., Ajdari, A., and Bocquet, L. (2008). Spatial cooperativity in soft glassy flows. *Nature*, 454(7200):84. 13, 85, 88

[Grandchamp et al., 2013] Grandchamp, X., Coupier, G., Srivastav, A., Minetti, C., and Podgorski, T. (2013). Lift and down-gradient shear-induced diffusion in red blood cell suspensions. *Phys. Rev. Lett.*, 110(10):108101. 52

[Guckenberger and Gekle, 2017] Guckenberger, A. and Gekle, S. (2017). Theory and algorithms to compute Helfrich bending forces: A review. *J. Phys. Condens. Matter*, 29(20):203001. 16

[Guckenberger and Gekle, 2018] Guckenberger, A. and Gekle, S. (2018). A boundary integral method with volume-changing objects for ultrasound-triggered margination of microbubbles. *J. Fluid Mech.*, 836:952–997. 17, 69

[Guckenberger et al., 2018] Guckenberger, A., Kihm, A., John, T., Wagner, C., and Gekle, S. (2018). Numerical–experimental observation of shape bistability of red blood cells flowing in a microchannel. *Soft Matter*, 14(11):2032–2043. 52

[Guckenberger et al., 2016] Guckenberger, A., Schraml, M. P., Chen, P. G., Leonetti, M., and Gekle, S. (2016). On the bending algorithms for soft objects in flows. *Comput. Phys. Commun.*, 207:1–23. 17

[Hariprasad and Secomb, 2015] Hariprasad, D. S. and Secomb, T. W. (2015). Prediction of noninertial focusing of red blood cells in poiseuille flow. *Phys. Rev. E*, 92:033008. 52

[Imai et al., 2010] Imai, Y., Kondo, H., Ishikawa, T., Lim, C. T., and Yamaguchi, T. (2010). Modeling of hemodynamics arising from malaria infection. *J. biomech.*, 43(7):1386–1393. 11

[Kalluri and Bagchi, 2011] Kalluri, R. and Bagchi, P. (2011). Rheology of a dense capsule suspension. In *APS Meeting Abstracts*, volume 1, page 25010. 32

[Kantsler and Steinberg, 2005] Kantsler, V. and Steinberg, V. (2005). Orientation and dynamics of a vesicle in tank-treading motion in shear flow. *Phys. Rev. Lett.*, 95:258101. 32

[Kaoui et al., 2009a] Kaoui, B., Biros, G., and Misbah, C. (2009a). Why do red blood cells have asymmetric shapes even in a symmetric flow? *Phys. Rev. Lett.*, 103:188101. 52

[Kaoui et al., 2009b] Kaoui, B., Farutin, A., and Misbah, C. (2009b). Vesicles under simple shear flow: Elucidating the role of relevant control parameters. *Phys. Rev. E*, 80:061905. 46, 64

[Kaoui and Harting, 2016] Kaoui, B. and Harting, J. (2016). Two-dimensional lattice boltzmann simulations of vesicles with viscosity contrast. *Rheologica Acta*, 55(6):465–475. 3

[Kaoui et al., 2011] Kaoui, B., Harting, J., and Misbah, C. (2011). Two-dimensional vesicle dynamics under shear flow: Effect of confinement. *Phys. Rev. E*, 83(6):066319. 32

[Kaoui et al., 2014] Kaoui, B., Jonk, R. J., and Harting, J. (2014). Interplay between microdynamics and macrorheology in vesicle suspensions. *Soft Matter*, 10(26):4735–4742. 32, 73

[Kaoui et al., 2008] Kaoui, B., Ristow, G., Cantat, I., Misbah, C., and Zimmermann, W. (2008). Lateral migration of a two-dimensional vesicle in unbounded poiseuille flow. *Phys. Rev. E*, 77(2):021903. 16, 52, 73

[Keller and Skalak, 1982] Keller, S. R. and Skalak, R. (1982). Motion of a tank-treading ellipsoidal particle in a shear flow. *Journal of Fluid Mechanics*, 120:27–47. 2

[Kennedy et al., 1994] Kennedy, M., Pozrikidis, C., and Skalak, R. (1994). Motion and deformation of liquid drops, and the rheology of dilute emulsions in simple shear flow. *Comput. & Fluids*, 23(2):251–278. 36

[Kim et al., 2008] Kim, Y. H., VandeVord, P. J., and Lee, J. S. (2008). Multiphase non-newtonian effects on pulsatile hemodynamics in a coronary artery. *International journal for numerical methods in fluids*, 58(7):803–825. 7

[Kraus et al., 1996] Kraus, M., Wintz, W., Seifert, U., and Lipowsky, R. (1996). Fluid vesicles in shear flow. *Physical review letters*, 77(17):3685. 3

[Krieger and Dougherty, 1959] Krieger, I. M. and Dougherty, T. J. (1959). A mechanism for non-newtonian flow in suspensions of rigid spheres. *Trans. Soc. Rheol.*, 3(1):137–152. 8

[Krüger et al., 2013] Krüger, T., Gross, M., Raabe, D., and Varnik, F. (2013). Crossover from tumbling to tank-treading-like motion in dense simulated suspensions of red blood cells. *Soft Matter*, 9(37):9008–9015. 3

[Lamb, 1993] Lamb, H. (1993). *Hydrodynamics*. Cambridge university press. 23

[Lamura and Gompper, 2013] Lamura, A. and Gompper, G. (2013). Dynamics and rheology of vesicle suspensions in wall-bounded shear flow. *Europhys. Lett.*, 102(2):28004. 32, 73

[Lamura and Gompper, 2015] Lamura, A. and Gompper, G. (2015). Rheological properties of sheared vesicle and cell suspensions. *Proc. IUTAM*, 16:3 – 11. 32

[Lanotte et al., 2016] Lanotte, L., Mauer, J., Mendez, S., Fedosov, D. A., Fromental, J.-M., Claveria, V., Nicoud, F., Gompper, G., and Abkarian, M. (2016). Red cells' dynamic morphologies govern blood shear thinning under microcirculatory flow conditions. *Proceedings of the National Academy of Sciences*, 113(47):13289–13294. 3, 4, 11, 35

[Larson, 1999] Larson, R. G. (1999). *The structure and rheology of complex fluids*, volume 33. Oxford university press New York. 31, 51

[Lebedev et al., 2007] Lebedev, V. V., Turitsyn, K. S., and Vergeles, S. S. (2007). Dynamics of nearly spherical vesicles in an external flow. *Phys. Rev. Lett.*, 99:218101. 3, 64

[Lee et al., 2011] Lee, B.-K., Xue, S., Nam, J., Lim, H., and Shin, S. (2011). Determination of the blood viscosity and yield stress with a pressure-scanning capillary hemorheometer using constitutive models. *Korea-Australia Rheology Journal*, 23(1):1. 7

[Li et al., 2013] Li, X., Vlahovska, P. M., and Karniadakis, G. E. (2013). Continuum- and particle-based modeling of shapes and dynamics of red blood cells in health and disease. *Soft Matter*, 9(1):28–37. 11

[Lipowsky, 2005] Lipowsky, H. H. (2005). Microvascular rheology and hemodynamics. *Microcirculation*, 12(1):5–15. 5

[Lipowsky and Sackmann, 1995] Lipowsky, R. and Sackmann, E. (1995). *Structure and dynamics of membranes: I. from cells to vesicles/II. generic and specific interactions*, volume 1. Elsevier. 15

[Maeda and Shiga, 1985] Maeda, N. and Shiga, T. (1985). Inhibition and acceleration of erythrocyte aggregation induced by small macromolecules. *Biochimica et Biophysica Acta (BBA)-General Subjects*, 843(1-2):128–136. 7

[Mansard and Colin, 2012] Mansard, V. and Colin, A. (2012). Local and non local rheology of concentrated particles. *Soft Matter*, 8(15):4025–4043. 85

[Marcinkowska-Gapińska et al., 2007] Marcinkowska-Gapińska, A., Gapinski, J., Elikowski, W., Jaroszyk, F., and Kubisz, L. (2007). Comparison of three rheological models of shear flow behavior studied on blood samples from post-infarction patients. *Medical & biological engineering & computing*, 45(9):837–844. 7

[Matsunaga et al., 2014] Matsunaga, D., Imai, Y., Omori, T., Ishikawa, T., and Yamaguchi, T. (2014). A full gpu implementation of a numerical method for simulating capsule suspensions. *J. Biomech. Sci. Eng.*, 9(3):14–00039–14–00039. 32

[Matsunaga et al., 2016] Matsunaga, D., Imai, Y., Yamaguchi, T., and Ishikawa, T. (2016). Rheology of a dense suspension of spherical capsules under simple shear flow. *J. Fluid Mech.*, 786:110–127. 32

[Mauer et al., 2018] Mauer, J., Mendez, S., Lanotte, L., Nicoud, F., Abkarian, M., Gompper, G., and Fedosov, D. A. (2018). Flow-induced transitions of red blood cell shapes under shear. *Physical review letters*, 121(11):118103. 3

[Merrill et al., 1963] Merrill, E., Gilliland, E., Cokelet, G., Shin, H., Britten, A., and Wells, R. (1963). Rheology of human blood, near and at zero flow. *Biophysical Journal*, 3(3):199–213. 5

[Merrill et al., 1969] Merrill, E. W., Cheng, C. S., and Pelletier, G. A. (1969). Yield stress of normal human blood as a function of endogenous fibrinogen. *Journal of Applied Physiology*, 26(1):1–3. 5

[Misbah, 2006] Misbah, C. (2006). Vacillating breathing and tumbling of vesicles under shear flow. *Phys. Rev. Lett.*, 96:028104. 2, 32, 40

[Misbah, 2017] Misbah, C. (2017). *Complex Dynamics and Morphogenesis*. Springer. 62

[Misra and Maiti, 2012] Misra, J. and Maiti, S. (2012). Peristaltic pumping of blood through small vessels of varying cross-section. *Journal of Applied Mechanics*, 79(6):061003. 7

[Molla and Paul, 2012] Molla, M. M. and Paul, M. (2012). Les of non-newtonian physiological blood flow in a model of arterial stenosis. *Medical engineering & physics*, 34(8):1079–1087. 7

[Morris et al., 1987] Morris, C. L., Smith, C. M., and Blackshear, P. (1987). A new method for measuring the yield stress in thin layers of sedimenting blood. *Biophysical journal*, 52(2):229–240. 5, 7

[Nait-Ouhra et al., 2018] Nait-Ouhra, A., Guckenberger, A., Farutin, A., Ez-Zahraouy, H., Benyoussef, A., Gekle, S., and Misbah, C. (2018). Lateral vesicle migration in a bounded shear flow: Viscosity contrast leads to off-centered solutions. *Phys. Rev. Fluids*, 3:123601. 73, 74, 75

[Narsimhan et al., 2013] Narsimhan, V., Zhao, H., and Shaqfeh, E. S. (2013). Coarse-grained theory to predict the concentration distribution of red blood cells in wall-bounded couette flow at zero reynolds number. *Physics of Fluids*, 25(6):061901. 85, 89

[Olla, 1997a] Olla, P. (1997a). The lift on a tank-treading ellipsoidal cell in a shear flow. *J. Phys. II France*, 7(10):1533–1540. 52, 73

[Olla, 1997b] Olla, P. (1997b). The role of tank-treading motions in the transverse migration of a spheroidal vesicle in a shear flow. *J. Phys. A: Math. Gene.*, 30(1):317. 52, 57, 73

[Olla, 1999] Olla, P. (1999). Simplified model for red cell dynamics in small blood vessels. *Phys. Rev. Lett.*, 82(2):453. 52, 73

[Olla, 2000] Olla, P. (2000). The behavior of closed inextensible membranes in linear and quadratic shear flows. *Physica A*, 278(1):87–106. 52, 73

[Pauling et al., 1949] Pauling, L., Itano, H. A., Singer, S. J., and Wells, I. C. (1949). Sickle cell anemia, a molecular disease. *Science*, 110(2865):543–548. 10

[Peyla and Verdier, 2011] Peyla, P. and Verdier, C. (2011). New confinement effects on the viscosity of suspensions. *EPL*, 94(4):44001. 9

[Picart et al., 1998] Picart, C., Piau, J.-M., Galliard, H., and Carpentier, P. (1998). Human blood shear yield stress and its hematocrit dependence. *Journal of Rheology*, 42(1):1–12. 5

[Pontrelli, 1998] Pontrelli, G. (1998). Pulsatile blood flow in a pipe. *Computers & fluids*, 27(3):367–380. 7

[Pontrelli, 2000] Pontrelli, G. (2000). Blood flow through a circular pipe with an impulsive pressure gradient. *Mathematical Models and Methods in Applied Sciences*, 10(02):187–202. 7

[Popel and Johnson, 2005] Popel, A. S. and Johnson, P. C. (2005). Microcirculation and hemorheology. *Annu. Rev. Fluid Mech.*, 37:43–69. 85

[Pozrikidis, 1992] Pozrikidis, C. (1992). *Boundary Integral and Singularity Methods for Linearized Viscous Flow*. Cambridge University Press, Cambridge, UK. 20, 25, 26

[Pries et al., 1992] Pries, A., Neuhaus, D., and Gaehtgens, P. (1992). Blood viscosity in tube flow: dependence on diameter and hematocrit. *Am. J. Physiol. Heart Circ. Physiol.*, 263(6):H1770–H1778. 6, 52, 85

[Pries et al., 1996] Pries, A., Secomb, T. W., and Gaehtgens, P. (1996). Biophysical aspects of blood flow in the microvasculature. *Cardiovascular research*, 32(4):654–667. 85

[Qi and Shaqfeh, 2017] Qi, Q. M. and Shaqfeh, E. S. G. (2017). Theory to predict particle migration and margination in the pressure-driven channel flow of blood. *Phys. Rev. Fluids*, 2:093102. 52, 85, 89

[Qi and Shaqfeh, 2018] Qi, Q. M. and Shaqfeh, E. S. G. (2018). Time-dependent particle migration and margination in the pressure-driven channel flow of blood. *Phys. Rev. Fluids*, 3:034302. 52

[Rahimian et al., 2010] Rahimian, A., Veerapaneni, S. K., and Biros, G. (2010). Dynamic simulation of locally inextensible vesicles suspended in an arbitrary two-dimensional domain, a boundary integral method. *J. Comp. Physics*, 229(18):6466–6484. 54, 74

[Reasor et al., 2013] Reasor, D., Clausen, J., and Aidun, C. (2013). Rheological characterization of cellular blood in shear. *J. Fluid Mech.*, 726:497–516. 32

[Robertson et al., 2008] Robertson, A. M., Sequeira, A., and Kameneva, M. (2008). Hemorheology. hemodynamical flows. modeling, analysis and simulation, oberwolfach seminars, vol. 37, 63-120. 11

[Robertson et al., 2009] Robertson, A. M., Sequeira, A., and Owens, R. G. (2009). Rheological models for blood. In *Cardiovascular mathematics*, pages 211–241. Springer. 7

[Saadat et al., 2019] Saadat, A., Guido, C. J., and Shaqfeh, E. S. (2019). Simulation of red blood cell migration in small arterioles: Effect of cytoplasmic viscosity. *bioRxiv*, page 572933. 85

[Samsel and Perelson, 1982] Samsel, R. W. and Perelson, A. S. (1982). Kinetics of rouleau formation. i. a mass action approach with geometric features. *Biophysical Journal*, 37(2):493–514. 5

[Sangani et al., 2011] Sangani, A. S., Acrivos, A., and Peyla, P. (2011). Roles of particle-wall and particle-particle interactions in highly confined suspensions of spherical particles being sheared at low reynolds numbers. *Phys. Fluids*, 23(8):083302. 9

[Sbragaglia et al., 2012] Sbragaglia, M., Benzi, R., Bernaschi, M., and Succi, S. (2012). The emergence of supramolecular forces from lattice kinetic models of non-ideal fluids: applications to the rheology of soft glassy materials. *Soft Matter*, 8(41):10773–10782. 85

[Schmid-Schonbein, 1975] Schmid-Schonbein, H. (1975). Erythrocyte rheology and the optimization of mass transport in the microcirculation. *Blood Cells*, 1(1):285. 2

[Schmid-Schönbein and Wells, 1969] Schmid-Schönbein, H. and Wells, R. (1969). Fluid drop-like transition of erythrocytes under shear. *Science*, 165(3890):288–291. 2

[Schmid-Schönbein and Wells, 1971] Schmid-Schönbein, H. and Wells, R. (1971). Rheological properties of human erythrocytes and their influence upon the "anomalous" viscosity of blood. In *Ergebnisse der Physiologie Reviews of Physiology, Volume 63*, pages 146–219. Springer. 5, 10

[Schmid-schönbein et al., 1969] Schmid-schönbein, H., Wells, R., and Goldstone, J. (1969). Influence of deformability of human red cells upon blood viscosity. *Circ. Res.*, 25(2):131–143. 5

[Secomb, 2017] Secomb, T. W. (2017). Blood flow in the microcirculation. *Annu. Rev. Fluid Mech.*, 49(1):443–461. 3

[Seifert, 1999] Seifert, U. (1999). Hydrodynamic lift on bound vesicles. *Phys. Rev. Lett.*, 83(4):876. 52, 73

[Shen et al., 2016] Shen, Z., Coupier, G., Kaoui, B., Polack, B., Harting, J., Misbah, C., and Podgorski, T. (2016). Inversion of hematocrit partition at microfluidic bifurcations. *Microvascular research*, 105:40–46. 85

[Shen et al., 2017] Shen, Z., Farutin, A., Thiébaud, M., and Misbah, C. (2017). Interaction and rheology of vesicle suspensions in confined shear flow. *Phys. Rev. Fluids*, 2(10):103101. 35, 44, 52

[Shen et al., 2018] Shen, Z., Fischer, T. M., Farutin, A., Vlahovska, P. M., Harting, J., and Misbah, C. (2018). Blood crystal: emergent order of red blood cells under wall-confined shear flow. *Phys. Rev. Lett.*, 120(26):268102. 9, 32, 81

[Sukumaran and Seifert, 2001] Sukumaran, S. and Seifert, U. (2001). Influence of shear flow on vesicles near a wall: a numerical study. *Phys. Rev. E*, 64(1):011916. 52, 57, 73

[Suresh, 2006] Suresh, S. (2006). Mechanical response of human red blood cells in health and disease: some structure-property-function relationships. *J. Mater. Res.*, 21(8):1871–1877. 11

[Taylor, 1932] Taylor, G. I. (1932). The viscosity of a fluid containing small drops of another fluid. *Proceedings of the Royal Society of London. Series A, Containing Papers of a Mathematical and Physical Character*, 138(834):41–48. 8

[Thiébaud and Misbah, 2013] Thiébaud, M. and Misbah, C. (2013). Rheology of a vesicle suspension with finite concentration: A numerical study. *Phys. Rev. E*, 88:062707. 32, 33, 39, 40, 54, 73, 74

[Thiébaud et al., 2014] Thiébaud, M., Shen, Z., Harting, J., and Misbah, C. (2014). Prediction of anomalous blood viscosity in confined shear flow. *Phys. Rev. Lett.*, 112(23):238304. 9, 10, 32, 33, 35, 36, 44, 47, 50, 73, 79, 80, 82

[Thurston, 1972] Thurston, G. B. (1972). Viscoelasticity of human blood. *Biophysical journal*, 12(9):1205–1217. 5

[Tomaiuolo, 2014] Tomaiuolo, G. (2014). Biomechanical properties of red blood cells in health and disease towards microfluidics. *Biomicrofluidics*, 8(5):051501. 1

[Trozzo et al., 2015] Trozzo, R., Boedec, G., Leonetti, M., and Jaeger, M. (2015). Axisymmetric boundary element method for vesicles in a capillary. *Journal of Computational Physics*, 289:62–82. 3, 16

[Viallat and Abkarian, 2014] Viallat, A. and Abkarian, M. (2014). Red blood cell: from its mechanics to its motion in shear flow. *International journal of laboratory hematology*, 36(3):237–243. 3

[Vitkova et al., 2012] Vitkova, V., Farutin, A., Polack, B., Misbah, C., and Podgorski, T. (2012). Erythrocyte dynamics in flow affects blood rheology. In *Journal of Physics: Conference Series*, volume 398, page 012027. IOP Publishing. 3

[Vitkova et al., 2008] Vitkova, V., Mader, M.-A., Polack, B., Misbah, C., and Podgorski, T. (2008). Micro-macro link in rheology of erythrocyte and vesicle suspensions. *Biophys. J.*, 95:33–35. 1, 32, 54, 74

[Vlahovska and Gracia, 2007] Vlahovska, P. M. and Gracia, R. S. (2007). Dynamics of a viscous vesicle in linear flows. *Phys. Rev. E*, 75(1):016313. 32

[Wang and Popel, 1993] Wang, C.-H. and Popel, A. S. (1993). Effect of red blood cell shape on oxygen transport in capillaries. *Mathematical biosciences*, 116(1):89–110. 11

[Xu and Kleinstreuer, 2019] Xu, Z. and Kleinstreuer, C. (2019). Heterogeneous blood flow in microvessels with applications to nanodrug transport and mass transfer into tumor tissue. *Biomechanics and modeling in mechanobiology*, 18(1):99–110. 89

[Zhao and Shaqfeh, 2011] Zhao, H. and Shaqfeh, E. S. (2011). The dynamics of a vesicle in simple shear flow. *Journal of Fluid Mechanics*, 674:578–604. 3

[Zhao and Shaqfeh, 2013] Zhao, H. and Shaqfeh, E. S. (2013). The dynamics of a non-dilute vesicle suspension in a simple shear flow. *J. Fluid Mech.*, 725:709–731. 54, 74

[Zhong-Can and Helfrich, 1989] Zhong-Can, O.-Y. and Helfrich, W. (1989). Bending energy of vesicle membranes: General expressions for the first, second, and third variation of the shape energy and applications to spheres and cylinders. *Phys. Rev. A*, 39(10):5280. 15, 16